The University of Nottingham
UNITED KINGDOM · CHINA · MALAYSIA

Tan, Chye Cheah (2016) Medical image registration and soft tissue deformation for image guided surgery system. PhD thesis, University of Nottingham.

Access from the University of Nottingham repository:
http://eprints.nottingham.ac.uk/33904/1/Thesis.pdf

Copyright and reuse:

The Nottingham ePrints service makes this work by researchers of the University of Nottingham available open access under the following conditions.

This article is made available under the University of Nottingham End User licence and may be reused according to the conditions of the licence. For more details see: http://eprints.nottingham.ac.uk/end_user_agreement.pdf

For more information, please contact eprints@nottingham.ac.uk

Medical Image Registration and Soft Tissue Deformation for Image Guided Surgery System

TAN CHYE CHEAH

Thesis submitted to the University of Nottingham
for the degree of Doctor of Philosophy

February 2016

Acknowledgements

This thesis would not have been possible without the help of my supervisor and my research collaborator, CBMTI Pte Ltd at University Malaya. First and foremost, I thank my supervisor S.Anandan Shanmugam for his help and support over the past five years. I would like to sincerely thank him for accepting me into the doctoral program and providing me with the necessary resources to succeed. His great efforts to explain things clearly and simply have been a source of inspiration for me.

This thesis is a result of discussions and collaborations with many people. In particular I wish to acknowledge Prof. Vicknes Waran, Alwin Kumar Rathinam, Dr. Kenneth Ang Li Mann (formerly University of Nottingham), Dr. Jasmine Kah-Phooi Seng (formerly University of Nottingham), and Dr. Lim Wee Gin. I also thank graduate and undergraduate students who have directly helped me with my research. These include Ho YuXin, Sunaina Manadath Pillay, Patrick Kunle Adebayo, Vasanth Vyasamurthy Arunkumar, and Lim Wei – Wu Ivan.

I thank my parents for instilling the importance of a good education very early in life. I am grateful to my parents, my sister, and my in-laws for their constant encouragement and love. Last but not least, I gratefully thank my wife, Kay Yong who has supported me through it all with over the past five years. The decision to start my PhD study at the University of Nottingham was made by both Kay Yong and myself. I do not think I can adequately articulate my gratitude for her love, help, and support which made this thesis possible.

Abstract

In parallel with the developments in imaging modalities, image-guided surgery (IGS) can now provide the surgeon with high quality three-dimensional images depicting human anatomy. Although IGS is now in widely use in neurosurgery, there remain some limitations that must be overcome before it can be employed in more general minimally invasive procedures. In this thesis, we have developed several contributions to the field of medical image registration and brain tissue deformation modeling. From the methodology point of view, medical image registration algorithms can be classified into feature-based and intensity-based methods. One of the challenges faced by feature-based registration would be to determine which specific type of feature is desired for a given task and imaging type. For this reason, a point set registration using points and curves feature is proposed, which has the accuracy of registration based on points and the robustness of registration based on lines or curves.

We have also tackled the problem on rigid registration of multimodal images using intensity-based similarity measures. Mutual information (MI) has emerged in recent years as a popular similarity metric and widely being recognized in the field of medical image registration. Unfortunately, it ignores the spatial information contained in the images such as edges and corners that might be useful in the image registration. We introduce a new similarity metric, called Adaptive Mutual Information (AMI) measure which incorporates the gradient spatial information. Salient pixels in the regions with high gradient value will contribute more in the estimation of mutual information of image pairs being registered. Experimental results showed that our proposed method improves

registration accuracy and it is more robust to noise images which have large deviation from the reference image. Along with this direction, we further improve the technique to simultaneously use all information obtained from multiple features. Using multiple spatial features, the proposed algorithm is less sensitive to the effect of noise and some inherent variations, giving more accurate registration.

Brain shift is a complex phenomenon and there are many different reasons causing brain deformation. We have investigated the pattern of brain deformation with respect to location and magnitude and to consider the implications of this pattern for correcting brain deformation in IGS systems. A computational finite element analysis was carried out to analyze the deformation and stress tensor experienced by the brain tissue during surgical operations. Finally, we have developed a prototype visualization display and navigation platform for interpretation of IGS. The system is based upon Qt (cross-platform GUI toolkit) and it integrates VTK (an object-oriented visualization library) as the rendering kernel. Based on the construction of a visualization software platform, we have laid a foundation on the future research to be extended to implement brain tissue deformation into the system.

Publications

1. Tan Chye Cheah, S.Anandan Shanmugam, and Ang Li Minn: ‘Medical image registration: Comparison and evaluation of nonlinear transformation algorithms’. Proc. Biomedical Engineering and Sciences (IECBES), 2010 IEEE EMBS Conference on, Kuala Lumpur, Nov. 30 2010-Dec. 2 2010.
2. Tan Chye Cheah, S.Anandan Shanmugam, and Ang Li Minn: ‘Medical Image Registration by Maximizing Mutual Information Based on Combination of Intensity and Gradient Information’. International Conference on Biomedical Engineering (ICoBE), 2012 IEEE ICoBE Conference on, Penang, Feb. 27 2012-Feb. 28 2012.
3. Tan Chye Cheah, S.Anandan Shanmugam, Alwin Kumar Rathinam, and Vicknes Waran: ‘Modeling the interaction between navigation probe and deformable brain tissue based on finite element analysis: preliminary study’. Biomedical Engineering and Sciences (IECBES), 2012 IEEE EMBS Conference on, Langkawi, Dec. 17 2012-Dec. 19 2012.
4. Tan Chye Cheah, S.Anandan Shanmugam, and Ang Li Minn. (2012). "Adaptation of Mutual Information Measure by Using Image Gradient Information." Journal of Medical Imaging and Health Informatics 2(3): 313-319.
5. Tan Chye Cheah and S.Anandan Shanmugam (2015). "Multi-Features for Mutual Information based Medical Image Registration." Journal of Medical Imaging and Health Informatics 5(5): 1076-1083.

Table of Contents

List of Figures

List of Tables

List of Abbreviations

CT	Computed tomography
DICOM	Digital imaging and communications
fMRI	Functional magnetic resonance imaging
FOV	Field of view
GPU	Graphic processing unit
ICP	Iterative closet point
IGI	Image-guided intervention
IGS	Image-guided surgery
iMRI	Intraoperative magnetic resonance imaging
LED	Light emitting diodes
MI	Mutual information
MRI	Magnetic resonance imaging
NCC	Normalized cross correlation
NMI	Normalized mutual information
OR	Operating room
PET	Positron emission tomography
RMS	Root mean square
SAD	Sum of absolute differences
SPECT	Single photon emission computed tomography
SSD	Sum of squared differences
US	Ultrasound

Chapter 1

Introduction

1.1 Motivation

In the last decades, image-guided surgery (IGS) has acquired great importance due to the rapidly evolving technology of the medical imaging. Conventionally, surgeons have to rely on their knowledge of human anatomy to relate two-dimensional images of magnetic resonance (MR) or computed tomography (CT) to the patient in the operating room. However this can be challenging because all patients' anatomies aren't uniform or identical. Thus the use of IGS navigation system has become a standard way to assist the surgeon in planning and guiding the surgery especially in minimally invasive surgery where the incision is small. Although advancements have been made for different components of IGS system such as localizers, registration techniques, and visualization, no one can confirm that the perfect model has been found for any of them. Recent trend is showing increased interest on the subject shown by the number of publications with the keywords "image guided surgery" on the PubMed database [2]. Despite the vast amount of literature published on the subject every year, there are research problems yet to be solved. This thesis is focused on addressing a small part of that problem. Among the different research topics related to medical image processing, this research is focused in two of them, medical image registration and image deformation modeling using CT and MR brain images as the primary source of images.

1.2 Problem Statement

In the field of medical image registration, a significant breakthrough is taking place with the development of image similarity measures and registration algorithms based on entropy and specifically, mutual information (MI) measures which were derived from the information theory. The MI similarity metric, proposed by Collignon et al. [3] and by Viola et al. [4], is proven to be one of the most accurate automatic multimodal registration methods in Retrospective Registration Evaluation Project (RREP) [5]. Although it has been widely accepted in the field of medical image registration, there are situations which can challenge the applicability of MI and result in misregistration [6, 7]. Several causes for misregistration include (1) changes in patient's anatomy between scans which cause large deviation from the reference image; (2) poor image quality or the images are in low resolution; (3) incorrect registration outcomes as a result of local maxima and interpolation methods; and (4) weak statistical dependence between different imaging modalities, such as MR and ultrasound. As such there is a need to devise methods that are more robust to handle a wide variety of registration difficulties.

Furthermore, the focus of this research in medical image analysis of IGS system is extended to understand and model the deformations that occur both pre-operatively and intra-operatively. In order to provide accurate spatial navigation and guidance, IGS relies on the accuracy of coregistration of the patient's position in operating room, patient-specific images generated by CT or MR, and surgical instrument location (see Figure 1.1). This accuracy is dependent on the assumption of accurate initial registration and a static relationship between patient and image model. However, brain tissue deformation and shifting occurs during surgery can compromise this spatial relationship. It is due to

various reasons including tissue retraction/ resection, gravity, hyperosmotic drugs, and pathology [8-10]. To date, it has been reported that the range of surface shift could differ from 1 to 2.5cm [11], while subsurface movement was 6 to 7mm from their preoperative image during surgery [10, 12]. Since the brain undergoes varying levels of deformations at different stages of the surgery, the navigation system based on preoperative images cannot accurately describe such movements which subsequently could lead to surgical error. In order to address this problem, attempts to characterize the deformation led to the development of intraoperative imaging. Although intraoperative CT/MR scanners offer powerful solution to brain deformation, they have been questioned to justify various limitations and their cost-effectiveness. In fact, we are looking at the possibility of building a deformation visualization technique using finite element (FE) methods to simulate the intraoperative brain shift. If the soft tissue deformation could be detected, and update the pre-operative images, then this technology could have a major impact on many more common procedures. This medical image visualization technique is a research effort to provide better navigation during the actual surgical procedure.

1.3 Objective

IGS is a surgical technique for localizing anatomical structures on the basis of preoperative image data and determining the optimal surgical path to reach these structures. Figure 1.2 shows the block diagram of the research project implementation, which consists of a data processing interface module (blue area) and the tracking devices (orange area). The blue area is the scope of this thesis which will be discussed in the following chapters. The overall purpose of this thesis is to develop a new registration

technique and investigate brain deformation modeling based on FE analysis within the field of IGS. The underlying hypotheses are: (1) incorporating the spatial information available within images will significantly improve the performance of the MI based image registration and (2) advanced visualization technique can improve the performance of the surgeon. The scopes of this research project are listed as the following:

1. Develop new information-theoretic algorithms to improve the image registration process in terms of accuracy and robustness.
2. Investigate brain tissue deformation phenomena induced by probe insertion based on FE analysis.
3. Develop a prototype of visualization and navigation system.

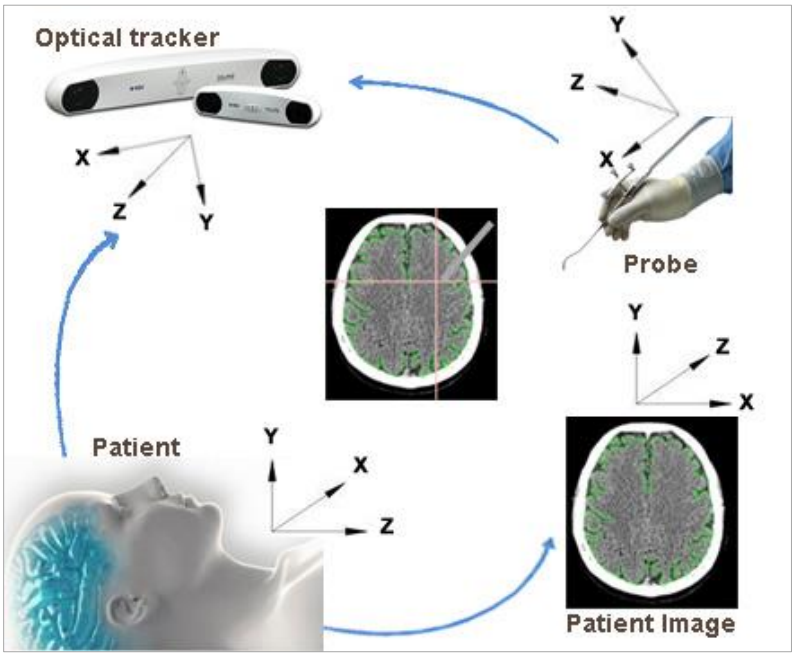

Figure 1.1: Typical instrument tracking scenario. A number of coordinate transformation calculations must be made to relate between different coordinate systems.

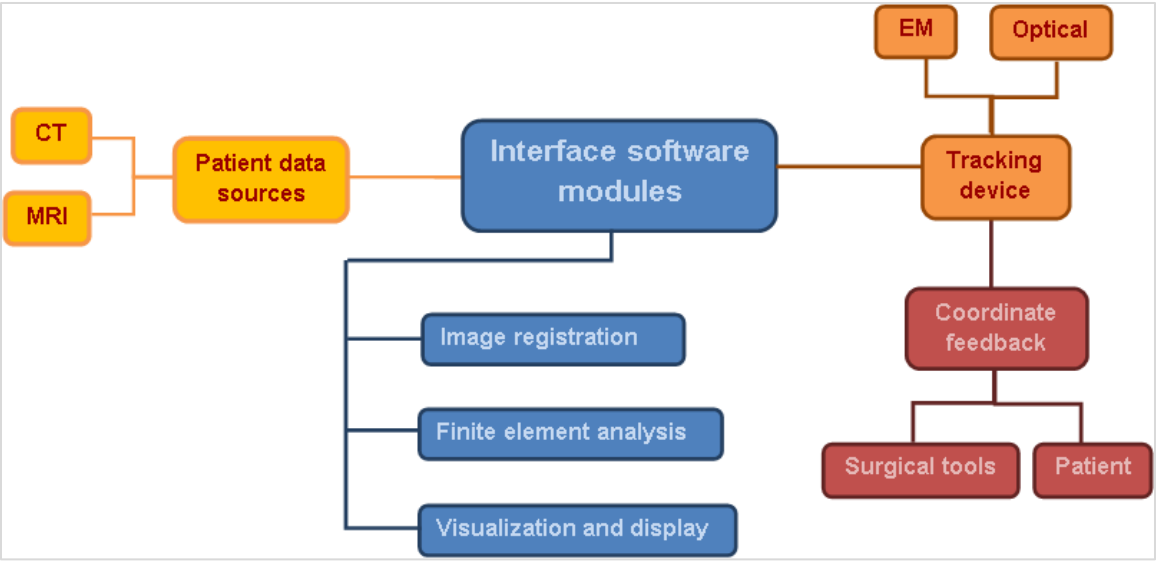

Figure 1.2: Block diagram of image-guided surgery system architecture.

1.4 Research methodology

In this section, we outline the research methodology that was followed to fulfill the objective above.

1. The requirements and system architecture of IGS were first investigated to better understand the environment in which the newly proposed methods were expected to operate.
2. Secondly, we surveyed and reviewed the existing image registration algorithm designed specifically for medical context. This ranges from feature based registration to intensity based algorithm.
3. Thirdly, feature-based registration will be investigated with nonlinear image deformation. For this reason, a point set registration method using points and curves feature is proposed.

4. Fourthly, we made some adaptations to the most efficient registration algorithm among the surveyed – MI algorithm by using gradient information. The performance of the adaption technique was analyzed and compared to the existing MI algorithm.
5. Fifthly, we made several improvements to overcome the weaknesses of the existing MI algorithm and introduced Multi-Features Mutual Information (MF-MI) to incorporate multiple image features.
6. Sixthly, we studied the brain deformation phenomena induced by probe insertion based on FE analysis to provide useful information concerning brain tissues deformation when under external stress.
7. Next, we build a prototype of visualization and navigation system for interpretation of IGS based on ITK and VTK libraries.

1.5 Thesis outline

This thesis is organized into seven (7) chapters. The first two chapters are introduction and literature review of the existing methods related to our research area. Chapter 3 describes the development of point set registration method using points and curves feature. The next two chapters, chapter 4 and 5 are focused on the improvement of MI registration technique. Chapter 6 explains the implementation of prototype IGS visualization system and presents modeling of soft tissue deformation based on finite element analysis. Lastly, chapter 7 draws conclusions about the research discussed herein. The following provides a brief description of every chapter:

- Chapter 2: **Literature Review**

  In this chapter, a review of the research topics is outlined. First, we introduce the workflow of IGS and explain the components related to IGS system, namely registration, tracking, and visualization. Second, a brief overview of medical image registration on the registration framework was covered. Finally, we discussed the existing research work to enhance MI technique and a state of the art of the soft tissue modeling techniques.

- Chapter 3 – **Improved Nonlinear Point Set Registration by Uniform Curve Features Subdivision Technique**

  For this chapter, feature-based registration will be investigated with nonlinear image deformation. A point set registration method using points and curves feature was proposed, which has the accuracy of registration based on points and the robustness of registration based on lines or curves. We consider the alignment of two features as point sets alignment. The extracted line or curve pairs are modeled by point sampling so that they are subdivided according to curvature and length of curves. The mechanism of uniform subdivision of curves segment ensures that the subdivided points can match the original curve as close as possible and fulfill the requirement of point set registration. We have tested the algorithm on real medical images and apply TPS transformation to describe nonlinear deformation. The experimental result reveals that the image registration algorithm with combination of point and curve feature is a feasible approach. The following publication was a result of work conducted based on this chapter:

1. Tan Chye Cheah, S.Anandan Shanmugam, and Ang Li Minn: 'Medical image registration: Comparison and evaluation of nonlinear transformation algorithms'. Proc. Biomedical Engineering and Sciences (IECBES), 2010 IEEE EMBS Conference on, Kuala Lumpur, Nov. 30 2010-Dec. 2 2010.

- Chapter 4 – **Adaptation of Mutual Information Measure by Using Image Gradient Information**

  In this chapter, we have presented the adaptation of mutual information measure which incorporates the spatial information based on significance of pixels. We assumed that the image locations with a strong gradient contain high information value, which could be useful for the image registration. The proposed method uses a simple way to enrich the image description by integrating the gradient information. Experimental results showed that the proposed method improves registration accuracy and it is more robust to noise images which have large deviation from the reference image. The following publications were a result of work conducted based on this chapter:

  1. Tan Chye Cheah, S.Anandan Shanmugam, and Ang Li Minn: 'Medical Image Registration by Maximizing Mutual Information Based on Combination of Intensity and Gradient Information'. International Conference on Biomedical Engineering (ICoBE), 2012 IEEE ICoBE Conference on, Penang, Feb. 27 2012-Feb. 28 2012.

2. Tan Chye Cheah, S.Anandan Shanmugam, and Ang Li Minn. (2012). "Adaptation of Mutual Information Measure by Using Image Gradient Information." Journal of Medical Imaging and Health Informatics 2(3): 313-319.

- Chapter 5 – **Multi-Features for Mutual Information based Medical Image Registration**

  The method presented in this chapter is an extension of previous work aimed towards registration of multiple spatial features. We proposed multi-features mutual information (MF-MI) measure to simultaneously use all information obtained from multiple features. One major contribution of MF-MI is the incorporation of multiple image features into MI algorithm, while allowing a flexible choice of the spatial information through weighting coefficients. The method is thoroughly investigated and its accuracy and robustness are evaluated on both simulated and experimental data. Through quantitative evaluations, the MF-MI measure is proven to handle a wide variety of registration difficulties. Using multiple spatial features, the proposed algorithm is less sensitive to the effect of noise and some inherent variations, giving more accurate registration. The following publication was a result of work conducted based on this chapter:

  1. Tan Chye Cheah and S.Anandan Shanmugam (2015). "Multi-Features for Mutual Information based Medical Image Registration." Journal of Medical Imaging and Health Informatics 5(5): 1076-1083.

- Chapter 6 – **Image-guided surgery system: Development of data visualization interface with navigation probe-tissue interaction**

  In this chapter, a prototype visualization display and navigation platform was built for interpretation of IGS. The main framework is based upon Qt (cross-platform GUI toolkit) and it integrates VTK (an object-oriented visualization library) as the rendering kernel. This system has finished several main functions, like DICOM data displaying in multi-planar reformation and image-patient registration. This chapter also presents a simple physical modeling to analyze the deformation and stress tensor experienced by the brain tissue during surgical operations. FE software COMSOL Multiphysics was used for discretizing and solving partial differential equations that describe the brain tissue deformation. Simulation results have displayed that the brain shape deformations and brain tissue deformation experience around the probe tip. Based on the construction of a visualization software platform, we have laid a foundation on the future research to be extended to implement brain tissue deformation to the data processing module. By modeling, it gives us some simulation data on actual implementation of the system. The following publication was a result of work conducted based on this chapter:

  1. Tan Chye Cheah, S.Anandan Shanmugam, Alwin Kumar Rathinam, and Vicknes Waran: 'Modeling the interaction between navigation probe and deformable brain tissue based on finite element analysis: preliminary study'. Biomedical Engineering and Sciences (IECBES), 2012 IEEE EMBS Conference on, Langkawi, Dec. 17 2012-Dec. 19 2012.

- Chapter 8 – **Conclusion and Future Work**

  This chapter provides a summary of the main results and contributions of the thesis, followed by a description of the future applications and research directions that can be used to build on this work.

Chapter 2

Image-guided surgery (IGS)

2.1 Introduction

IGS is a surgical technique to provide navigation and guidance by establishing the spatial correspondence on the basis of images obtained preoperatively. It requires accurate spatial correlation between the image space (coordinate system within the acquired image series) and physical space (coordinate system relevant to patient's anatomy). The process is often referred to as registration. To fulfill this task accurately, the identification of landmark points or fiducials fixed to the patient and their corresponding location in the pre-operative images are required. These points are then used to derive the coordinate transformation matrix that map the position of image space and physical space. Generally, a least-squares approach is used to obtain the correct registration between corresponding points. Once registration has been established, any position of a pointer in the patient's body is displayed accordingly in the image data. Usually, the pointer tip is projected as crosshairs in the corresponding three orthogonal views (axial, coronal and sagittal slices of the image series) as shown in Figure 2.1. With the tracking information provided, the position of the tip is shown on the screen simultaneously and is updated continuously as the surgeon maneuvers through the anatomy of the patient. Based on the accurate visual feedback, IGS system enhances the information integration of the surgeon and makes it possible to carry out surgical procedures that are more precise and less invasive than conventional procedures. In general, IGS procedure comprises three phases.

- *Preoperative phase*

  Before an operation, patient's data is collected through different imaging modalities such as X-rays, CT, MR, ultrasound and nuclear imaging. The image data provides important information about the structural and the functional meaning of objects of interest in the image space. The objects of interest can be tumors, major vessels, or physiologically important brain structures. Based on the information, surgeon can plan the surgical path and determine exactly the size, shape, location and orientation of the craniotomy to be performed.

- *Intraoperative phase*

  Before the surgery starts, the preoperative images and surgical plan are transferred to the computer in the operating room. The patient's head will be fixed to the operating table to avoid shifting. Patient registration is required to register patient or physical space to image space before the preoperative images can be used interactively. It is a process of determining feature points based on the fiducial markers or anatomical landmarks from CT or MRI image data and relating them to the corresponding patient data. The paired points need to be matched accurately to provide a rigid-body transformation matrix which describes their relationship. Coordinate matching ensures that any point seen in the image data corresponds to an actual point in the patient's anatomy. Once registration has been established, the surgeon can then safely navigate and execute their surgical plan accordingly.

- *Postoperative phase*

  The preoperative and intraoperative information are combined with additional images to verify the technical results of the procedure and to assess the longer-term clinical results for the patient.

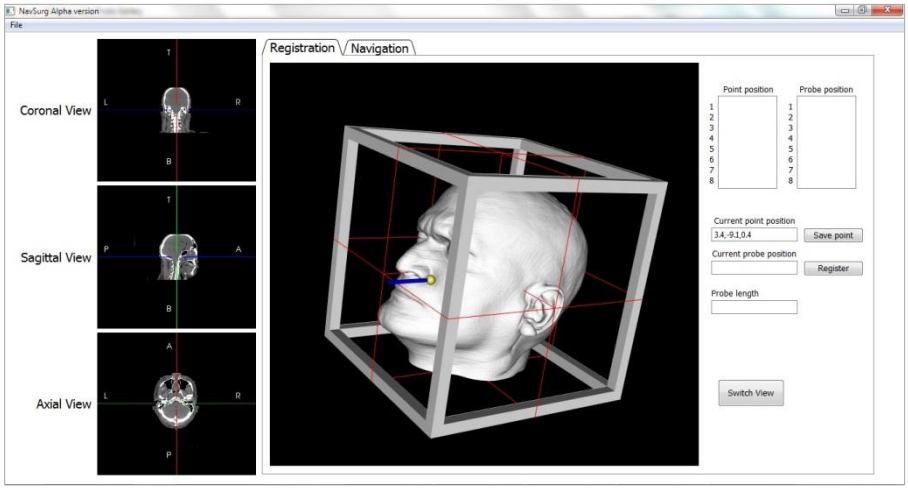

Figure 2.1: Multiplanar views of brain images. Top left: coronal, middle left: Sagittal, bottom left: Axial, right: the result of stacking images together.

2.2 System architecture

In the following section, the components related to IGS system, namely registration, tracking, and visualization will be further explained.

2.2.1 Registration

Registration is the process of spatial and temporal alignment of two separate data sources. When the mathematical relationship between a point in one data source and the homologous point in another source is known, the data are considered registered. If that relationship can be reduced to a simple translation and rotation transformation, the

registration is considered rigid. Registration is one of the key components of IGS system because it brings together preoperative image data, intraoperative tracking information, the patient and the surgical instruments' coordinate. There are great differences on the technical approaches depending on the type of data to be matched. A comprehensive survey was done by many researchers [13-16] and we can categorize the registration into image-to-image registration and image-to-physical space registration according to different registration characteristics.

The field of registration has been dominated by the techniques of image-to-image registration, whether inter-subject registration, intra-subject registration, or inter-modality registration. In image-to-image registration, point-based registration [17-19] has the advantage to easily quantify the quality of the registration. However the greatest disadvantage is that it relies on point identification and is difficult to be used retrospectively. One of the solutions is using surface structures where surfaces are extracted from image sets and fitted together like a hat on a head [20, 21]. In a landmark paper by West et al. [5], a blinded evaluation of the accuracy of several retrospective image-to-image registration techniques was performed. In order to ensure blindness, image sets were made available to researchers in the field. The participants could use their own techniques for registration of the image sets. After their results had been submitted, the gold-standard results were revealed and the registration quality was then quantified. This study showed that point-based and intensity-based image-to-image registration techniques performed significantly better than surface-based registrations. In Section 2.3, we will further explain the difference between feature-based and intensity-based registration and discuss the state-of-the-art image registration techniques.

In IGS system, image-to-physical space registration realizes the spatial transformation between both types of information for medical intervention. The most effective technique to register these spaces is to identify homologous features in both the image space and the physical space using stereotactic frames or fiducial markers. Frame-based stereotactic device was initially developed by Horsley & Clark [22] to give the patients' body a coordinate system. Although stereotactic frames [23, 24] provide a robust basis for registration, they are uncomfortable and invasive. Based on this idea, frameless stereotaxy was developed to replace the invasive stereotactic frame-based method. Frameless method refers to the anatomical landmarks on the subject or artificial markers attached to the subject. Such anatomical landmarks should be uniquely identified, distributed evenly over the image volume and carry significant morphological information of the image. Because of the limited good intrinsic points to serve as reference points, researchers have tried placing the artificial markers on the patient for use in registration. These artificial markers can be noninvasive and designed to stick to the skin [25] or invasively implanted into the bone [26, 27]. Registration based on these extrinsic markers is often automated and fast because they are easily detected in the images.

2.2.2 Tracking

Tracking is an essential feature to accurately determine the position of instruments relative to the patient anatomy during surgery. It consists of determining the relationship between the instrument, the anatomy, and the image coordinate frame. By rigidly mounting the tracking objects to surgical instruments, the instruments can be localized within the tracking system coordinate frame. The component that delivers this

information to the IGS system is called tracker or localizer. This tracking information is necessary to IGS system for accurate navigation and guidance. Currently available tracking systems use electromagnetic, optical, and mechanical tracking techniques. Because of the flexibility and performance, electromagnetic tracking and optical tracking are the main choice for IGS system [28, 29].

Electromagnetic tracking system [30, 31] uses an electromagnetic field generator and the surgical instruments are embedded with small electromagnetic coils. The magnetic field is generated by the field generator at a stationary base. The tracking of the relative position and orientation of the localization device is based on measuring the field strengths at the receiving coils. Although this method does not require a line of sight between the transmitter and receiver, it is sensitive to ferromagnetic material such as iron, cobalt, nickel, and steels. It has been reported that ferromagnetic material can create significant distortion in the operating room environment and cause translation errors up to 8.4 mm RMS and rotation errors up to 166° [32]. Optical tracking [33, 34] provides great accuracy and is not influenced by any nearby conducting or metallic objects. The object location would be measured by two cameras positioned at a defined distance from each other. It uses stereo vision techniques to determine the position of target objects. Optical tracking is divided into active and passive tracking. Active optical tracking is where the light transmitted from the object though LEDs. For passive tracking, the light is transmitted from an infrared light source at the optical tracking system and reflected by the markers. Since passive tracking offers simple tool construction, the active tracking is seldom used in operating room now [28]. A recent article [35] comparing optical and electromagnetic tracking systems mentioned that optical tracking has additional

advantages of higher accuracy. In Table 2.1, measurement accuracies of these tracking systems are summarized [36].

Tracking method	Company	Position accuracy (RMS)	Orientation accuracy (RMS)
Electromagnetic	Ascension Technologies Inc.	0.7-1.4 mm	0.5-1.0°
Optical	Northern Digital Inc.	0.1-0.15 mm	-
Mechanical	Immersion Corp.	0.23-0.43 mm	0.01°

Table 2.1: Typical accuracy measurements of tracking methods for IGS system.

2.2.3 Visualization

Visualization is one of the primary interfaces to provide a clear and accurate representation of all relevant data in a timely manner. Depending on the task to be performed and the nature of the target structures, the challenge is to determine how it should be best presented. Basic 2D visualization requires less computational power, so real-time update of the display can be achieved easily. Although for diagnostic procedures, 2D visualization is often sufficient, to guide interventional procedures, more complete visualization of 3D volume information is more useful and desirable. The two common techniques for 3D volumetric data rendering are surface rendering and volume rendering. Each rendering method provides different information depending on the needs of the surgeon.

2D visualization of the 3D volume

Conventional method of visualizing volumetric images is to present multiple images in slice-by-slice format. Multi-planar reformatting is a common technique of visualizing medical image data which generating 2D planes that cut through the volumetric 3D data.

It is a simple method because the image data have been acquired and saved in a sequential collection of parallel 2D slices. Presentation of multi-planar images often uses three separate panels, one for each orthogonal orientation, namely axial, sagittal, and coronal views. By simultaneously displaying the three orthogonal views, surgeon can have a quick observation of the volumetric data in IGS system. Although the information provided is limited to the data contained in the specific planes, its main advantage is speed since only limited data are processed and displayed.

Surface Rendering

3D visualizations are often generated using surface rendering because of the comparatively small amount of data necessary to render the object in three dimensions. It is done by rendering its surface opaque while making the rest of the image volume transparent. Surface rendering works well in instances where there is a relatively large and clearly defined surface like bones. However the potentially important information about anatomical structures and pathologies inside the surface-rendered structure is lost. Generally, surface rendering techniques require segmentation of the image volume. The most common technique for extracting the boundaries from volume data is the iso-surface. This is often done in combination with thresholding. Once the boundary has been clearly identified, the contours of the segmented volumes can be built as a polygonal mesh. One of the common algorithms for surface rendering is the marching-cubes algorithm [37]. The inputs are the triangular meshes extracted from the image volume representing the surface of the anatomical structures of interest.

Volume Rendering

Volume rendering involves projection of rays to the objects within the 3D field of view. It differs from surface rendering in that it does not require surface extraction of the image data. For each voxel that the ray encounters, a lookup table is used to map the voxel values into the resulting object properties (e.g., color and transparency information). Once the assigning process is accomplished, then the "camera" perspective must be set since the data are displayed as the view from a camera and the volumetric data can be displayed in an arbitrary manner. Rendering of every voxel allows for visualizing natural geometrical structures and the representation of the complete volume data. It is best suited for complex anatomy with fine details like the brain. Although volume rendering offers great flexibility, there is a drawback on performance due to the large amounts of data required to create an accurate visualization.

2.3 Medical image registration in IGS: A summary

Registration is a general term that is used to describe the process of developing a spatial mapping between sets of data. In image processing, comparing or combining the information content of images is achieved by investigating the relationship between two or more images. The task of establishing this correspondence is called image registration. Such a procedure can find applications in many diverse fields, such as medical image analysis (e.g. diagnosis), neuroscience (e.g. brain mapping), computer vision (e.g. stereo image matching for shape recovery), astrophysics (e.g. the alignment of images from different frequencies), military applications (e.g. target recognition), etc. However, a

major application of this is in the field of image-guided surgery through image registration.

A typical image registration framework consists of three components: a similarity measure that quantifies the quality of alignment; geometric transformations that align the geometric difference of images; and an optimizer that search the optimum transformation as quantified by the similarity measure. Figure 2.2 illustrates these components. The main idea is to search iteratively for the geometric transformation that applied to the floating image by optimizing (i.e. minimizes or maximizes) a similarity measure. As shown in Figure 2.2, the floating image is compared with the reference image using a similarity measure. The similarity measures can be based on the distances between certain homogeneous features (e.g. landmark points) or differences of image intensity information in the two image sets. Hence we can classify the medical image registration techniques into feature-based and intensity-based methods. Differences in image registration techniques are explained in greater detail in the following section. Based on the similarity measure, new transformation parameters are estimated to provide a better registration result from the two image sets. The floating image is then interpolated and transformed with the new parameters and again compared with the reference image to allow further improvement in transformation parameters by the optimization steps. This process is repeated until no further improvement is possible. The optimum transformation parameters will be used to register the floating image to the reference image.

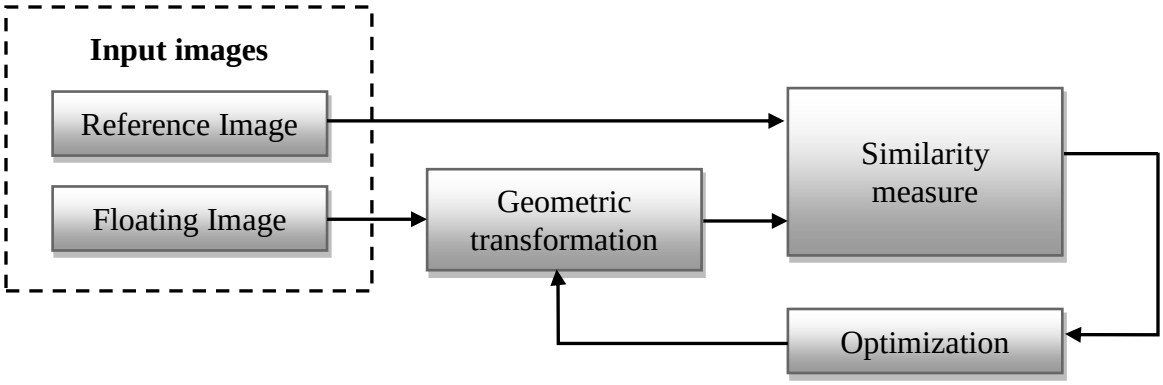

Figure 2.2: Image registration framework.

A number of reviews and surveys have been published in this area [13, 14, 38]. In these surveys, excellent overviews and categorizations of image registration techniques were provided. From the methodology point of view, registration algorithms can be classified based on certain homogeneous features or image intensity values. The following section presents the technical background of these methods.

2.3.1 Feature-based registration

Feature-based registration involves identifying the corresponding landmarks or features and applying the transformation function that is required to spatially match these features efficiently. These features can have a clear morphological meaning (e.g. the anatomical landmarks of the human brain, fiducial markers in imaging modalities, etc.), or they can be of geometrical interest only (e.g. lines, corners, surfaces, etc.). A preprocessing step is usually needed to extract these features manually or semi-automatically, which makes the performance of the algorithm heavily depends on the feature identification. In feature-based registration, it can be subdivided into landmark-based and segmentation-based methods.

Landmarks can be intrinsic (anatomical or geometrical salient points) or extrinsic (artificial markers attached to the subject) points that are identifiable in both image modalities. Fiducial markers are usually used as a "gold standard" for brain image registration because they are easily detected in the images. The registration based on these extrinsic landmarks is often automated and widely used in IGS system, where registration efficiency is one of the primary concerns. In registration based on anatomical landmarks [19], the corresponding morphological feature points are usually identified by a trained medical physician. The accuracy of the registration result is highly dependent on the user's experience to accurately identify the anatomical landmarks. Due to the small number of points which can be used as stable anatomical landmarks, registration algorithms are usually apply with rigid transformations. On the other hand, geometric landmarks are the salient points with some geometrical property which can be segmented automatically such as corner points, intersection points, and local extrema. The accuracy of registration may depend on the precision of the segmentation algorithms. Although identification of three landmark points will be sufficient to establish the rigid transformation, it is usual to use more than three points to average out the feature identification error.

Segmentation based methods offer wide range of possibilities for solving the registration problem because boundaries or surfaces in medical images are normally more distinctive than landmark points. The curve and surface segmentation based methods can be categorized into rigid model and deformable model based. The term rigid model is used to simply describe that the same corresponding features are extracted from both images. These features are to be registered by fitting algorithms. One of the most well-

known and successful surface fitting techniques is the head hat algorithm [39]. This approach relies on a simple segmentation step to extract two equivalent surfaces from the imaging modality. The registration is determined by iteratively transforming the hat surface with respect to the head surface until the closest fit of the two surfaces is found. Other popular rigid model based techniques include hierarchical chamfer matching [40] and the Iterative Closest Point (ICP) algorithm [41]. Rigid based registration methods are well suited for intra-subject registration because the features which are being matched are generally the same as they are obtained from the same individual.

Deformable model based methods are much more applicable for inter-subject registration. The extracted structure (e.g. surfaces or boundaries) from one image is elastically deformed to fit the second image. The deformation process is always done iteratively, small deformations at a time and restricted by elastic modeling constraints applied onto the segmented curve or surface. Therefore it is best suited to find local curved transformations between images, instead of finding global rigid transformations. Deformable curves as "snakes" or active contours were proposed by Kass [42] to provide effective contour extraction techniques. Active contours are energy minimizing splines driven by both internal and external energy. It can be easily manipulated and self-adapting in their search for a minimal energy state. Thus they are popular in image segmentation and shape modeling[43], boundary detection and extraction [44], object tracking and analysis [45], and deformable registration [46, 47].

2.3.2 Intensity-based registration

Intensity based registration methods also referred to as voxel based methods. These methods directly utilize the intensity information within the image and fully automated without requiring segmentation or extensive user interactions like feature-based registration. These approaches are generally more flexible and more robust in the situation where features are difficult to determine as intensity-based registration operate on the full image content rather than a representative structure, such as landmark points or surfaces. In intensity-based image registration, a cost function or similarity measure is defined, and the image datasets are iteratively transformed until the cost function is optimized. There are several well established intensity-based similarity measures used in image registration such as intensity differences, intensity cross-correlation and information theory.

The methods of minimizing the intensity difference are usually based on the sum of squared differences (SSD) between two images. SSD [48] is suitable for monomodality image registration (e.g. serial MR registration) when the intensity differences among the data are sufficiently small. The assumption behind the SSD computed from the voxel intensity is that the corresponding structures in both images should have identical intensities. Thus, SSD measure is very sensitive to a small number of voxels that have very large intensity differences between reference image and floating image. This undesirable property obviously can lead to false monomodality image registration. Cross correlation technique [49, 50] were introduced to help overcoming the problem of the differing levels of intensity values between images. The registration is obtained by maximizing the similarity between images of the same object that may be

different due to various acquisition conditions. Cross correlation is based on the assumption that there is a linear relationship between the intensity values of two images. However it is not always true for complex multimodal images. Therefore the correlation techniques cannot always achieve reliable registration results in multimodality registration.

Information theory

The basics of information theory were laid by Claude Shannon in his paper "A Mathematical Theory of Communication" [51]. Using the probability theory, Shannon defined measures such as entropy (*H*, the measures of the uncertainty on the occurring of a random variable) and mutual information (*MI*, the measure of the correlation between two signals). In this section, we present these two key concepts of information theory and explain their use as similarity criteria in image registration. For a good reference of the information theory, refer to Cover et al. [52] and Pluim at al. [53].

Shannon entropy is commonly used as a standard information measure in many engineering areas, where information is simply the result of a selection from a finite number of possibilities. The entropy *H* of a discrete random variable *X* with values in the set $X = [x_1, x_2, \ldots, x_n]$ is defined as:

$$H(X) = -\sum_{x \in X} p(x) \log p(x) \qquad (1)$$

where *p(x)* is the probability distribution of random variable *X*. The Shannon entropy can also be calculated for an image on the distribution of image intensity values by counting the number of times each grey value occurs in the image and dividing those numbers by

the total number of occurrences. A low entropy value will be yielded by an image consisting of almost a single intensity, which is an image containing very little information. An image consisting of several different intensities will have a high entropy value. If we consider another random variable Y with probability distribution $p(y)$ corresponding to values in the set $Y = [y_1, y_2, \ldots, y_m]$, the joint entropy of X and Y is defined as:

$$H(X,Y) = -\sum_{x\in X}\sum_{y\in Y} p(x,y)\log p(x,y) \tag{2}$$

where $p(x, y)$ is the joint probability. Joint entropy provides a method to measure the amount of information in the combined image. If the two images are completely independent, their joint entropy will be at a maximum value. The more similar the images are, the lower their joint entropy compared to the sum of the individual entropies. The concept of joint entropy can be visualized using a joint histogram calculation from a floating image and a reference image, which are shown in Figure 2.3. The left panel is generated from the images when aligned, the middle panel was rotated 1°, and the right panel was rotated by 5°. In image registration, when the images are correctly aligned, the joint histograms have tight clusters, and the joint entropy is minimized. These clusters disperse as the images become less well registered, and correspondingly, the joint entropy is increased. Besides the Shannon's entropy, other different entropy have been used in image registration are Rényi entropy [54, 55], Jumarie entropy [56, 57], Tsallis entropy [58-60] and Havrda-Charvat entropy [61, 62].

The basic idea of mutual information (MI) [3, 6, 63] comes from information theory which measures the statistical dependence between two random variables or the

amount of information that one random variable contains about the other. For discrete random variables X and Y with their respective marginal probability distributions $P_X(x)$, $P_Y(y)$ and joint probability distribution $P_{XY}(x, y)$, *MI* is defined as:

$$MI(X,Y) = \sum_{x,y} P_{XY}(x,y)\, log \frac{P_{XY}(x,y)}{P_X(x)P_Y(y)} \tag{3}$$

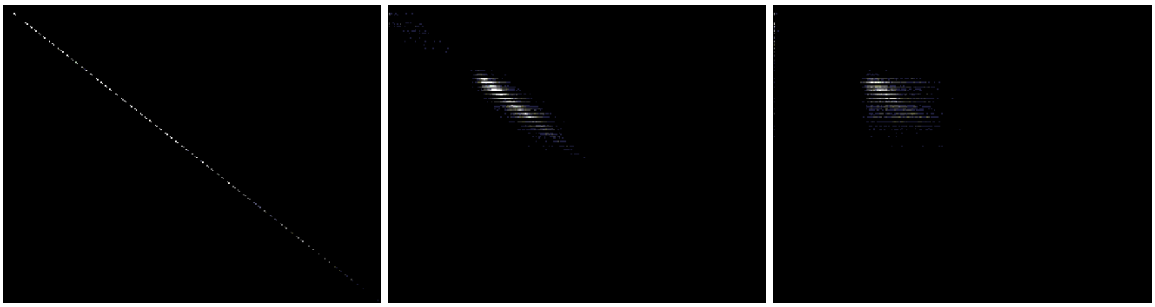

(a) (b) (c)

Figure 2.3: Example 2D joint entropy histogram of (a) Identical MR images of the head, (b) floating image was rotated 1°, and (c) floating image was rotated 5°.

MI is also related to the joint entropy information theory by the following equation:

$$MI(X,Y) = H(X) + H(Y) - H(X,Y) \tag{4}$$

If X and Y are two images that are geometrically related by the registration transformation, the terms $H(X)$ and $H(Y)$ are denoted as the entropy of the reference image and floating image respectively, while $H(X,Y)$ is the joint entropy of both images. The equation (4) can be interpreted that maximizing MI will tend to find as much as possible of the information that exists in both images so that at the same time they explain each other well. The relationship between all the above measures can be expressed by the Venn diagram, as shown in Figure 2.4. The advantage of MI compared

with other similarity measure is that the image intensities corresponding to the same object between different images are statistically related. It does not depend on any relationship between the intensities in the floating image and reference image like cross correlation technique [50, 64]. Therefore the applicability of MI registration is widely applied in medical image registration problems, covering monomodality as well as multimodality registrations [65, 66]. Because of the statistical notion of MI measure, it is sensitive to the amount of overlap between both images. Normalized mutual information (NMI) measures were introduced by Studholme et al. [67] to overcome this problem. This is shown in equation (5):

$$NMI(X,Y) = \big(H(X) + H(Y)\big)/H(X,Y) \tag{5}$$

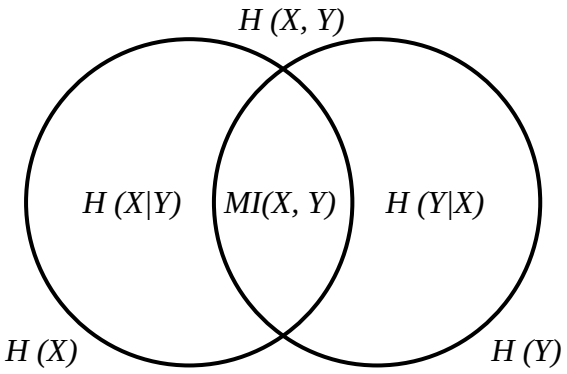

Figure 2.4: *H(X)* and *H(Y)* denote the separate entropy values of image *X* and *Y*, respectively. *H(X,Y)* is the joint entropy of the image intensities. Correct registration of the image is assumed to be equivalent to maximization of the mutual information M*I(X,Y)* of the images.

2.3.3 Review of mutual information variants

MI is a similarity measure that was pioneered both by Collignon et al. [3] and by Viola et al. [4]. Within a few years, it became the most investigated measure for medical image registration and the number of papers published related to MI based registration has grown rapidly. MI registration has received so much attention that, a few years after being proposed for image registration, a comprehensive survey based on mutual information was presented by Pluim et al. [53] addressing almost 160 papers on that topic. This section presents the survey and review of recent literature concerning various improvements on MI based image registration. The intention of this section is not to exhaustively evaluate all existing techniques, but to highlight a few approaches that inspire this research development. Because of the sheer volume of available papers, we narrow our analysis to medical image registration and incorporation of spatial information into MI algorithm.

2.3.3.1 Quantitative-qualitative measure of mutual information (Q-MI)

In paper [68], Hongxia et al. proposed a similarity measure to consider not only the probability of image intensity, but also the utility of each voxel in calculating the MI of two images. This method was motivated by Belis at al. [69] that different voxels, even having the same intensity, should be treated differently because they may have different characteristics and utilities on image registration. The utility of each voxel in an image can be determined according to the regional saliency value calculated based on scale-space map [70]. The salient voxels will have higher utility values and they will contribute more in measuring the MI of the two images under registration.

By denoting the two images under registration as the reference image *R* and the floating image *F*, and letting I_R and I_F be the intensity values of the two images, respectively, the Q-MI incorporates the qualitative aspect of image into the measure of MI as follows:

$$QMI(R,F;U) = \sum\sum u(I_R,I_F)p(I_R,I_F)\log\frac{p(I_R,I_F)}{p(I_R)p(I_F)} \quad (6)$$

The optimal transformation between both images can be obtained by maximizing the Q-MI value. In equation (6), the marginal and the joint image intensity distributions, $p(I_R)$, $p(I_F)$ and $p(I_R, I_F)$, can be estimated by simply calculating the marginal and the joint histograms of images within the overlap region. $u(I_R, I_F)$ is a joint utility for each intensity pair (I_R, I_F), which is used to determine the amount of useful information that one image contain about another.

2.3.3.2 Combined gradient intensity-based registration (GI-MI)

This adaptation of the MI measure was proposed by Pluim et al. [71]. This is one of the early works that focused on incorporating spatial information into MI-based image registration. The authors extended MI measures (both standard and normalized MI) to include spatial information that is present in each of the images. This extension is accomplished by multiplying the normalized MI with a weighting function based on gradient information. The authors highlighted that image gradients by themselves have been shown to be useful registration criteria [72] because a strong gradient signify the transition of tissues, which provide high information value.

For a volume image, the gradient vector is computed for each sample point *x = [x1, x2, x3]* where each component is the gradient in one of the image dimension. It is worth to mention that the gradient term is based not only on the gradient magnitude, but also on the orientation of the gradients. The gradient angle $\alpha_{x,y}\ (\sigma)$ is calculated according to the following expressions:

$$\alpha_{x,y}(\sigma) = \arccos \frac{\nabla x(\sigma).\nabla y(\sigma)}{|\nabla x(\sigma)||\nabla y(\sigma)|} \tag{7}$$

where $\nabla x(\sigma)$ denoting the gradient vector at point x of scale σ and $|\cdot|$ denoting magnitude. Since the algorithm interested to include the strong gradients that appear in both images, the gradient weighting function *G(A,B)* is calculated by multiplying the angle function with the minimum of the gradient magnitudes:

$$G(A,B) = \sum_{(x,x')\in(A\cap B)} w\left(\alpha_{x,x'}(\sigma)\right) min(|\nabla x(\sigma)|, |\nabla x'(\sigma)|) \tag{8}$$

Finally, the proposed registration measure becomes

$$MI_{new}(A,B) = G(A,B)MI(A,B) \tag{9}$$

2.3.3.3 Region mutual information (RMI)

The RMI proposed by Daniel et al. [1] is an extension of MI that efficiently takes regions of corresponding spatial information into account. Due to the reason of MI treats images as 1D signal, extending the dimensionality of the histograms is one of the logical ways to extend MI. However the main drawback of increasing the dimensionality is more samples are needed to populate the space to get a reasonable estimate of entropy and it's

computationally expensive. Therefore as the size of the neighborhood increases, the authors decouple the entropy calculation by projecting the data onto each of the *d* new axes, and summing the entropies along each dimension. In the formulation of RMI, each data point represents a pixel and its neighborhood as depicted in Figure 2.5a. The proposed algorithm proceeds as follows:

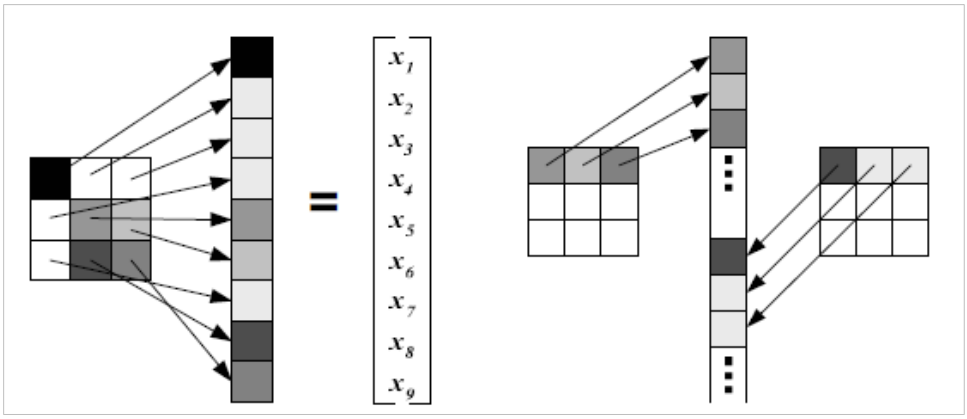

(a) (b)

Figure 2.5: (a) An illustration of the relationship of its data point. (b) The co-occurrences of the pixel points in corresponding image neighborhoods. [1]

1. Given two images, create a vector v_{ij} representing the co-occurrences of the pixels and their neighbors for some specified square radius *r* as shown in Figure 2.2b. This vector is now a point p_i in a *d*-dimensional space.
2. Given radius *r* and *m x n* images, a distribution of *N = (m-2r) (n-2r)* points represented by a *d X N* matrix is obtained.
3. Subtract the mean from the points so that they are centered at the origin.

$$P_0 = P - \frac{1}{N}\sum_i^N p_i \tag{10}$$

4. Calculate the covariance of the points.

$$C = \frac{1}{N} P_0 P_0^T \tag{11}$$

5. Estimate the joint entropy as: $H_g(C)$
6. Estimate the marginal entropies as $H_g(C_A)$ and $H_g(C_B)$ where C_A is the $\frac{d}{2} X \frac{d}{2}$ matrix in the top left of C and C_B is the $\frac{d}{2} X \frac{d}{2}$ matrix in the bottom right.
7. Calculate the $RMI = H_g(C_A) + H_g(C_B) - H_g(C)$

2.3.3.4 Conditional mutual information (cMI)

Because of the calculation of MI is typically based upon a global joint histogram, Dirk Loeckx et al. [7] proposed conditional mutual information (cMI) as a new similarity measure using a local estimation of the joint histogram for nonrigid image registration. The authors regarded the spatial coordinates of pixels in the reference image as prior known conditions. Similarly to RMI, the conditional probability distribution is also extending the joint histogram with a spatial dimension representing the spatial distribution of the joint intensities. Hence cMI $I(R,F|X)$ between the reference and floating intensity distributions R and F given the spatial distribution X is expressed as:

$$I(R,F|X) = H(R|X) + H(F|X) - H(R,F|X) \tag{12}$$

Following this formulation, cMI calculates the information that is shared between (R,F) but not available in X. The cMI measure was incorporated in a tensor-product B-spline registration algorithm [73], using the same kernel to calculate the weighted average of the

B-spline deformation coefficients and for the spatial distribution of the joint intensities over the joint histogram.

2.3.3.5 Spatial encoding mutual information (SEMI)

Xiahai Zhuang et al. [74] proposed a unified function to encode the spatial information into the computation of joint probability distribution function (PDF). They suggested two points for improving MI in nonrigid registration. The first idea is that to create the global and local intensity class linkage. The local estimation was mixed with the global estimation under a weighting function. Based on this idea, the authors introduced a new parameter, $\lambda \in [0, 1]$ indicating the trade-off between the local information and global information, to provide a general weighting scheme for them such that $\omega = \omega(\lambda)$. By valuing $w(\lambda)$, the importance of the local information from the global information can be differentiated. Another idea is to encode the fine detail of spatial information within the local estimation of the joint probability distribution to provide important information for correcting local misalignment. This encoding is achieved by weighting the contribution of pixel pairs to the joint histogram table according to their spatial coordinates:

$$H(r,f) = \sum_{x} \omega_r\big(I_r(x)\big)\, \omega_r\left(I_f(x)\right).\varepsilon(x) \tag{13}$$

$\varepsilon(x)$ is the weighting function to encode spatial information at coordinate x. By using a constant value, $\varepsilon_x = 1$, equation (13) becomes the conventional estimation method.

2.3.3.6 Higher-order mutual information

Ruekert et al. [75] proposed an extension of the MI framework which incorporates spatial information based on higher-order image structure into the registration process. The entropy of images can be calculated by using the probability of co-occurrence of intensity pairs within a neighborhood in the image. For example, the second-order entropy of an image can be defined as:

$$H_2(X) = -\sum_i \sum_j p(i,j) \log p(i,j) \tag{14}$$

p(i, j) denotes the joint probability that a voxel has intensity *i* while its neighboring voxel has intensity *j*. The joint probability *p(i, j)* can be estimated from a co-occurrence matrix between neighboring voxel pairs in a single image. The authors have chosen a neighborhood which is defined by the six nearest neighbors of each voxel. In contrast to the computation of first-order approximations of the marginal and joint entropies which only requires the calculation of the 2D joint histogram, the computation of second-order approximations of the marginal and joint entropies requires the calculation of the 4D joint histogram of both images. Due to the high dimensionality of this histogram, the authors have limited the number of histogram bins to 16 bins per dimension for the calculation of second-order information measures. The results showed that 4D histograms with 16 bins per dimension represent a good compromise between total number of bins and the average number of samples per bin.

2.3.3.7 Local linear embedding and hybrid entropy (LLE-HE)

In paper [76], Qi Li et al. explored the spatial information solution by including ordinal features (OFs) into MI registration measure. OFs are defined based on the qualitative relationship between two image regions and it is proven useful in the pattern recognition task [77]. The OFs with different orientations are extracted by Sum-Difference Ordinal Filters (SDOFs) [78] to represent the spatial information between neighboring pixels. However the extracted OFs with different orientations are high dimensional and contain a lot of unessential redundant information. In order to minimize the redundant information and reduce computational cost, LLE [79] algorithm is used to reduce the dimensionality and different directional OFs are needed to fused together by using Zhang's inverse mapping method of LLE [80]. In this final fused OF, redundant information is minimized and complementary information is reserved and emphasized.

Similarly to cMI, the registration algorithm is also extending the joint histogram with a spatial dimension representing the spatial distribution. A similarity measure based on hybrid entropy is calculated between the reference and floating intensity distributions R and F given the spatial distribution X:

$$HE(R,F,X) = H(F) + H(R,X) - H(R,F,X) \tag{15}$$

During the registration process, the information shared by (R, X) is always unchanged, which has no influence on the registration results except that computational time is increased. Based on the above analysis, R and X are joined together and the unity (R, X) is registered with F. $HE(R,F,X)$ incorporate the spatial information into MI and does not include unchanging information. So $HE(R,F,X)$ can efficiently measure the intensity

information and spatial information in both of medical images and effectively reduce the influence of noise by OF.

2.3.4 Performance comparison and discussion

The performance comparison between the reviewed mutual information variants are discussed in this section. Note that, in our survey in Section 2.3.3, we focused only on those MI variants that incorporate spatial information. Table 2.1 therefore gives the summary of performance comparison between the reviewed MI variants presented in sections 2.3.3. We use the – symbol to denote that the authors do not provide any information in terms of algorithm performance. Mutual information is based on a single pixel joint probability model. Several causes for misregistration have been mentioned in the Section 1.2. To rectify these shortcomings, Pluim et al. [53] also mentioned the challenges to "correct" the assumption of Shannon entropy that the intensity values of neighboring pixels are uncorrelated. According to the reviewed methods, we categorize them into two main approaches, (1) dimensionality approach and (2) hybrid approach. Because MI technique treats each image as 1D signal, attempts have been made by many researchers to incorporate spatial information by extending the dimensionality of the histograms. These methods were effective for the improvement of registration quality. However the curse of dimensionality is an important limitation as the improved performance comes at the cost of increasing the computational complexity of cost function calculation. Hybrid approach on the other hand does not suffer from such issue. It is an alternative way to incorporate spatial information by combining the MI similarity measure with the additional term that describes spatial information. A critical look at Table 2.2 shows the hybrid approaches provide similar registration accuracy with the

dimensionality approaches with low computational cost for rigid registration. Thus, in view of the fact that the hybrid approaches offer some advantages over the dimensionality approaches as highlighted above, our focus is looking at the possibility of developing a simple method to combine multiple spatial features into the MI similarity measure by using hybrid approach.

	Q-MI	GI-MI	RMI	cMI	SEMI	Higher-order MI	LLE-HE
Dimensionality/ Hybrid	Hybrid	Hybrid	Dimensionality	Dimensionality	Hybrid	Dimensionality	Dimensionality
Rigid/ nonrigid	Rigid	Rigid	Rigid	Non-rigid	Non-rigid	Non-rigid	Rigid
Spatial information	Saliency measure to represent the utility pixel	Gradient information	High dimensional histogram	Spatial dimension in joint histogram	Pixel-wise spatial encoding	Co-occurrence matrix	Ordinal features
Optimization	Multi-resolution framework	Powell's method	-	Quasi Newton method	Gradient ascent method	-	Particle swarm optimization method
Computational cost	Low cost	Low cost	174sec $O(n^2d^2)$	10610sec number of evaluations per iteration: $\nu \times 3(n_i+1)$	-	-	156.2msec
Accuracy	1.07mm (CT/MR) 2.64mm (PET/MR)	1.37mm (CT/T1) 2.43mm (PET/T1)	1.25mm (CT/X-Ray) 92% (successful rate)	Surface distance: 2.5-5mm (CT/MR)	4.64±1.36mm (simulated T1/T2)	0.58mm (simulated T1/T1)	> 90% (success rate)
Limitation/ issue	-	Gradient term fluctuate due to various imaging conditions	Higher computational complexity due to higher dimension	Higher computational complexity due to higher dimension	-	Only include one neighbor pixel which leaves out a great deal of spatial information	Higher computational complexity due to higher dimension

Table 2.2: The comparison of the reviewed literature on the image registration.

2.4 Soft tissue deformation modeling

In order to provide spatial navigation and guidance, IGS systems rely on the assumption that rigid body transformation remains valid throughout the intervention. However studies have shown that this assumption is not always valid [8, 9] and the brain could deform after the skull is opened and before the surgery is started. The overall accuracy of the IGS system is reduced, which are often unacceptable for many surgical applications. Thus the deformation needs to be accounted to maximize the effectiveness of IGS systems. A potential solution to the misalignment between the preoperative images and surgical situation is to simulate the deformations, and warp the preoperative images to reflect the real surgical scene. Recent studies have shown promising results to use biomechanical models to estimate displacements in order to update the preoperative images [11, 81-85]. The following section will describe various deformation modeling methods and its applications in soft tissue deformation.

2.4.1 Deformation modeling methods

At present, the modeling of soft tissue deformation has been widely studied. Essentially, they are applied in the field to simulate the deformation behavior of non-rigid objects due to external influences both in surgery planning [86, 87] and in real-time surgical applications [88, 89]. The methods for deformation modeling were developed based on the models ranged from heuristic approach to continuum mechanical approach. The first approach is a straight forward modeling method based on geometry of deformable objects. According to some predefined rules, the shape of the object is transformed by adjusting control points or shape parameters. However, in order to produce more realistic

models, they must be based on physical properties of soft tissues. As a result, the second approach implicitly is based on the hypothesis of the continuum mechanics models. Considering physical property of deformable objects, external forces, and environmental constraints on object deformation, the continuum mechanics model can be simulated with certain realism. In particular, the related work on modeling will be reviewed and compared in the following section.

2.4.1.1 Heuristic approach

The first class is based on purely geometric techniques. Generally, these techniques are computationally efficient, and they rely on the skill of the developer rather than on physical principles. Heuristic based geometric models can be divided into three categories, deformable splines, mass-spring model, and chain mail model.

Deformable splines

In the field of computer aided geometric design (CAGD), deformable splines serve to numerically obtain smooth and rounded curves, surfaces, or volumes. Among the different existent techniques are the Bezier curves and many other methods of specifying curves with a small vector of numbers, including: double-quadratic curves, B-splines, rational B-splines, non-uniform rational B-splines (NURBS), and β-splines. In these examples, the curve or surface is represented by a set of control points. By moving the control points, the form of the respective curve, surface, or volume changes in a predictable manner. This parameter-based object representation is computationally efficient and supports interactive modification. However, this level of control is sometimes a disadvantage due to the precise specification or modification of curves or

surfaces can be laborious. Even a perceptually simple change may require adjustment of many control points. Textbooks by Bartels et al. and Farin provide comprehensive coverage of curve and surface modeling with splines [90, 91].

Mass-spring model

Mass-spring model is one of the techniques that have been used effectively for deformable object modeling. In this model, deformable objects are represented by a mesh of springs or spring damper elements which are connected to a large number of mass points. The spring is often linear, but non-linear springs can be used to model soft tissues that exhibit inelastic behavior. The spring forces and the motion of a single mass point are governed by the Newton's second law. If a point x has mass m, then the right hand side is the forces acting on the mass point:

$$m_i \ddot{x}_i = -\gamma_i \dot{x}_i + \sum_j g_{ij} + f_i \tag{16}$$

where γ is the damping coefficients, g_{ij} is the force applied on mass i, and f_i is the sum of other external forces like gravity or user applied forces acting on mass i. Due to their computational simplicity, they have been widely used in surgical simulation where large and complex deformation must be present without sacrificing real-time response to user interaction.

Pioneering work has been reported by Terzopoulos et al. in which they created non-linear mass-spring models of the facial soft tissues [92]. Montgomery et al. describe a surgical simulation software library that uses mass springs for a number of different modeling simulations [93]. Bucholz et al. determined the average shift of structures into three classes – low, moderate, and high shift and modeled the response of the brain to

surgery by using mass-spring model and intraoperative ultrasound [94]. Skrinjar and Duncan used mass spring model and applied Kelvin solid property model to describe intraoperative brain deformation. However, this research group abandoned mass-springs models for finite element models in the subsequent work due to the difficulty to apply accurate model parameters and the limitation of physical realism of mass-springs models [95].

Chain mail model

The chain mail model is similar to mass-spring type model. But instead of linking the different elements with springs, these are interconnected like links of a chain. It simulates a deformable object by the interaction between these chain elements. That is to say, the motion of every unit is associated with its neighboring units. Within a certain limit, each link can move freely without influencing its neighbors. When the stretching or compressing of two units has gone beyond the predefined limits, the deformation displacements are propagated directly to the corresponding adjacent links. To achieve an elastic relaxation behavior, the relative unit positions are adjusted to minimize the energy of the whole system. Just like the mass-spring model, the great advantage of the chain mail algorithm is its simplicity. So far, chain mail approaches have only been used successfully in real time for 3D objects consisting of very few elements [96].

2.4.1.2 Continuum mechanical approach

Continuum mechanical approach is an entirely different way to deal with the issue of deformable objects. It is based on the laws of continuum mechanics that considers the equilibrium of a solid body acted on by external forces. The deformation is a function of

these acting forces and the object's material properties. Because there is not possible to find a general analytical solution, a number of numerical methods are used to approximate the object deformation, with the two best known approaches being finite element methods and boundary element methods.

Finite element methods

The predominant technique used in continuum mechanics problems is the finite element modeling (FEM) method. Originally, FEM was developed to approximately resolve differential equations defined for a certain domain with some given corresponding boundary conditions. To do so, the deformable object is discretized into a finite number of elements and joined at discrete points called nodes. This model can be described using the constitutive, kinematic and dynamics equations, such as viscoelastic, fluid elastic, etc. Then, the displacement is approximated with polynomial equations over each element and the solution is subject to constraints at the node points and element boundaries. In the simplest linear case, the resulting system of equations can be represented as:

$$KU = F \tag{17}$$

where F and U are the externally applied force and nodal displacement vector, respectively, and K is the stiffness matrix describing the material properties. Once the equations are solved, the node displacement of each element can be calculated by interpolation using the shape functions. For the nonlinear material like soft tissue, the stiffness matrix depends on the displacement and the solution of deformation problem can become more complicated.

Most researchers apply the FEM to image-guided surgery have focused on linear-elastic models of the brain. Skrinjar et al. used linear elasticity to deal with the problem of brain shift during craniotomy based on surface displacement [95]. Ferrant et al. tracks the key surfaces of objects like cortical surface and the lateral ventricles to infer volumetric deformation field using a linear elastic biomechanical finite-element model [97]. Clatz et al. also used a linear elastic model to predict the gravity-induced deformation of the brain during Parkinson's disease procedure [98]. Wittek et al. introduced a non-linear viscoelastic model suitable for real-time surgical procedures [84]. The research group based at Dartmouth College has been extensively use porous media model to representing the brain in a series of porcine and human studies [9, 99-101].

Boundary element model

Boundary element modeling (BEM) is another method which is similar to FEM. However all computations are done on the surface instead of the whole volume. This offers significant advantage in terms of computational efficiency over the FEM because it reduces the three dimensional problem (volume) to two dimensions (surface). As for the practical effects, this also means that only the surface of an object has to be discretized into patches or boundary elements. Furthermore, every node of this boundary mesh actually has a direct influence on all the other nodes. In the simplest linear case, the resulting system of equations can be represented as:

$$HU = GP \tag{18}$$

where the influence matrices H and G are much smaller than the stiffness matrix K in the FEM case. U and P are the nodal displacemensst and surface force vectors, respectively.

Ecabert et al. introduces the use of a 2D BEM combining elastic and fluids materials to compensate for the brain shift occurring during surgery [102]. However this model only works for objects with homogenous material and non-linear equations can be difficult to express in BEM. Therefore it is less popular to be used in the soft tissue modeling for image-guided surgery.

2.4.2 Discussion

The above section has presented many of the techniques that have been used to compensating soft tissue deformation during image-guided surgery. These techniques range from the deformable splines to FE methods that approximate the full continuum mechanics model of brain deformation. Based on our literature search, the majority of the work completed to date has been focused on neurosurgery, they showed the ability of the models to predict deformation behavior, but they are not yet integrated into a system that could be used during surgery. Mass-spring model and FEM method are the main focus in deformation modeling research field. Mass spring model is a simple technique to model soft tissue deformation, compared with FEM technique. Due to their computational simplicity, they can be updated rapidly to display the dynamic behavior of the brain tissue. However, a significant challenge of mass-spring model is that proper values for the spring constants are difficult to derive from material properties, and so constitutive laws are difficult to express in the model. Furthermore brain tissues often undergo large deformations and their material properties are complex. For these reasons, FEM are preferable in our brain tissue deformation modeling research.

Chapter 3

Improved Nonlinear Point Set Registration by Uniform Curve Features Subdivision Technique

3.1 Introduction

Medical image registration is the process of spatial mapping between two images that differ in image acquisition time, image properties, or viewpoint and subsequently producing a result image that is informative. For example, in postoperative assessment, in order to verify the technical results of the procedure, it is necessary to locate changes from preoperative and postoperative images through image registration. They are also useful to combine the complementary information from structural and functional imagery, like magnetic resonance imaging (MRI) and position emission tomography (PET). Generally, image registration methods can be divided into intensity-based and feature-based methods as described in Section 2.1.2. For an overview we refer to [13, 14, 38], and the references cited therein.

In feature-based registration, the process of feature correspondence should remain stable and invariant regardless of any feature variations and noise. Furthermore, degradations such as noise and outliers significantly challenge the accuracy of registration result. Thus the most preferred features extracted in advance would be points as its coordinates can be directly applied to find correspondence. The "points" in point set registration are often features extracted from an image, such as the corner points, boundary points or intersection points. An example of point set registration is shown in

Figure 3.1. Given are two images, typically called the reference image *R* and the floating image *F*. The goal is to identify correspondences between two sets of points and determine the transformation that maps one point set to the other. Iterative Closest Point (ICP) [41] is a popular method for rigid point set registration due to its simplicity and low computational complexity. ICP is an algorithm employed to assign correspondences based on the closest distance criterion and finds the least-squares rigid transformation connecting the two point sets. The algorithm iteratively revises the transformation until it reaches the minimum distance. For images where curve and contour extraction are more appropriate, feature points will be derived based on its feature characteristics such as edges, which have local maximum gradient magnitude, ridges, crest lines, etc. Curve and contour based registration has been used clinically to register medical image volumes [49, 103-105].

For this chapter, feature-based registration will be investigated with nonlinear image deformation. One of the challenges faced by feature-based registration would be to determine which specific type of feature is desired for a given task and imaging type. For this reason, a point set registration method using points and curves feature is proposed, which has the accuracy of registration based on points and the robustness of registration based on lines or curves. The proposed method is using hybrid approach in feature correspondence stage. The extracted line or curve pairs are modeled by point sampling so that they are subdivided according to curvature and length of curves. Then the mechanism of uniform subdivision of curves segment ensures that the subdivided points can match the original curve as close as possible and fulfill the requirement of point set registration. The deformation between images is described by thin plate splines (TPS),

which validated to be more accurate over other nonlinear transformation functions and more consistent in registration process even the correspondences are noisy [106].

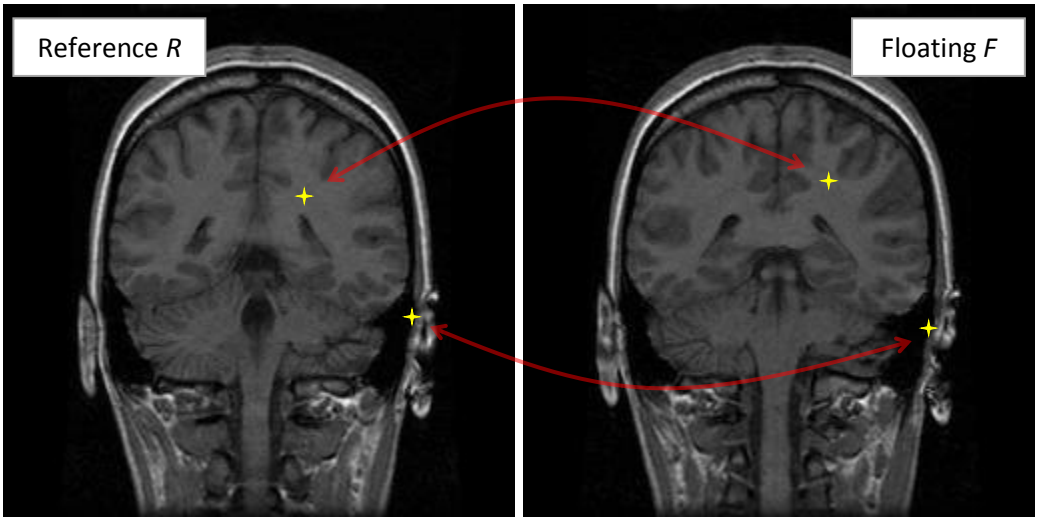

Figure 3.1: Illustration of point set registration based on specified feature correspondence. Given two sets of points, assign the correspondences and the transformation that maps one point set to the other.

3.2 Feature extraction

3.2.1 Point extraction

In point set registration, corresponding control points are identified by operator from both reference image and floating image. The corresponding points are also called homologous landmarks, to emphasize that they should represent the same feature in the different images. Generally, the point features in medical image registration are not only holding the geometry property, but also have some meanings in anatomy. Since control points are defined in pairs, the correspondence is straight forward. Automated approaches to feature extraction and feature correspondence are desirable but it is not the main focus of this chapter. Figure 3.2 shows the example of correspondence point pairs are

numbered in order to determine the relationship between reference image and floating image.

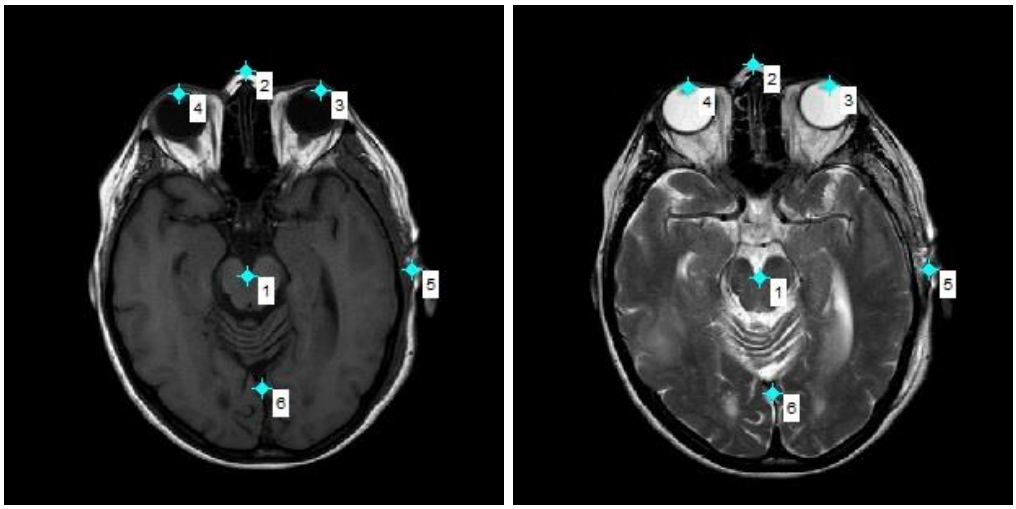

(a) (b)

Figure 3.2: An example of control points selection for (a) reference image and (b) source image which are numbered in pairs.

3.2.2 Curve extraction

In the process of medical image registration, matching a pair of curves differs from the purely curve alignment. Given a short curve and a long curve, the short curve must be matched as a part of the long curve with the curve alignment method. However this is not the case for image registration, where the curve is matched not only by aligning the coordinate but also by keeping consistent in the length of curve. The precision of curve extraction plays an important role in image registration, especially the start point and the end point because they decide the length of curve segment. As for our curve extraction method, the operator is required to mark a set of approximate points along the curve in

the image. The discrete points P_i (i=1,…, N) cannot represent curve feature precisely, so the curves need to be modeled and connected by line segment.

3.2.3 Uniform curve subdivision

There are numerous approaches proposed for alignment of curve features. The famous concepts are chamfer matching [40] and head hat matching algorithm [39]. In this section, we attempt a different method to match the similarity of curve features as close as possible. Based on the curve feature extracted earlier, whose start and end point correspond to the same image attribute, points will be interpolated in equal distance throughout the entire curve segment. The total number of interpolated points for related curve pairs will be equal, enabling the point correspondence to be determined easily. The process of modeling of a correspondence curve pair is same. Figure 3.3(a) and (b) are the result of our curve extraction method, where blue point is the approximate point along the curve feature and blue line is the modeled curve segment. Figure 3.3(c) demonstrates the curve subdivision result, where green points are the distributed points based on our proposed subdivision algorithm.

The process of curve subdivision is summarized below:

1. Calculate total distance between consecutive points P_i and P_{i+1} in P_i (i=1,…, N).
2. Specify *NumP* value to generate *NumP* points that interpolate a curve.
3. Calculate interval distance d by dividing the total distance with *NumP* value.
4. Calculate the distance *dist* from current point P_{curr} to the subsequent point in P_i.
5. If distance is enough (d <= *dist*), generate a new point between P_{curr} and P_{curr+1} in such a way that the distance between P_{curr} and new point is interval d.

6. If distance is not enough ($d < dist$), accumulate distance to the adjacent point. The curve segment in $[P_{curr}, P_{curr+1}]$ needs not to be subdivided, and then turn to step 4.
7. The curve is subdivided continuously until fulfill the constraint $i < N - 1$.
8. When the subdivision is stopped, the discrete points along the curve feature are obtained.

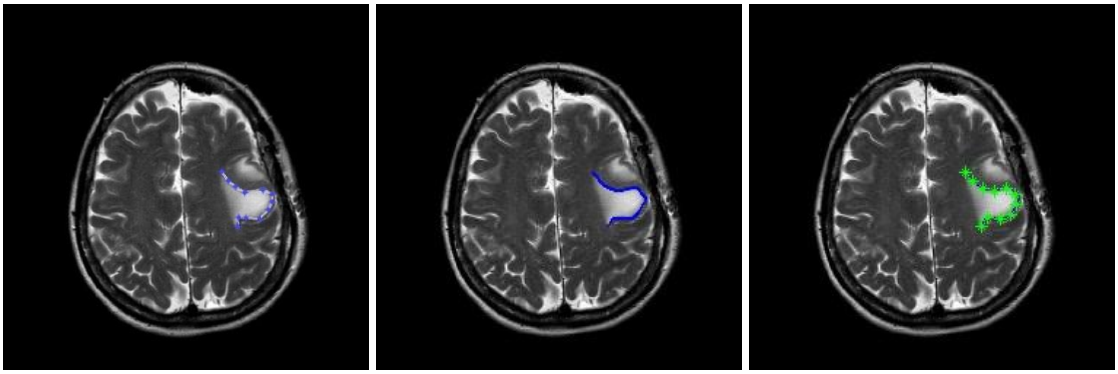

(a) (b) (c)

Figure 3.3: Landmark extraction and correspondence for uniform distributed points. (a) blue point is the approximate point along the curve feature. (b) blue line is the modeled curve segment. (c) the curve subdivision result, where green points are the distributed points based on our proposed subdivision algorithm.

3.3 Nonlinear Point Set Registration

The point set registration method involves identifying corresponding control points, matching the points set and estimating the image transformation from the locations of the control points. Due to the deformable nature of medical brain images, it generally has nonlinear geometric differences. At times, the local deformation is small and can be negligible. Hence using linear transformation is sufficient to register those images. When the geometric differences are huge and complex, nonlinear registration is needed to

provide more accurate transformation. Thin plate spline (TPS) is one of the most commonly employed transformation function for nonlinear image registration. It was first used by Goshtasby [92] in the registration of remote sensing images and then by Bookstein [107] in the registration of medical images. The main reason for choosing TPS in our algorithm is because it can produce a smoothly interpolated spatial mapping to address image deformation. The registration technique was implemented in MATLAB [108].

Given two sets of 2D control point pairs p_i and q_i , $i=1,2,\ldots,n$ in the reference and floating image respectively, TPS is capable of warping the points p_i arbitrarily close to points q_i (x, y) based on the function of:

$$f(x,y) = a_1 + a_2 x + a_3 y + \sum_{i=1}^{n} w_i U\left(\left\|(x,y) - p_i\right\|\right) \tag{19}$$

where

- n is the number of control points.
- the coefficients a_i characterize the affine part of the spline-based transformation, while the coefficients w_i characterize the non-affine part of the transformation.
- p_i is the i th landmark.
- $U(\| (x, y) - p_i \|) = \| (x, y) - p_i \|^2 \log (\|(x, y) - p_i \|^2)$ is the radial basis function.

The additional boundary conditions as shown in equation (20) must be satisfied to solve the equation (19).

$$\sum_{i=1}^{N} w_i = 0 \quad ; \sum_{i=1}^{N} w_i x_i = 0 \quad ; \sum_{i=1}^{N} w_i y_i = 0 \tag{20}$$

3.4 Experiment and results

Experimental results are presented in this section to demonstrate the application of the proposed method in coping with nonlinear deformations in clinical images. Image quality was inspected through subjective and objective quality assessments. Subjective quality assessment is the visual inspection to verify that the algorithms have successfully align floating image close enough to fit the reference image. There is no "golden criteria" in objective quality evaluation, but for demonstrating the validity of our method we choose root mean square error and mutual information to assess the results. The transformation performance was evaluated in the categories below.

a) Error parameter

The registration accuracy is evaluated by computing Root Mean Square Error (RMSE). MSE quantizes level of error between two images through the average of total sum of squared differences between both images. RMSE is the square root of MSE.

$$MSE = \frac{1}{MN}\sum_{i=1}^{M}\sum_{j=1}^{N}\left(x_{i,j} - x'_{i,j}\right)^2 \tag{21}$$

$$RMSE = \sqrt{MSE} \tag{22}$$

where M and N is the number of rows and columns in an image. *x* is the intensity value of grayscale image from 0 – 255.

b) Degree of matching

The degree of matching is calculated using mutual information. It is a statistical measurement between two images' content and checks the matched information rate. It is generally accepted to assess multimodal image registration.

$$MI(X,Y) = \sum_{x,y} P_{XY}(x,y)\, log \frac{P_{XY}(x,y)}{P_X(x)P_Y(y)} \tag{23}$$

There are two experiments were conducted to demonstrate the performance of the proposed approach. First, we used a pair of sagittal images from two different patients [109] to illustrate the inter-subject registration. The aim of inter-subject image registration is to establish correspondence between the brains of two different individuals. In the second experiment, we used pre-operative image and intra-operative image after resection [110], representing intra-subject registration with the presence of significant geometric variations. In image-guided interventions, tissue can move and deform between preoperative scans and the intervention. These deformations may either be due to voluntary movements or involuntary activities such as breathing and heartbeat, or may be induced by an intervention. Based on intra-operative information, intra-subject registration is applied for predicting deformation of adjacent tissues.

Shown in Figure 3.4(a) and (b) are the reference and floating image with geometric differences. The first row displays the sagittal images from two different patients, while the second row contains pre-operative image and intra-operative image after resection. Six salient point pairs were chose from both images, distributed all over the object of interest. For sagittal images, boundary of head was selected as curve feature and extracted from both images which interpolate a total of 31 control points. For another

dataset, brain tissue was selected as curve feature and interpolates a total of 45 control points. Figure 3.4(c) is the intensity difference between Figure 3.4(a) and (b). Given the locations of two point sets, we applied TPS algorithm to estimate the non-rigid transformation. The registration result is Figure 3.4(d), in which feature points are matched accurately. Figure 3.4(e) demonstrates the linear subtraction of the aligned image and reference image. The proposed method performs well and demonstrates visually accurate image alignment. The two mentioned quality metrics are utilized to quantify the registration performance, which are presented in Table 3.1.

In the first simulation, the proposed algorithm was successfully registered the image with an average intensity RMS error of 26.86 and MI value of 1.26. The proposed hybrid feature method achieved lower intensity error as compared with the point or curve feature alone. MI value also indicates that the proposed algorithm attained higher matched information rate of the image content. In the second set of simulation, the global distortions consist of non-rigid shape of the brain tissue and a removed region due to craniotomy. The proposed algorithm also successfully registered the image with an average intensity RMS error of 23.32 and MI value of 1.20. Hybrid feature approach is able to achieve better results as compared with the point or curve feature alone.

	Registration quality	**Point**	**Curve**	**Hybrid**
Inter-subject registration	**Error parameter (RMSE)**	35.0131	28.6687	26.8644
	Degree of matching (MI)	1.1391	1.1222	1.2567
Intra-subject registration	**Error parameter (RMSE)**	20.6699	27.0818	23.3145
	Degree of matching (MI)	1.1436	1.1191	1.2028

Table 3.1: The comparison of the registration performance based on point or curve features with the proposed hybrid method.

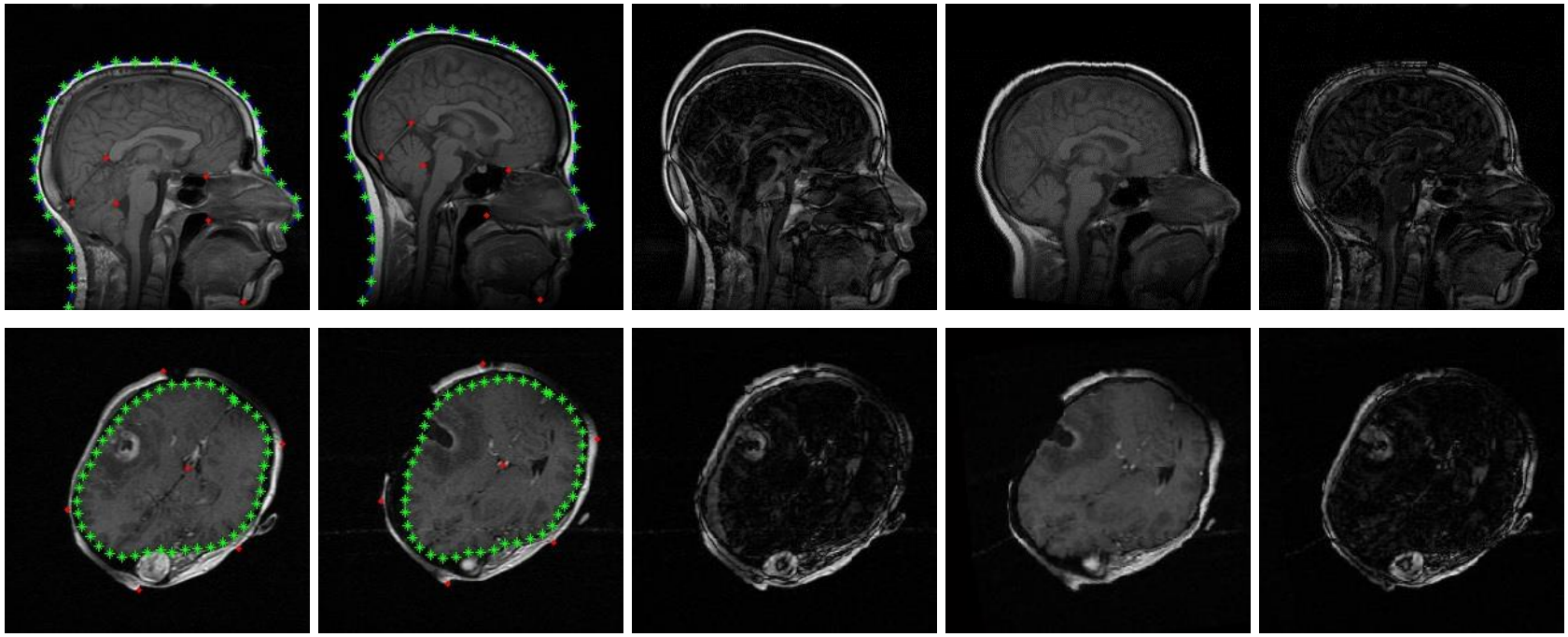

(a) Reference (b) Floating (c) Before (d) Registered (e) After

Figure 3.4: Image registration result. (a) Reference image and point set, (b) Floating image and point set, (c) difference between (a) and (b), (d) the registered floating image, (e) difference between (a) and (d).

3.5 Discussion and conclusion

Feature-based image registration is a spatial mapping process for determining the point-by-point correspondence between two images. The performance of point set registration algorithm depends on: 1) the performance of its feature correspondence step and 2) the performance of the transformation function that warps floating image to the reference image based on accurate feature correspondence information. Determining the specific type of feature for a given task and imaging type is a challenge faced by feature-based registration, as it was mentioned in the previous section.

Our contribution includes the following aspects. We introduce the idea that incorporating the curve feature into nonlinear point set registration, which has the accuracy of registration based on points and the robustness of registration based on curves. We consider the alignment of two features as point sets alignment. According to this idea, we proposed the extracted curve pairs are modeled by straight line, and then they are subdivided uniformly according to curvature and length of curves. Moreover, the combination of independent points and curve sampling points help to balance the general point distribution in point set registration. In designing the experiments, we have tried to simulate with what we consider to be two of the major obstacles facing by nonlinear registration algorithms: geometry variations and missing data between the reference and floating images. We tested the proposed method on inter-subject and intra-subject medical images and apply TPS transformation to describe nonlinear local deformation. The experimental results reveal that the image registration algorithm with combination of point and curve feature is a feasible approach and accurate registration is possible under a

significant amount of geometric and intensity variations. In addition, hybrid feature approach achieved better results as compared with the point or curve feature alone.

Chapter 4

Adaptation of Mutual Information Measure by Using Image Gradient Information

4.1 Introduction

In chapter 3, we have tackled the problem of spatial mapping using points and curves feature in point set registration. In this chapter, we will concentrate on rigid registration of multimodal images using voxel similarity measures. An information theoretic approach is presented for finding the correct alignment of an object in medical image. An advantage of the method presented in this chapter is that they require no preprocessing of the images, as the point set registration methods mentioned in the previous chapter. From a practical point of view, intensity-based registration is desirable because its results are objective and quantitative analysis is possible.

The registration method applies the concept of mutual information (MI) to measure the statistical dependence between the image intensities of corresponding voxels in both images. Because no assumptions are made regarding the nature of this dependence and no limiting constraints are imposed on the modalities involved, MI is a general and powerful criterion, which can be applied on a large variety of applications. Retrospective Registration Evaluation Project (RREP) has done an extensive evaluation on the performance of various registration methods, the results demonstrated the superior performance of MI for automatic multimodal registration [111]. However, MI ignores the

spatial information contained in the images such as edges and corners that might be useful in the image registration. Since the joint intensity histogram by itself is insufficient, our focus is to increase registration robustness and accuracy by taking spatial information into consideration. Here, we introduce the Adaptive Mutual Information (AMI) measure which incorporates the gradient spatial information. The decision to choose gradient information is motivated by the fact that the image locations with a strong gradient have high information value, which could be useful for the image registration. Salient pixels in the regions with high gradient value will contribute more in the estimation of mutual information of image pairs being registered. Experimental results showed that our proposed method improves registration accuracy and it is more robust to noise images which have large deviation from the reference image.

This chapter will present a review of the MI registration criterion and its application for multimodal medical image registration. We start with a discussion of the theory and implementation of the MI registration algorithm as originally presented by Collignon et al. [3] in Section 4.2. The proposed AMI approach is discussed in Section 4.3. Validation of the AMI registration criterion is discussed in Section 4.4 and the registration performance of AMI is compared with the MI algorithm. Section 4.4.1 examines the registration accuracy of the proposed method. Section 4.4.2 reviews the robustness of the algorithm with respect to noise and we conclude the chapter in Section 4.5.

4.2 Mutual information registration algorithm

4.2.1 Mutual information theory

The basic idea of mutual information (MI) [3, 6, 63] comes from information theory which measures the statistical dependence between two random variables or the amount of information that one random variable contains about the other. For discrete random variables *X* and *Y* with their respective marginal probability distributions $P_X(x)$, $P_Y(y)$ and joint probability distribution $P_{XY}(x, y)$, MI is defined as:

$$MI(X,Y) = \sum_{x,y} P_{XY}(x,y)\, log \frac{P_{XY}(x,y)}{P_X(x)P_Y(y)} \tag{24}$$

MI is also related to the joint entropy information theory by the following equation:

$$MI(X,Y) = H(X) + H(Y) - H(X,Y) \tag{25}$$

$$= H(X) - H(X|Y) \tag{26}$$

$$= H(Y) - H(Y|X) \tag{27}$$

If *X* and *Y* are two images that are geometrically related by the registration transformation, the terms *H(X)* and *H(Y)* are denoted as the entropy of the reference image and floating image respectively, while *H(X,Y)* is the joint entropy of both images. The MI similarity measure suggests that the images are geometrically aligned when *MI(X,Y)* of the corresponding images is maximal. If both marginal entropy *H(X)* and *H(Y)* are to be independent, which is the case there is no overlap area between two images, *MI(X,Y) = 0*. If either *H(X)* or *H(Y)* is completely contained in the other, both images *X*

and *Y* are one-to-one related, *MI(X,Y) = H(X) =H(Y)*. However, if both images only partially overlap, the MI measure becomes clear in equation (25), which can be interpreted that maximizing MI will tend to find as much as possible of the information that exists in the both images so that at the same time they explain each other well. Additional properties of MI are summarized in Table 4.1 (see [112] for their proof).

Non-negativity:	$I(X,Y) \geq 0$
Independence:	$I(X,Y) = 0 \Leftrightarrow P_{XY}(x,y) = P_X(x).P_Y(y)$
Symmetry:	$I(X,Y) = I(Y,X)$
Self-information:	$I(X,X) = H(X)$
Boundedness:	$I(X,Y) \leq \min(H(X), H(Y))$
	$\leq (H(X), H(Y))/2$
	$\leq \max(H(X), H(Y))$
	$\leq H(X,Y)$
	$\leq H(X) + H(Y)$
Data processing:	$I(X,Y) \geq I(X,T(Y))$

Table 4.1: Some properties of mutual information.

4.2.2 Image registration using mutual information

Unlike point set registration, the MI registration criterion does not require any preprocessing or segmentation of the images. MI based registration rely on the relative occurrence of intensity values in each of the images separately and their co-occurrence in both images combined. Although multimodal images of the same scene may have different intensity representation, the same voxels of the same object are not totally independent, but are statistically related. As such the applicability of MI is widely applied

in multimodality registration problems [3, 65, 66, 113]. While originally MI was introduced for multimodality image registration, MI has also been used successfully for monomodality image registration, for instance, serial MR images [114], fMRI time series images [115], or mammogram images [116].

In the following section we will refer the two image data that are to be registered as the reference image, X and floating image, Y. Let x denote the image intensity in the reference image and y the intensity in the floating image. Intensities x and y are related through the geometric transformation T_α defined by the registration parameter α.

The MI algorithm is summarized below:

1. The reference and the floating image intensities are first linearly rescaled to the range $[0, N_X - 1]$ and $[0, N_Y - 1]$, with N_X and N_Y as the number of intensities in the images. Typically, we use $N_X = N_Y = 256$.
2. Allocate an N_X x N_Y array for the total number of bins in the joint histogram.
3. Compute the joint intensity histogram *JHIS(X,Y)* of the overlap part $X \cap Y$ in the images by finding the intensity pairs. For every pixel $i \in X \cap Y$, if the intensity value in X is $X(i) = x$, and the corresponding value in Y is $Y(i) = y$, then $JHIS(x,y) = JHIS(x,y) + 1$.
4. Calculate the normalized joint intensity histogram.

$$PDF(x,y) = \frac{JHIS(x,y)}{\sum_{x,y} JHIS(x,y)} \tag{28}$$

5. Calculate the joint image intensity distributions based on the normalized joint intensity histogram.

$$P_{XY}(x,y) = \sum_{x}\sum_{y} PDF(x,y) \tag{29}$$

6. Calculate the marginal intensity distributions by the sums of the rows and the columns of the normalized joint histogram.

$$p_X(x) = \sum_{y} PDF(x,y) \tag{30}$$

$$p_Y(y) = \sum_{x} PDF(x,y) \tag{31}$$

7. The MI registration criterion is then evaluated by equation (24).
8. Repeat step 1 – 7 to search the transformation parameters that maximize the mutual information. The optimal registration parameter α^* is found from

$$\alpha^* = \arg max_{\alpha}\ I(X,Y) \tag{32}$$

4.3 The proposed adaptive mutual information (AMI)

4.3.1 Image gradient information

The gradient information is a measure of the image intensities changing rate between neighboring voxels and it is commonly used for edge detection process. We assumed that the image locations with a strong gradient contain high information value, which could be useful for the image registration. Furthermore, the gradient intensity utilizes all the information which is in a medical image and as such, is suitable for the registration problem. The gradient function, $\nabla\bar{X}$ of a 2D image is defined as the gradient vector, *Gx*, *Gy* in *x* and *y* directions:

$$\nabla\bar{X} = \begin{bmatrix} G_x \\ G_y \end{bmatrix} = \begin{bmatrix} \frac{\delta\bar{X}}{\delta x} \\ \frac{\delta\bar{X}}{\delta y} \end{bmatrix} \tag{33}$$

The corresponding voxels in the reference and the floating image are denoted by $\bar{X}$ and $\bar{Y}$, respectively. There are a number of different ways to calculate gradient information from images. In the work presented here, we used a simple approach where the gradient magnitude is calculated by applying the *x* and *y* components of the two-dimensional numerical gradient according to the following expressions:

$$|\nabla\bar{X}| = \sqrt{\nabla x^2 + \nabla y^2} \tag{34}$$

4.3.2 Normalized mutual information based on significance of pixels

In image registration, the significance of pixels in a medical image is not the same. Since high gradient magnitude is preferred, the significance of a pixel S_i is determined by incorporating the scaled gradient magnitude as follows:

$$S_i = \frac{(G_i + I_i)}{(G_{max} + I_{max})} \tag{35}$$

G_i is the gradient magnitude values derived from the equation (34) and I_i is the original intensity values of the image. The result of S_i is the saturation with the maximum of one and the minimum of zero because the addition of the terms requires normalization. The result image is then linearly rescaled to the range $[0, N_X - 1]$ and $[0, N_Y - 1]$. Typically, we use $N_X = N_Y = 256$. The intensity transitions that are depicted in the image are emphasized by adding the gradient term to the original image, as shown in the Figure 4.1.

Because of the statistical dependency, MI is sensitive to the amount of overlap between both images. Normalized mutual information (NMI) measures were introduced by Studholme et al. [67] to overcome this problem. This is shown in the following equation:

$$NMI(X,Y) = \big(H(X) + H(Y)\big)/H(X,Y) \tag{36}$$

We will therefore use NMI to combine the intensity and gradient information into a single cost function. Finally, the complete MI cost function is expressed below:

$$AMI\big(S_r, S_f\big) = \Big(H(S_r) + H\big(S_f\big)\Big)/H\big(S_r, S_f\big) \tag{37}$$

where S_r and S_f are the significance of pixels of both the reference and floating image derived from the equation (35). By applying mutual information to the gradient magnitude images themselves would seem rational to incorporating spatial information. Therefore we also experiment it and discuss the result in Section 4.4.

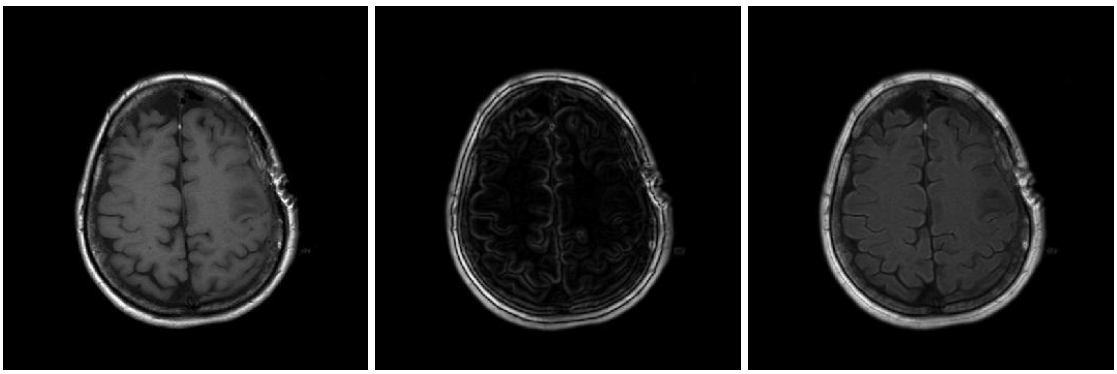

(a) (b) (c)

Figure 4.1: Example of the intensity changes and contribution of gradient information to the resultant image. A transaxial slice of a MR image is shown in (a) and the corresponding gradient image calculated according to (48) is presented in (b). The resultant image (c) is found by summing over intensity value of original image and gradient image based on the formula (35) stated above.

4.4 Comparative studies between MI and AMI

The performance of the registration criterion was evaluated for rigid registration of the brain images. In this work, the main idea behind the validation method was to compare the similarity measures of different transformation parameter α relative to their true position. This was done by first applying a known transformation to an image and then transforms the image within the search space. We will plot the similarity measures graph to compare their global maxima and the smoothness of the search space. First, experiments with known image transformation show the quality of the registration method. Further tests reveal the robustness of the method with respect to Gaussian noise. For better understanding and visualization for the results, we analyze separately rotation and translation.

The similarity measure was implemented in MATLAB [108] and two different datasets are used in the experiments, which are acquired from the Whole Brain Atlas website [117]. Dataset A contains high resolution MR and CT images, while dataset B contains MR images of different slice. CT/MR and MR/MR image pairs with known transformation parameter are registered in order to validate the registration accuracy. Registration of MR/MR images is a common monomodality scenario for intensity-based registration. The same tissue characteristics are imaged and the structure in the images is similar. Registration of CT/MR images is a more difficult problem because CT image depict different anatomical details compare to MR image. However the corresponding structures and gradients are appearing in both images. The reference and floating image pairs are presented in Figure 4.2. In all experiments, the default joint histogram size used in the algorithm is 256 x 256.

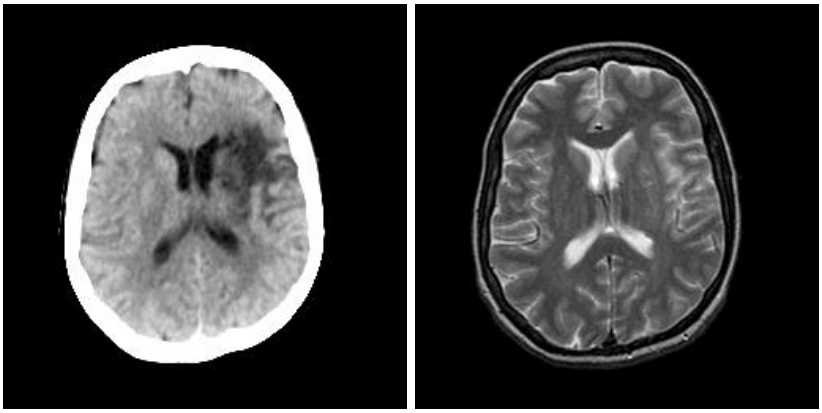

(a) CT image (b) MR image

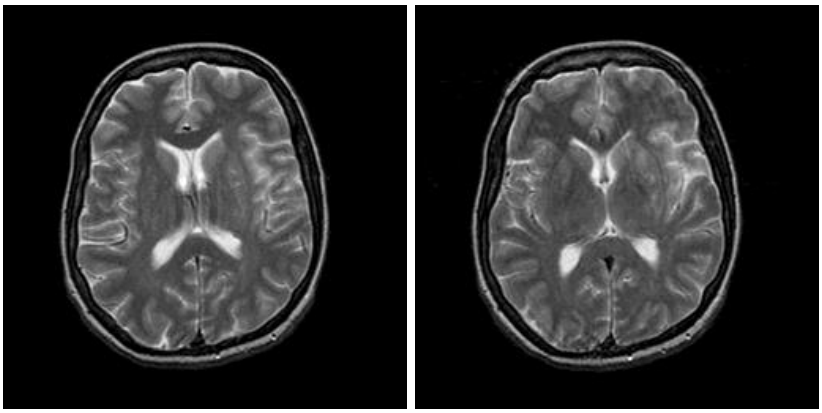

(c) MR image 14th slice (d) MR image 15th slice

Figure 4.2: 2D image slices used in our experiments. The top row is the dataset A: CT/MR image pair; the bottom row shows the dataset B: MR/MR image pair.

4.4.1 Registration accuracy estimation

In this experiment, the transformations were performed with respect to the rotation range of [−20°, 20°] around its center point, and translation range of [−20, 20] (pixels) on x-axis to search for the optimum value of the registration function. Since the datasets were originally aligned, the ground-truth transformation parameters are known. Any shift or rotation away from their original positions will decrease the similarity measure of image pair. The registration result of the normalized mutual information (NMI), gradient-based

mutual information (GMI) using the gradient image and the proposed adaptive mutual information (AMI) were compared in the experiments. To evaluate the performance of the methods, the plots of different similarity measures values against the changes in translation in x-axis (*Tx*) as well as the changes in rotation about z-axis (*Rz*) are shown.

The results of the MR/MR monomodality registration are presented in Figure 4.3. The left figure shows the curve functions for rotation around its center point. Clearly, AMI yield the highest similarity value and the correct registration solution was found. It also can be seen that NMI function has a local minimum at the position of correct alignment, where the highest similarity value lies on the -1° rotation. There is only a single strong optimum for AMI and GMI, which coincides with the correct registration result. The AMI measures produced slightly better result compared to NMI and GMI measures, although the differences were not significant. In the right figure, the curve functions for translation in the horizontal direction are shown. All three methods found the correct registration solution and showed a single high peak value.

Figure 4.4 shows the results of the CT/MR registration experiment. The left figure is the curve functions for rotation around its center. Again, NMI function doesn't give the correct registration result and it has a local minimum at the position of correct alignment. The highest similarity value lies on the 1° rotation. To further pinpoint the performance of AMI, the rotation range is extended to [-60°, 60°] and showed in the bottom row of Figure 4.4. The results demonstrated that AMI produces a sharper peak and decreased faster than other methods as the image rotated away from their original positions. In the right figure, the curve functions for translation in the horizontal direction are shown. The

results are similar except NMI has slight misregistration which was circled out in the figure.

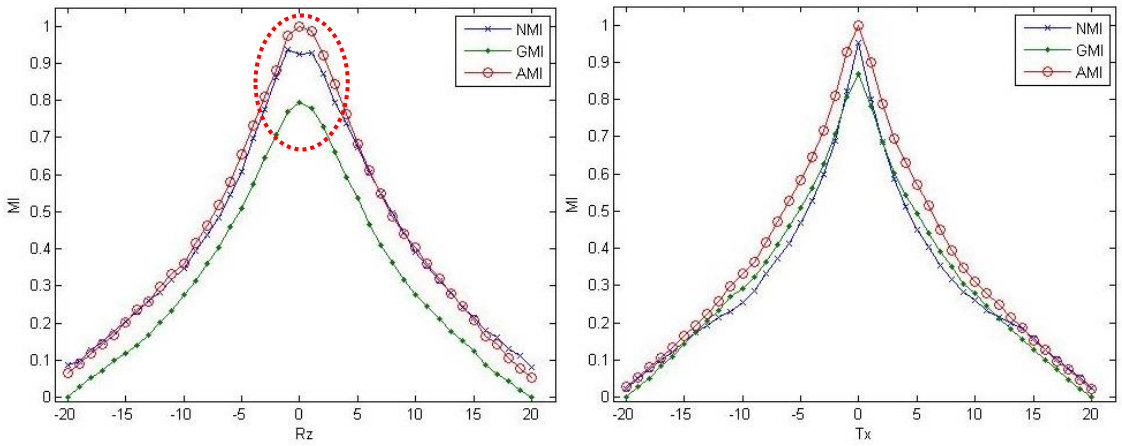

(a) (b)

Figure 4.3: Similarity measures result for MR/MR image registration. From left to right: (a) rotation around its center point, (b) translation in the horizontal direction.

4.4.2 Robustness to noise

Subsequently, we carry out noise experiments with the CT/MR dataset. In this section, the floating image was added the Gaussian white noise with the mean set to zero, and variances are respectively 0.01, 0.02, 0.03, 0.04, and 0.05. The Gaussian noise affects independently all pixels of the images and thus highly corrupts the information content. Under these five conditions, we are looking for a smooth function with a sharp peak. In Figure 4.5, we observed that NMI doesn't produce a global maxima and it failed to preserves the curve function after the noise variance of 0.02. On the other hand, AMI function preserves the curve function from distortion at each noise level within the rotation range of [-60°, 60°]. Although GMI and AMI also have a local minimum at the position of correct alignment due to the noise corruption, they produce the result more closely to the correct registration solution. Table 4.2 shows the rotation error for all five

datasets and emphasize the lowest value in bold. The rotation error of both GMI and CMI measures are below 3°.

Noise variance	NMI	GMI	AMI
0.01	-3°	**1**°	**1**°
0.02	-8°	2°	**1**°
0.03	-10°	**2**°	3°
0.04	-25°	**2**°	**2**°
0.05	-31°	**2**°	3°

Table 4.2: The rotation error for all the five dataset based on NMI, GMI and CMI methods. The values highlighted in bold emphasize the lowest error.

4.5 Discussion and conclusion

MI is an effective similarity measure for multimodal image registration. As applied here the technique is intensity-based, rather than feature-based. Such an approach avoids the task of identifying corresponding features information in two different modalities, which is difficult to automate for a wide range of clinical data. Despite the general promising results, there are situations which can challenge the applicability of MI and result in misregistration. In this chapter, we have presented the adaptation of mutual information measure which incorporates the spatial information based on significance of pixels. We assumed that the image locations with a strong gradient contain high information value, which could be useful for the image registration. The proposed method uses a simple way to enrich the image description by integrating the gradient information. We experimented with various modalities of brain images and showed that our method is more reliable than the existing mutual information method. From the result, we can see that AMI does not only make the similarity measure sharper, but also decrease the interpolation induced

local minima. It also demonstrated that AMI is more robust to noise than existing MI method. In cases in which MI performs well, the registration result of AMI is similar to MI and the global maxima do not alter significantly. Another similarity measure was included in the experiment by simply applying mutual information to gradient images. The idea seems logical in incorporating spatial information and the results showed that GMI generates the correct registration solution as AMI. However, because a lot of intensity information is discarded, the GMI value is much lower compare to AMI.

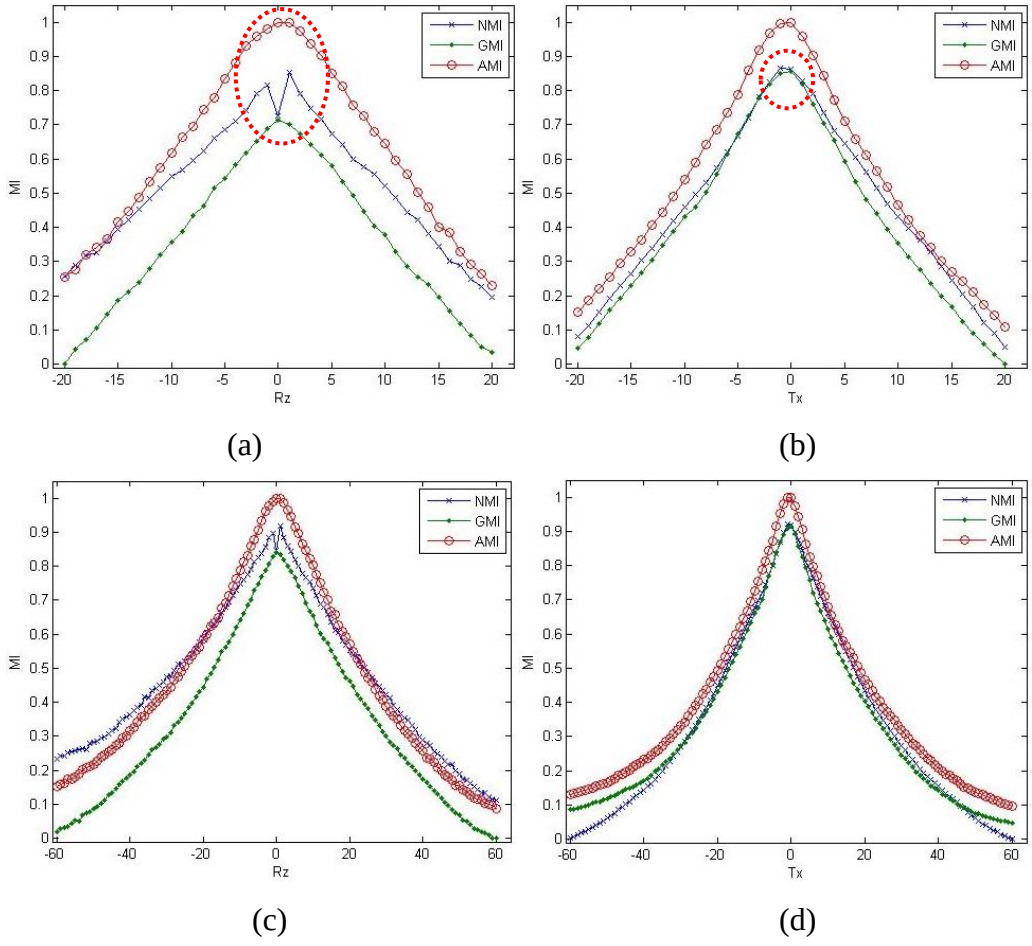

Figure 4.4: Similarity measures result for CT/MR image registration. The top row shows the rotation range of [-20°, 20°], and translation range of [-20, 20] on x-axis. The bottom row shows the rotation range of [-60°, 60°], and translation range of [-60, 60] on x-axis. From left to right: (a) rotation around its center point, (b) translation in the horizontal direction.

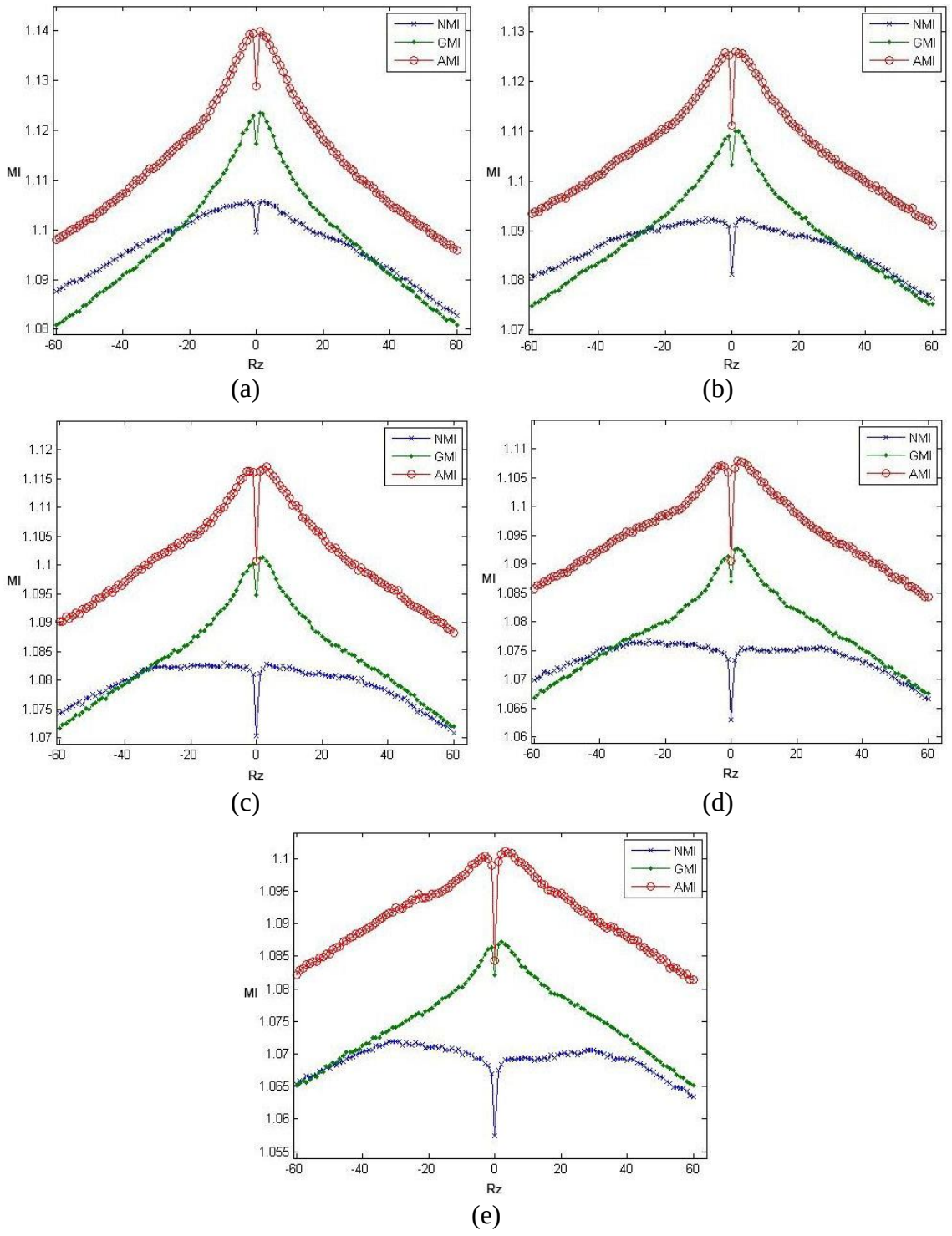

Figure 4.5: CT Similarity measures result for CT/MR noise image registration. The Gaussian white noise was added to the floating image, with the mean is zero, and variances are respectively (a) 0.01, (b) 0.02, (c) 0.03, (d) 0.04, and (e) 0.05.

Chapter 5

Multi-Features for Mutual Information based Medical Image Registration

5.1 Introduction

Recently mutual information (MI) has grown to be accepted as a popular similarity measure and widely being recognized in the field of medical image registration. However, a known disadvantage of MI-based image registration is the lack of concern on any spatial information and involves only the pixel intensities as an input feature. To avoid this additional spatial information is required. It has been shown in the previous chapter that incorporating gradient information into MI algorithm can overcome some of the shortcomings of the conventional technique. The method presented in this chapter is an extension of previous work aimed towards registration of multiple spatial features. From the vast amount of feature choices that describe the structural information of images, we would like to incorporate the spatial feature that: (a) classify information-rich areas; (b) return values that are a smooth decreasing function of misregistration. Along this direction, we propose multi-features mutual information (MF-MI) measure to simultaneously use all information obtained from multiple features. The method is thoroughly investigated and its accuracy and robustness are evaluated on both simulated and experimental data. Through quantitative evaluations, the MF-MI measure is proven to handle a wide variety of registration difficulties. Using multiple spatial features, the proposed algorithm is less sensitive to the effect of noise and some inherent variations, giving more accurate registration.

The organization of this chapter is as follows. Section 5.2 explains about the registration framework and implementation. The spatial features used for the image registration are discussed in Section 5.3. Evaluation is performed on the medical images and we illustrate the clinical relevance of the proposed method for image registration involving CT, MR, MR-PD, and SPECT images of the head, see sections 5.4. The conclusion is drawn in Section 5.5.

5.2 Multi-features enhanced mutual information algorithm (MF-MI)

In a survey of MI-based image registration [53], Pluim et al. provided a comprehensive review of the MI algorithm and mentioned the challenges to "correct" the assumption of Shannon entropy that the intensity values of neighboring pixels are uncorrelated. Multi-channels or multi-dimensions mutual information are one of the important trends in image registration to overcome the shortcoming of MI technique. The idea behind this is to include additional channels or dimensions in joint intensity histogram that describe the spatial information which in turn helps to increase the robustness and accuracy of the registration algorithm. However, as dimensionality increases, the power of histogram statistics decreases and more samples are needed to fill the joint histogram up to a sufficient level, so that MI can be reliably estimated. In this chapter, we propose an extension of the standard single feature MI similarity measure to a multi-features MI measure to solve the problem of joint probability distribution estimation in a multi-dimensional feature space. The proposed measure incorporates the commonly used image intensity feature with additional spatial features, such as image gradients or other texture

parameters. According to their complementary properties, additional spatial features are assimilated in MF-MI similarity measure:

$$MFMI(R,F) = \sum_{i=1}^{N} \lambda_i \frac{\left(H(R_i) + H(F_i) \right)}{H(R_i, F_i)}, \quad 0 \leq \lambda_i \leq 1 \tag{38}$$

where the λ value ranges from the value one to zero. This property is very important for the weighting function because the output of equation presents a fraction whose value extends from zero to one.

The MF-MI similarity measure is defined as the aggregate measure of MI from a set of spatial distribution extracted from the images. The correct image registration is achieved by the maximization of the MF-MI value. Being a linear combination, all of the properties (as listed in Table 4.1) held by the MI automatically hold for the MF-MI, such as non-negativity, independence, symmetry, etc. Given the reference image *R* and floating image *F*, $H(R_i)$, $H(F_i)$, and $H(R_i, F_i)$ are the marginal entropies derived from all image features [$i=1, \ldots, i=N$]. The weighting coefficients λ_i specify the relative contribution of each image feature to the MF-MI. When a single feature is used with $\lambda_1 = 1$, MF-MI is equivalent to the commonly used NMI similarity measure. When multiple features ($i > 1$) are used, the weights λ_i can be adjusted for specific dataset to resolve the potential ambiguities. By valuing the weighting coefficient, we can differentiate the importance of the spatial information from the normal intensity information. The best weights (λ values) for each image feature were obtained by experimental method. The procedure is as follows:

1. Calculate NMI of each image feature according to equation (24). The experiments were performed with respect to the rotation range of [−90°, 90°] around its center point, to search for the optimum value of the registration function.
2. Initialize $c_i = 1$ and $d_i = N^2+N$.
3. Calculate the entropy of each image feature according to the equation (1). If entropy (i) > entropy ($i+1$), then $c_i = c_i + 1$, else $c_{i+1} = c_{i+1} + 1$.
4. If $i < N$, then increment i and go to step 3.
5. The weights λ_i of each image feature is found from.

$$\lambda_i = \frac{c_i}{d_i} \tag{39}$$

5.3 Spatial features

Now that the registration framework for multi-features mutual information has been defined, spatial features need to be chosen. From the vast amount of choices, we are looking for the features that describe the spatial information of images and supply supplementary features to the algorithm, which may improve the registration quality. The term spatial information is the parameters that describe and provide important details about the image such as image gradient, edges, corners, texture, etc. To analyze the spatial features, we are trying to explore standard statistical measures from texture parameters. The texture parameter refers to the characterization of the spatial variation in pixel intensities, which is useful in retrieving the information available from medical images. Because texture has so many different varieties, we have selected gradient magnitude and standard deviation filter for further investigation. However the standard

deviation image feature was not included in the chapter because MF-MI with standard deviation image feature produces poorer registration result in all experiments. Besides, it provides similar image intensity profile with adaptive image gradient. Based on the objective of MF-MI, the image feature should describe the spatial information of images and supply supplementary features to the algorithm, which may improve the registration quality. Therefore only image gradient will be discussed in the following sections.

5.3.1 Adaptive image gradient

Gradient magnitude is a measure of the image intensities changing rate between neighboring pixels. It is normally used to detect the object boundaries where pixels change their intensity suddenly. By deriving gradient magnitude map, pixels at object boundaries would give large values, which may only occupy a small part of the whole image volume. On the other hand, the background regions and anatomical structures would give small and almost constant values. Thus, we define a new image feature, namely adaptive image gradient (AIG), by incorporating the spatial information about the distance of a pixel to the object boundary into the original image. In developing AIG feature, we made the following modifications to the original gradient magnitude map to vary it smoothly and gradually from object boundaries towards similar image regions.

1. We begin by defining a gradient operator, ∇G in an image. In this work, we used the *x* and *y* components of the two-dimensional numerical gradient to calculate the gradient magnitude according to equation (34).
2. Then, we derived a logical gradient map of the image by performing element comparison to the gradient magnitude, where each element of the logical gradient map is:

- Logical 1 (true) if the corresponding element of gradient magnitude is greater than zero.
- Logical 0 (false) if the corresponding element of gradient magnitude equals zero.

3. Based on the binary information in logical gradient map, we perform distance transform by calculating the Euclidean distance between each pixel that is set to zero (0) and the nearest nonzero pixel. In 2D image, the Euclidean distance between (x_1, y_1) and (x_2, y_2) is

$$Euclidean\ distance = \sqrt{(x_1 - x_2)^2 + (y_1 - y_2)^2} \tag{40}$$

4. The result is then linearly rescaled to the range [0, 1]. The AIG feature is determined by multiplying the distance transform result to the gradient magnitude map, as shown in Figure 5.1(b).

Following this formulation, the AIG value increases smoothly and gradually as the pixel position moves from boundaries towards interiors of anatomical structures. With this property, the AIG feature can provide detailed spatial information, which is about the distance of a pixel to a certain object's boundary, and therefore is superior to the traditional gradient magnitude map.

5.3.2 Intensity profile comparison

As a comparative illustration, we individually computed the intensity value profiles of the original image and AIG feature map of a clinical image. The original image is shown in Figure 5.1(a), while Figures 5.1(b) present the corresponding slice from the AIG maps. For a detailed explanation, Figures 5.1(c) and (d) respectively present the value profiles

of the same line (marked as dashed lines) shown in Figures 5.1(a) and (b). Note that the values from individual images are re-scaled to [0, 1] for a fair comparison. As suggested by the figures, feature values in Figure 5.1(c) are very sparse, where the majority value is small and constant. On the contrary in Figure 5.1(d), the value variation from boundaries towards homogenous regions provides more information details. In addition, much more structural information can also be found in the AIG map. For instance, regions close to boundaries in Figure 5.1(b) suggest much more information than those in Figure 5.1(a).

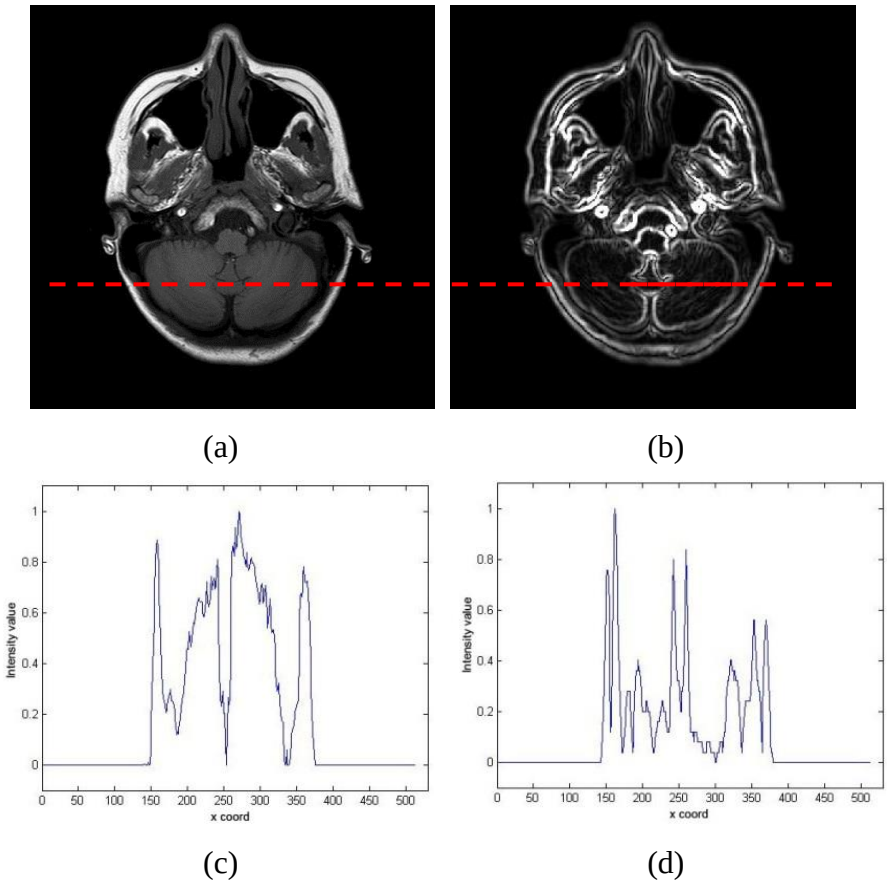

Figure 5.1: (a) and (b) are slices respectively selected from a clinical MR-T1 image volume and its corresponding AIG maps. (c) and (d) are value profiles of lines in (a) – (b), which are marked as dashed lines.

5.4 Experimental Results

In this section, we conduct several experiments with MATLAB software [108] to evaluate the performance of different spatial features that we have selected. An ideal registration function should present a global maximum close to the correct transformation parameters. Moreover, the registration function should be smooth and convex with respect to different transformation parameters and the number of local maxima of the registration function should be as small as possible. In our experiment, the NMI method was used as the baseline for comparison of results. Subsequently, we will highlight some typical registration functions for different registration problems. In Section 5.4.2, we shall evaluate the robustness of the spatial features by adding Gaussian white noise to the floating image. In Section 5.4.3, the robustness of the spatial features to different image overlaps was assessed.

5.4.1 Registration Quality Estimation

A good registration algorithm should be able to recover the accurate transformation between two images. Accordingly, the registration quality of the NMI and MF-MI similarity measure is evaluated based on a wide variety of registration problems: multimodality registration and monomodality registration of different time series images. The medical images involved were obtained from the Whole Brain Atlas (WBA) database [117]. Only 2D images from the central slice of the axial view are selected for registration due to the large number of registration tasks involved. For visual inspection, the brain images used in the experiment are shown in Figure 5.2 and Figure 5.3. A summary of each data set is given below.

a) Data-set 1: CT, MR-T2, MR-PD, SPECT, 42 year-old male, Metastatic Bronchogenic Carcinoma, as shown in Figure 5.2.

b) Data-set 2: CT/CT, 86 year-old male, Acute Stroke with fluent aphasia, as shown in Figure 5.3a.

c) Data-set 3: MR-T2/MR-T2, Multiple Sclerosis patient, as shown in Figure 5.3b.

d) Data-set 4: SPECT/SPECT, 36 year-old male, AIDS Dementia, as shown in Figure 5.3c.

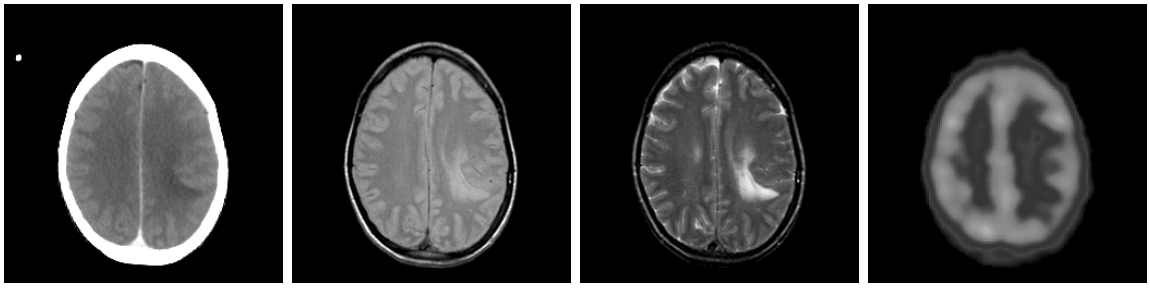

(a) (b) (c) (d)

Figure 5.2: A slice of image series from one individual used in the multimodality registration experiment. (a) CT brain image. (b) MR-PD brain image. (c) MR-T2 brain image. (d) SPECT-Tc brain image.

The experiments were performed with respect to the rotation range of [−90°, 90°] around its center point, and translation range of [−90, 90] (pixels) on x-axis to search for the optimum value of the registration function. Since the data sets were originally aligned, the ground-truth transformation parameters are known. Any shift or rotation away from their original positions will decrease the similarity measure of the image pair. The registration results for all four test data sets are summarized in Table 5.1 and Table 5.2. Table 5.1 shows the comparative performances for rotation around its center point. It can be observed that the MF-MI registration algorithm successfully register all pairs of images, compared to the NMI registration algorithm. A misalignment occurred in MR-

PD/SPECT registration task, which the optimum parameter being slightly away from the correct global maximum which is 0°. This might be due to the fewer similarities between the image contents of MR-PD and SPECT. In Table 5.2, most of the cost functions point to the correct global solution.

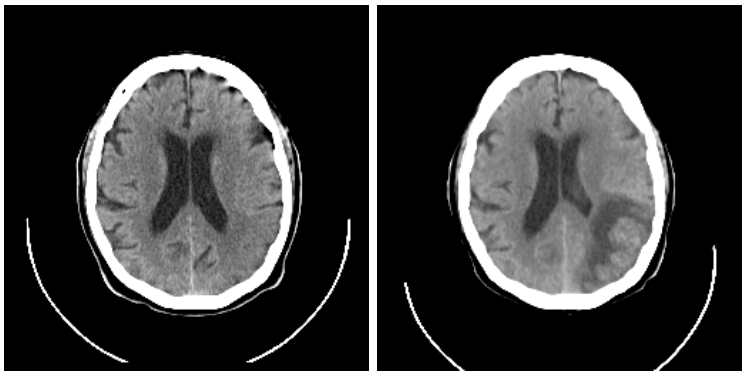

(a)

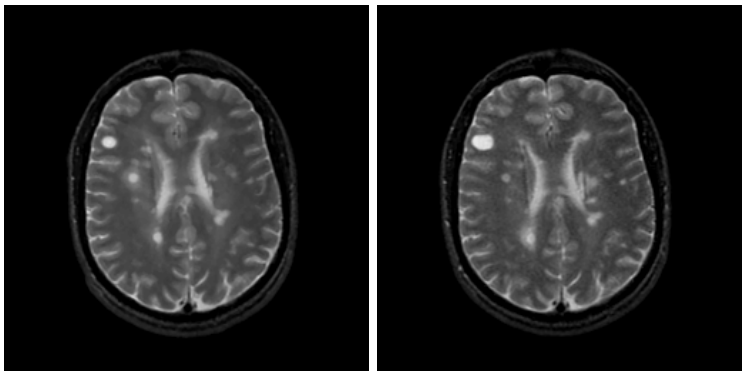

(b)

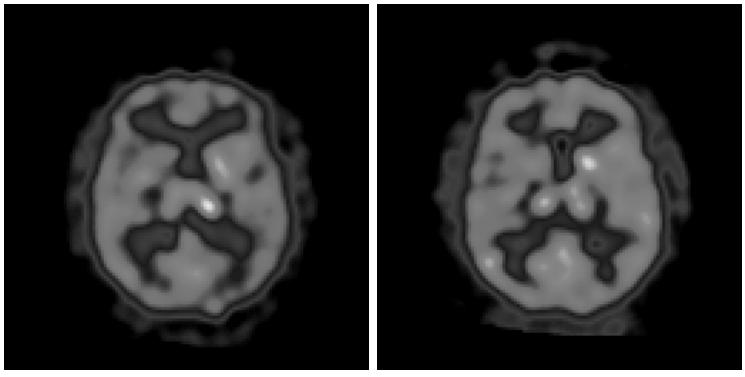

(c)

Figure 5.3: A slice of image series from one individual used in the monomodality registration experiment. (a) CT brain image. (b) MR-T2 brain image. (c) SPECT brain image.

As summarized in Table 5.1 and Table 5.2, the MF-MI results were almost similar to the NMI measure in all registration cases except MR-PD/ SPECT. Although we cannot conclude that MF-MI is more efficient in searching for global maximum at all cases, their accuracy results are the same or closer to the ground truth. When the spatial information was used, the registration functions are improved especially for poor image correspondence or lower resolution images like SPECT images.

Data sets	*Accuracy*	
	NMI	MF-MI
Multimodality		
CT/MR-T2	0	0
MR-T2/PD	0	0
MR-PD/SPECT	2	0
Monomodality		
CT/CT	0	0
MR-T2/T2	0	0
SPECT/SPECT	0	0

Table 5.1: Comparative performances between NMI and MF-MI for the experiment of rotation around its center point. The "Accuracy" column is the rotation error in degree.

Data sets	*Accuracy*	
	NMI	MF-MI
Multimodality		
CT/MR-T2	0	0
MR-T2/PD	0	0
MR-PD/SPECT	0	0
Monomodality		
CT/CT	0	0
MR-T2/T2	0	0
SPECT/SPECT	0	0

Table 5.2: Comparative performances between NMI and MF-MI for the experiment of translation in x-axis. The "Accuracy" column is the translation error in pixel.

5.4.2 Robustness to Noise

Medical images are prone to be corrupted by noise due to different conditions that can occur during the acquisition procedure. The goal of this experiment is to discuss the effect of noise to the algorithm's performance and the advantage of spatial information in terms of robustness to noise. We carried out the experiment with CT/MR-T2 image pairs from data-set 1 and added various levels of Gaussian white noise with mean (m = 0) and variance (ν = 0.0001, 0.0003, 0.002, 0.007, and 0.01) to the floating image. For these images, the Gaussian white noise with different variances will produce the noise level around 1%, 2%, 5%, 8%, and 10%. We are not interested to go further above 10% noise level because the Gaussian white noise highly contaminates the information content in medical images. Under these five conditions, we analyze the impact of noise on the global maximum searching and the smoothness of the function.

The registration results for various noise levels are summarized in Table 5.3. The values in the column labeled with "Accuracy" are the rotation error of the registration function. The global maxima of the function achieved using MF-MI is closer to the optimum 0° and the results remained largely consistent as noise levels increased. However this is not the case with NMI method, where the global maximum is greatly influenced by the noise artifact and the accuracy decrease significantly as noise levels increased, where there is a noticeable increase in the rotation error for ν = 0.01. This registration inaccuracy can be caused by the significant loss of structural characteristics when high level of noise is added. As the noise level increases, the correlation between images is weakened and the convergence ranges are broadened. This reveals that MF-MI with spatial information is much less sensitive to the increase of noise compared to the

standard single feature NMI measure. Compared with the NMI, MF-MI has more information to represent the whole structure features of medical image and presents good stability even in a noisy environment.

Noise level (v)	*Accuracy*	
	NMI	MF-MI
0.0001 ≈ 1%	-1	0
0.0003 ≈ 2%	-1	0
0.002 ≈ 5%	-1	0
0.007 ≈ 8%	-1	0
0.01 ≈ 10%	-2	0

Table 5.3: Comparative performances in terms of different weighting coefficients for different noise level. The "Accuracy" column is the rotation error in degree.

5.4.3 Invariance to image overlaps

In this section an extended investigation was made to examine the behavior of measures to the misalignment of an image when it is presented with varying image overlaps. In order to look at the effect it has on registration measures, the CT/MR image set was truncated in-plane to produce image pairs with different overlapped regions. We used a simple model where there are two parameters, one controlling the changes in rotational alignment θ, around its center point and another controlling the field of view (FOV) to vary the overlaps. For simplicity, the reference image has a complete extent, while the floating image has a limited extent determined by the parameter FOV. Using this simple model, the behavior of measures can be evaluated directly for different rotational misalignment and field of view. The registration results for each measure and each FOV parameters are shown in Table 5.4. Both measures provide robust recovery of alignment until the FOV is reduced to 70%. MF-MI with spatial information relatively provides

good recovery of alignment for all but misalignments occurred at the FOV of 60% and below. To further expound the experiment result, the registration functions for rotation degree between -30° and 30° and field of view parameter FOV between 90% and 50% are shown in Figure 5.4. It can be seen that the response of all measures are affected considerably by the variation in field of view. As the field of view increases, the local maxima of the function increases and the smoothness of the function is lost. However MF-MI measure provides a better response with a much sharper peak at the correct alignment.

Field of View (FOV)	*Accuracy*	
	NMI	MF-MI
90%	0	0
80%	0	0
70%	-1	0
60%	-1	1
50%	1	1

Table 5.4: Comparative performances in terms of different weighting coefficients for different FOV level. The "Accuracy" column is the rotation error in degree.

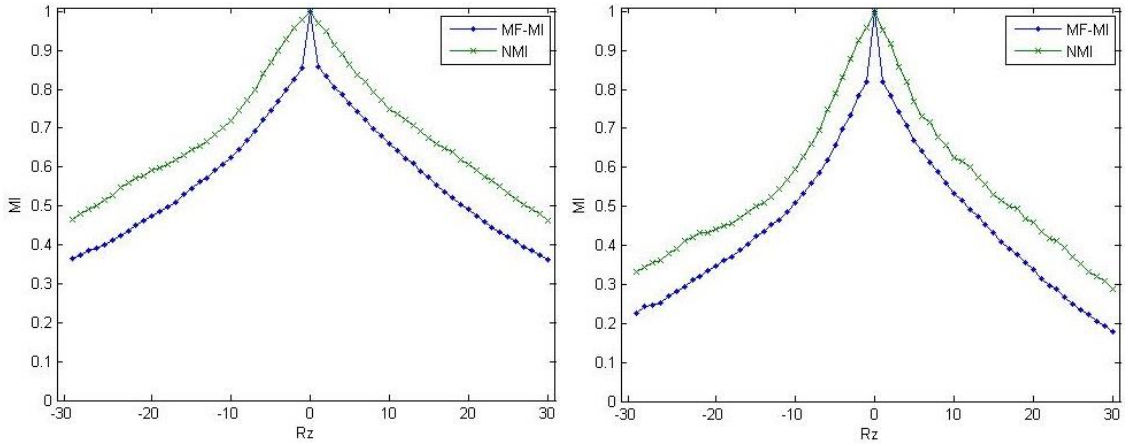

(a)

(b)

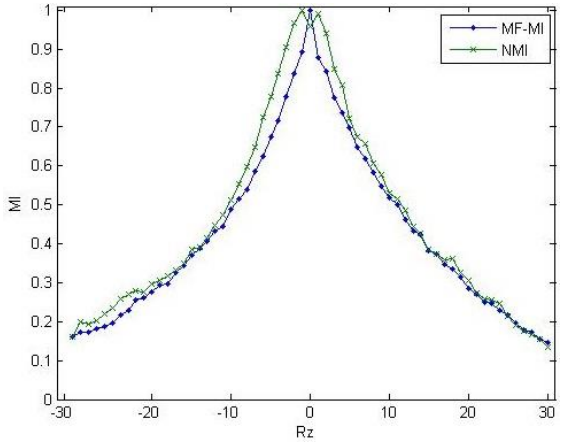

(c)

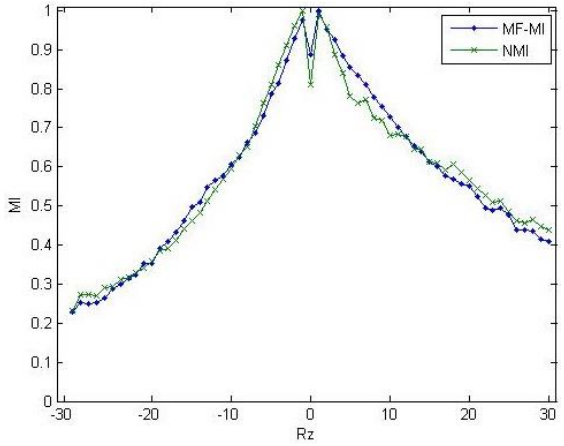

(d)

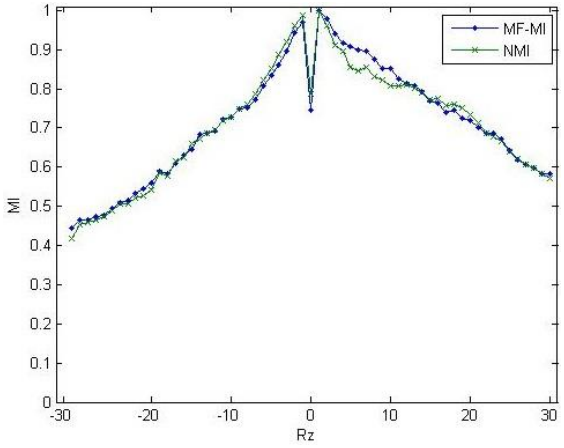

(e)

Figure 5.4: The registration function (CT/MR-T2) versus relative rotation for different field of view. From left to right: (a) 90%. (b) 80%. (c) 70%. (d) 60%. (e) 50%.

5.5 Discussion and Conclusion

Although MI has been successfully applied to medical image registration, its reliability depends on the statistical stability of samples. Hence MI function is easily influenced by the intensity interpolation and noise artifacts, which may cause many local maxima that lead to the failure of registration. In addition, MI presents a poor performance for registration of images with low resolution or with small overlapped area of images. To overcome these weaknesses, we have introduced MF-MI for robust registration of monomodality and multimodality brain images. One major contribution of MF-MI method is the incorporation of multiple image features into MI method, while allowing a flexible choice of the spatial information through weighting coefficients. The constant weighting scheme λ was used to weigh the significance of the spatial information and it can be adjusted for specific dataset or fine-tuned through experiment samples. The performance of this weighting scheme highly depends on the parameterization of λ for different registration tasks. Furthermore, the proposed MF-MI measure can be computed for a number of additional features, as long as these features provide the same output image resolution.

Through quantitative evaluations, the MF-MI has been shown to produce an improvement of the registration compared with standard MI using intensity information alone. Using multiple image features, the proposed method has reduced the effect of noise and some inherent variations, making the registration result more accurate. In cases in which MI performs well, the registration result of MF-MI is similar and the global maxima do not alter significantly. In summary, rigid registration experiments indicate that the MF-MI keeps sharp peaks and fewer local maxima all along. The main limitation

is in the assumption whether the image features identify enough information-rich pixels in the image for registration. Such issues can be further avoided and improved by other more reliable image feature parameters inclusion from the original image to enhance image registration.

Chapter 6

Image-guided surgery system: Development of data visualization interface with navigation probe-tissue interaction

6.1 Introduction

The development of IGS has mostly started in neurosurgical [118-122] and orthopedic [123-126] applications, and is often associated to minimally invasive interventions. The application of IGS in surgical environment covers several aspects including: identification of target of interest, instrument navigation from entry point to the target and visualization of tracked surgical instruments on reformatted image slices. In order to provide accurate spatial navigation and guidance, IGS relies on the accuracy of coregistration of the patient's position in operating room, patient-specific images generated by CT or MR, and surgical instrument location. This accuracy is dependent on the assumption of accurate initial registration and a static relationship between patient and image model. However, brain tissue deformation and shifting occurs during surgery can compromise this spatial relationship. Since the brain undergoes varying levels of deformations at different stages of the surgery, we are looking at the possibility of building a deformation visualization technique using finite element (FE) methods to simulate the intraoperative brain shift. If the soft tissue deformation could be detected, and update the pre-operative images, then this technology could have a major impact on many more common procedures.

In general, medical data visualization works with either image data or mesh data. Image data refers to DICOM, Tiff, and Jpeg formats. Mesh data are solutions in Vtk, mha, Stl, Abacus, and Ansys formats. Currently there are a few toolkits developed as specialized library for medical image processing and visualization applications. Insight Segmentation and Registration Toolkit (ITK) [127, 128] provides image registration and segmentation algorithm implementations, while visual data representations can be created with the Visualization Toolkit (VTK) [129-131]. Based on ITK and VTK libraries, many visualization frameworks exist to provide higher level functionality and reduce the time to develop new applications. The Medical Imaging Interaction Toolkit (MITK) [132-134] proposes a highly organized library to provide support for high level user interactions in ITK and VTK based medical applications. The Medical Imaging Toolkit [135] is another library for medical image processing and visualization application development. Apart from these toolkits, other groups have developed different tools for medical applications based on ITK and VTK libraries [136]. In contrast to previously described toolkits, our goal in this chapter is to build a prototype visualization display and navigation platform for interpretation of IGS. The main framework is based upon Qt (ver. 4.8.6) and it integrates VTK (ver. 5.10.0) as the rendering kernel. This work is mainly developed by using C++ programming language, which significantly benefits the flexibility and extensibility of the program.

This chapter also presents an analytical model to study the navigation probe-tissue interaction. Brain shift is a complex phenomenon and different reasons causing the brain deformation includes changes in pressure and fluid levels after the dura mater has been opened, physiological reactions to anesthesia and tissue retraction or resection performed

by the surgeon [8, 9, 89]. Although there are many different reasons for brain shift during medical intervention, most of the studies mentioned in the literatures [89, 137] focused in the development of biomechanical models which estimate displacements for the cause of deformation, such as direction of gravity or craniotomy procedure and require intraoperative measurements to constrain their model. The aim of this work is to investigate the pattern of brain deformation with respect to location and magnitude and to consider the implications of this pattern on models for correcting brain deformation in IGS systems. When the interactive force between the tissue and the surgical probe is known and the tissue properties are accurately predicted, the deformation of the tissue or organ can be calculated for visualization. The analytical model accounts for the probe's geometric, material properties, and also the brain tissue's nonlinear material properties. We extracted related anatomical structures from a CT image and generated a FE mesh in order to study the deformation of the brain.

The rest of this chapter presents details of our developed prototype visualization and navigation platform as follows. In Section 6.2, a detailed description of the integration of toolkits and the software architecture is given. We then present the visualization module in Section 6.2.1, and the probe registration module in Section 6.2.2. In Section 6.3, a detailed finite element simulation and implementation work is given. Finally we present some concluding remarks in Section 6.4.

6.2 Software development and architecture

The architecture of the application is based on the IGS system components, as shown in Figure 1.2. It consists of three major software libraries, all implemented in C++, and the

fourth is used for the building process. In this software development work, these versions of the libraries were downloaded:

- VTK version 5.10.0
- ITK version 4.1.0
- Qt SDK version 4.8.6
- CMake version 2.8.11

The Qt library provides a cross-platform framework which is very efficient for developing applications with a graphical user interface (GUI). The library supports all three major platforms (Windows, Mac, and Linux) and creates the applications that look at home in these environments. With the signal/slot mechanism, all the created interface components can be connecting to each other and activated by the GUI elements easily. The VTK library provides the core functionality of the application module and is used in the display of both the mesh formats and DICOM image formats. The ITK library was used to preprocess the DICOM images (finding the proper window/level for the image, finding the number of slices in the DICOM image set, and reading metadata embedded in the DICOM image such as patient name, age, etc.). Although ITK and VTK don't provide any user interface components, they enable complex applications to be built on top of the application level with the help of Qt platform. Figure 6.1 illustrates the basic idea of the system architecture based on these libraries.

An important and challenging aspect of the development of this software module was to integrate all of these libraries correctly. During the initial stage in assessing the structure of the various components, we found out that these libraries interacted in unexpected ways in the difference environments. Thus CMake [138] was used to control

the software compilation process using compiler independent configuration file, CMakeLists.txt. It is a text file that contains the project parameters and specify configuration and build options in simple CMake language. CMake is not directly a compiler tool, but it will generate the native build files and workspaces that can be used in the Microsoft Visual Studio compiler environment [139].

This visualization and navigation module was built to allow effective exploration and visualization of medical data based on ITK and VTK libraries. The use of VTK and ITK for the programming platform was obvious, because it provides a number of state-of-the-art medical data processing algorithms with a strong object-oriented architecture. One of the most valuable features of these libraries is its free availability, which makes it widely used and supported. The backbone of the application is built around the basic VTK pipeline to create visualization and processing module, whereas ITK is used to support I/O of medical image files in DICOM format and provide some preprocessing filters that are not present in VTK. The Qt framework and VTK's pipeline architecture allow us to build a very flexible application, which different modules can be managed separately. Besides, we can easily add a new module to the application without affecting other modules.

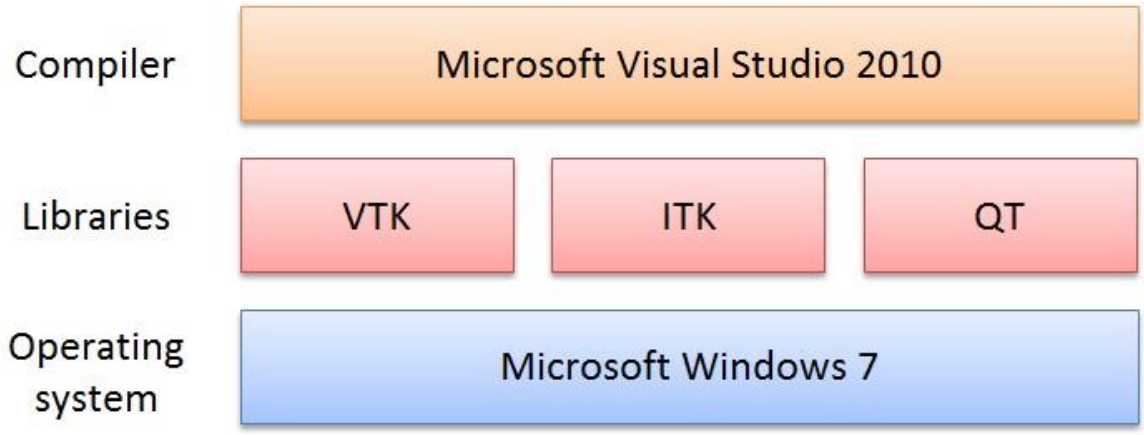

Figure 6.1: General architecture of the software module showing some of the open-source components and libraries that were used.

6.2.1 Volume data visualization

The graphical layout of the software module mirrors those of mainstream visualization applications (e.g. 3D Slicer and OsiriX) with a standard four panel layout where the coronal, axial, sagittal, and 3D views of images are presented. In IGS system, the patient data used for visualization are DICOM image series acquired from MR or CT imaging. DICOM image series is a stack of images, which composed of multiple sequentially scanned images which constitute a 3D volume. When the user loads a DICOM image set, the coronal, axial, and sagittal panels hold the corresponding geometry, and the 3D panel holds an interactive 3D view of the three planes in space. This is shown in Figure 6.2 for CT volume of brain structure. The experimental medical image data used in this figure are provided by Visible Human Project Dataset [140].

To better visualize the brain structure for accurate navigation, interactive slice views are provided in the visualization environment. There are two types of slice views: axis-aligned and arbitrary view. Both allow the user to move the slices interactively

through mouse scroll. Orthogonal axial view is a familiar way of examining patient information to doctors and radiologists because the medical image data are often acquired in axial position. In order to provide different orthogonal orientations (sagittal and coronal views), the multi-planar reformatting was used to obtain any coronal and sagittal 2D image from the original axial view images. The standard three axis-aligned slice views are parallel to the coordinate planes. By determining the normal vector for every plane, such as the normal vector of axial plane is (0, 0, 1) or (0, 0, -1), the position of the three orthogonal planes can be obtained. Multi-planar sectioning, as shown in Figure 6.2, is another approach of visualizing the three orthogonal views stacked perpendicular to each other to create a 3D visualization. By simultaneously displaying all three orthogonal views, the doctors can view the brain structure from multiple directions at the same time and examine the patient data comprehensively. Axis-aligned view provides orthogonal views of volumetric data, but the constraint on slice directions limits the freedom of interactive viewing and examination. In various clinical applications, it is at times necessary to view cross sections made at arbitrary angles through the volumetric data. As the shapes of the target of interest are usually irregular, a user-defined cutting plane with arbitrary orientations may further help the doctors to obtain information of the brain structure from arbitrary angles, as shown in Figure 6.3. This view can be navigated through the "click and drag" method of manipulating an orthogonal plane within one of the three views of the volume, causing other views to be reformatted according to the new viewpoint position.

The visualization panels allow user interaction through intuitive mouse control. The DICOM set loaded into the 3D panel can be rotated in any direction to view different

side of the DICOM image. The contrast (window/level) of the DICOM images can be adjusted by the standard left mouse click in any window containing a DICOM image to increase or decrease the DICOM image contrast. The contrast settled on in this adjustment will apply to all other windows in the application.

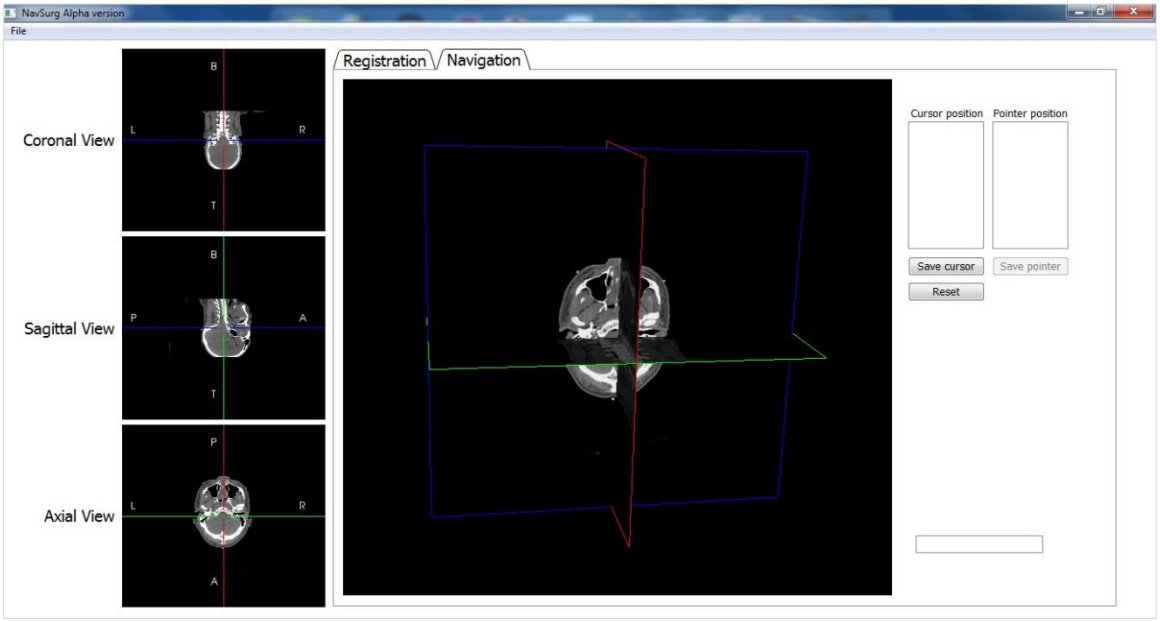

Figure 6.2: A four panel windows display of application module is shown. The window consists of axial, coronal, sagittal, and 3D overlaid display. The cross hairs shown in the 2D images are synchronized to allow users to localize a specific region in 2D and the same region in 3D.

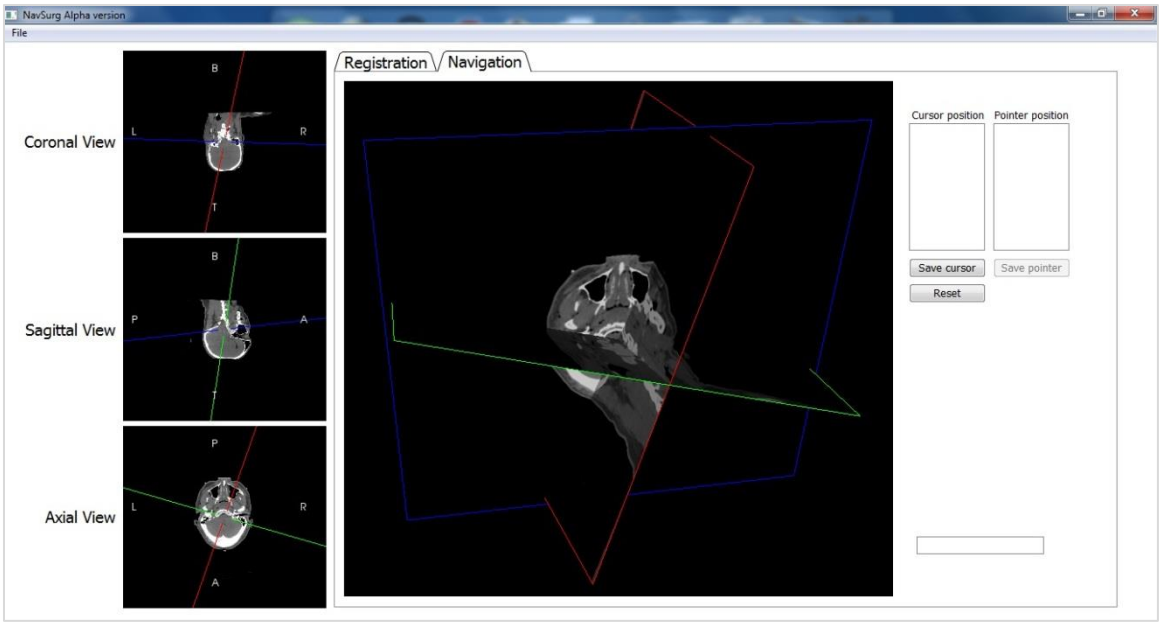

Figure 6.3: Arbitrary slice view is shown. Thumbnails at left are the cutting planes applied to different orthogonal views, and the resulting 3D volume is in the center.

6.2.2 Navigation probe registration

The navigation probe tracking allows the visualization of the brain and the probe display inside the virtual environment. Figure 6.4 shows a photograph of the 3D mock operating room setup being used to perform image-guided navigation with the patient data. A 3D rapid prototyped physical biomodel was reconstructed from the CT scans by CBMTI Pte Ltd, Kuala Lumpur. It was used as the "patient" and a simple robotic arm built by Amir, University Malaya, was used to provide real-time physical coordinates. A line widget was created as a virtual pointer to give more specific control to the users. Before the navigation was performed, it is necessary to register the image space to the tracked instrument. To establish the registration, positions of the pair points in image space and physical space must be obtained. The pair points are selected by clicking on corresponding image slices manually and capture the corresponding position at the

physical patient through robotic arm respectively. Coordinate information provided by the software module helps the user to position and reposition the probe to accurately locate the features of the calibration object in the image. The medical image was then registered to the physical position of the patient model using standard image-to-patient rigid transformations to connect the coordinate system of the model to the actual patient data. The navigation probe can be visualized on preoperative images according to its position in the physical coordinates as shown in Figure 6.5.

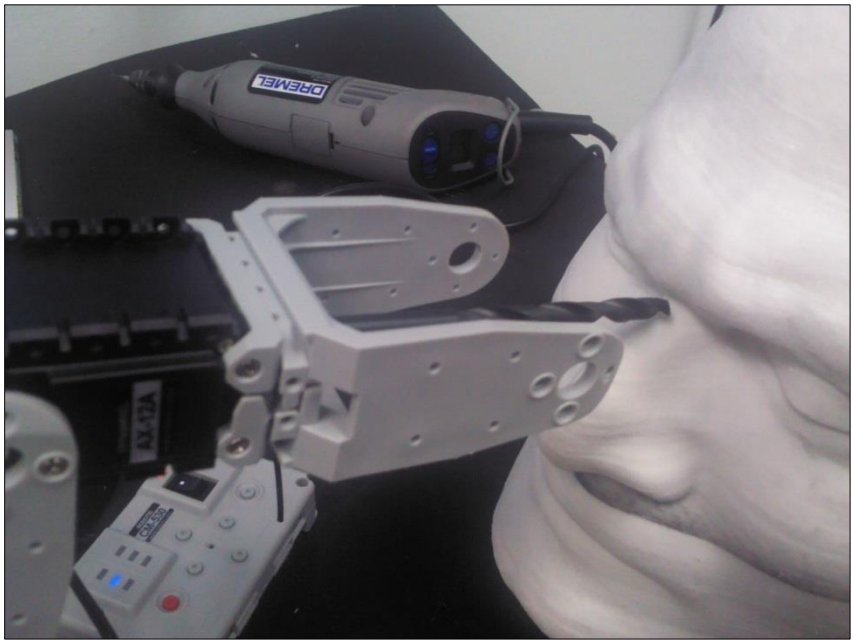

Figure 6.4: A photograph of the 3D mock operating room setup being used to perform image-guided navigation with the artificial patient.

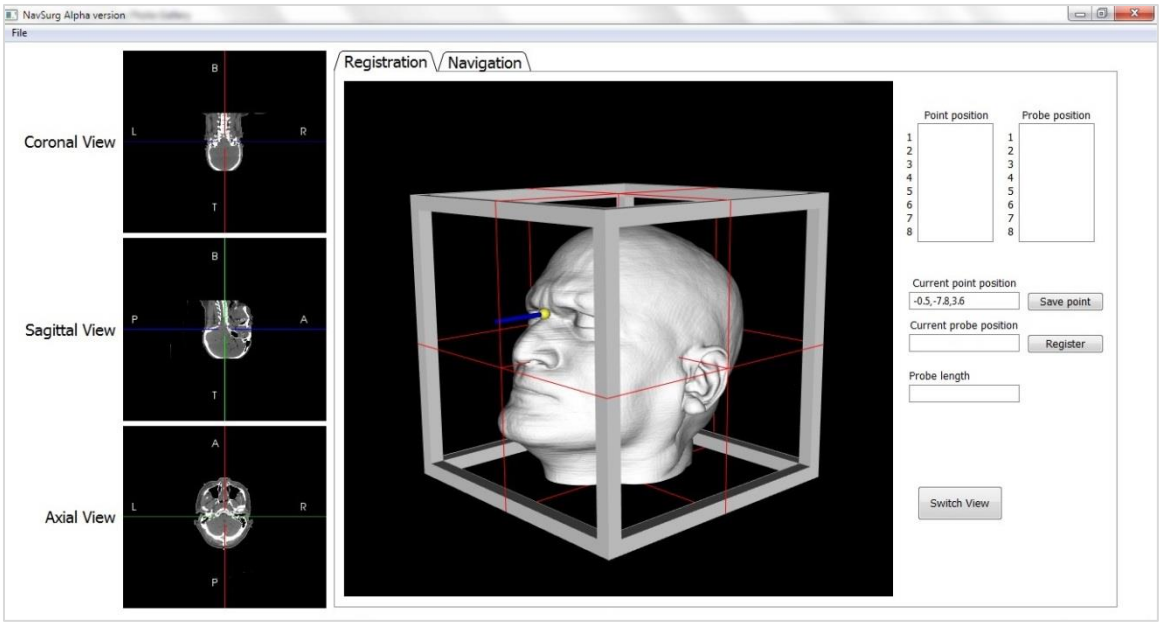

Figure 6.5: The probe is being tracked and a line widget is used to indicate the position in the system.

6.3 Modeling of navigation probe-tissue interaction

This section presents an analytical model to study the navigation probe-tissue interaction. The aim of this work is to investigate the pattern of brain deformation with respect to location and magnitude and to consider the implications of this pattern on models for correcting brain deformation in IGS systems. When the interactive force between the tissue and the surgical probe is known and the tissue properties are accurately predicted, the deformation of the tissue or organ can be calculated for visualization. The model accounts for the probe's geometric, material properties, and also the brain tissue's nonlinear material properties. We extracted related anatomical structures from a CT image and generated a FE mesh in order to study the deformation of the brain.

6.3.1 Finite element implementation

In this section, a computational analysis was carried out to determine the deformation and stress tensor experienced by the brain tissue of the corresponding mechanical loading force. For the purpose of illustrating the concepts abound in this study, a 3D rapid prototyped physical biomodel was reconstructed from the CT scans by CBMTI Pte Ltd, Kuala Lumpur. Figure 6.6 shows this model with the probe pointing at the slice with the region of interest. From a numerical point of view, this is a highly nonlinear structural analysis, mainly due to the contact interaction between the brain and the navigation probe (stainless steel grade 316), and also the geometrical nonlinearity originating from the large displacement. In order to perform FE analysis, we used a commercially available software, COMSOL Multiphysics [141]. COMSOL Multiphysics is a general purpose software package for solving problems that are based on partial differential equations (PDEs). This study was done in two-dimensional space and the dependent variables u and v was defined as displacements field components according to coordinate system axes. As this study aimed to perform a simulation based on a patient-specific brain model, a few assumptions have to be made prior to the simulation.

- A relatively idealized brain model was used to carry out the FEM simulation without introducing pathological information. This brain model is anatomically based on a normal adult's brain and physically based on a mechanical model generalized from experimental data reported on literature [142].
- The mechanism governing the brain shift during neurosurgery is very complicated as mentioned in the literature review. Thus, a simplified mechanism was assumed that the outer surface of the brain is fixed to the inner surface of the skull, which

prevents the brain from moving under the influence of gravity. The exposed surface and the nearby regions are free to move but the remaining surfaces are fixed. The scalp and the skull are not considered to influence the mechanical response of the brain to the quasi-static loading conditions and will be ignored in this study.

- Brain tissues are recognized as an anisotropic inhomogeneous material and exhibit different mechanical behaviors under different surgical or pathological conditions. In this study, simulation of a general homogeneous and isotropic brain model was used.

Figure 6.6: A 3D rapid prototyped physical biomodel reconstructed from the CT scans with the probe pointing at the slice with the region of interest by CBMTI Pte Ltd, Kuala Lumpur.

The brain tissue deformation when interacting with navigation probe is fundamentally governed by the following factors: (1) brain geometry, (2) brain tissue properties, and (3) boundary constraints due to surrounding structures that support the

brain. To determine the patient-specific brain geometry, we extracted the geometric information from an axial view of a CT image, which was acquired from a 128 slices dual source Siemens CT imaging system in University Malaya Medical Centre (UMMC). As opposed to other imaging modalities, CT images have larger field of view and produce higher resolution of detail for brain structure, which in turn results in better segmentation of brain geometry. The brain tissue was manually segmented out using a Digital Imaging and Communications in Medicine (DICOM) processing software BioModroid (CBMTI Pte Ltd, Kuala Lumpur) and is indicated by green lines as two-dimensional contour shown in Figure 6.7(a). The image slice was exported as a jpeg image which was then imported into WinTopo (Softsoft Pte Ltd, UK) to convert from raster into dxf, a vector format. This geometry object file was imported into COMSOL Multiphysics to carry out the FE analysis. The surgical probe is created by using rectangle geometry with the diameter of 6mm. Figure 6.7(b) shows the imported brain geometry model and the probable surgical probe insertion location.

The finite element model was generated by dividing all the domains into smaller unit called mesh unit. The meshing of the model was discretized with the free triangle technique. In order to achieve computational efficiency while maintaining accurate FE analysis, only the surface boundary was discretized with extremely fine mesh elements as shown in Figure 6.7(c). The FE mesh generated consisted of 21,786 elements with degree of freedom is approximately 90,450. To solve the constitutive equations governing the model, boundary conditions should be indicated properly. In this work, we assume that the regions nearby the contact surface are free to move but the remaining boundaries of the brain are fixed to the skull and no relative movement is allowed. A prescribed loading

was imposed by a pressure parameter load of 10N/m^2 at the probe boundary constituting a force profile. For the purpose of this experiment, it is assumed that the surgical probe will only move in a uniform linear motion along the x+ direction of the movement, while the y and z directions and all possible rotations were constrained.

Based on the available experiment data on brain tissues from literatures, we chose to model the brain as a nonlinear viscoelastic material which is valid for large deformation case. Most soft tissues are inherently viscoelastic because its stress response exhibit both viscous fluids and elastic solids characteristics. Similar to elastic materials, the elastic response is instantaneous while the viscous part occurs over time. For the homogeneous modeling, the whole brain was treated as a homogenous isotropic material. The brain tissue with white and gray matter were assigned with same material properties, using parameters obtained from literature [142]: tissue density, p = 1000kg/m3, Young's modulus, E = 2100Pa, Poisson's ratio, ν =0.45, bulk modulus, k = 1.24E8 N/m^2, and shear modulus, G = 6.20E6 N/m^2.

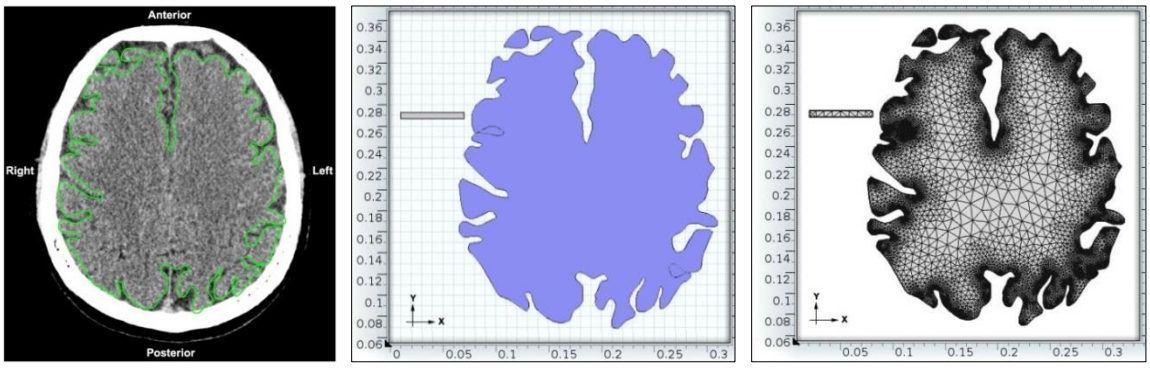

(a) (b) (c)

Figure 6.7: (a) Segmented CT image of the brain tissue used to construct a patient specific brain model. (b) The design of the brain model with surgical probe. (c) The meshing of the model generated by the software.

6.3.2 Simulation results and discussion

Surgical probe insertion procedures are primarily displacement driven problems, and our results indicate that the deformation response of the brain tissue is sensitive to boundary conditions surrounding it. The stationary simulation was performed using COMSOL Multiphysics, a commercially available FE solver. Figure 6.8 shows the region of interest, Region B where the probe and brain tissue come in contact. Point A is set to be the evaluation point of the displacement value. The point is selected near the contact surface due to larger displacements occur in this area relative to the other area. Figure 6.10 presents the simulation results of the brain tissue deformation where large deformation and stress is shown in red and small deformation is shown in blue. The Von Mises criteria was used for combining the stresses in all dimensions into an equivalent stress, which is then compared to the yield stress of the brain tissue. The equation for von Mises stress is shown below.

$$\sigma = \sqrt{\sigma_{xx}^2 + \sigma_{yy}^2 - \sigma_{xx}\sigma_{yy} + 3\tau_{xy}^2} \tag{41}$$

where σ correspond to normal stress values, and τ is the shear stress value.

The results show that the deformations in the brain models are smooth and this indicates that our simulation is realistic. The initial 4 images (a-d) depict the probe with the force acting on the tip. After the probe breaks the brain tissue's surface tension as shown in Figure 6.10(d), the probe continues moving into the brain and the subsequent images have the force acting on the tip as well as around the probe's contact surface with the brain i.e. in the direction y+ and y-. Figure 6.9 shows a progression timeline of the Von mises stress value at different tool positions. The navigation probe breaks the tissue's

surface tension at (a) and continues moving into the brain at (b). The stress values continue to increase as the probe is moving in because probe is approaching to the evaluation point. The Von mises stress reach the highest value at the last position which is the nearest to the evaluation point, point A. Table 6.1 presents the Von mises stress value for different tool positions at a tabular format.

This simulation results provide useful information about the probe-tissue contact modeling. By using the proper force parameter and the tissue properties, approximate deformation of the brain tissue can be determined. In addition, the deformation function can also be used to calculate and compensate the displacements of the anatomical landmarks on the contact surface of the brain due to brain shift effect. Most importantly, this technique does not use intraoperative imaging modality to determine the coordinates of preoperative points corresponding to specific intraoperative points.

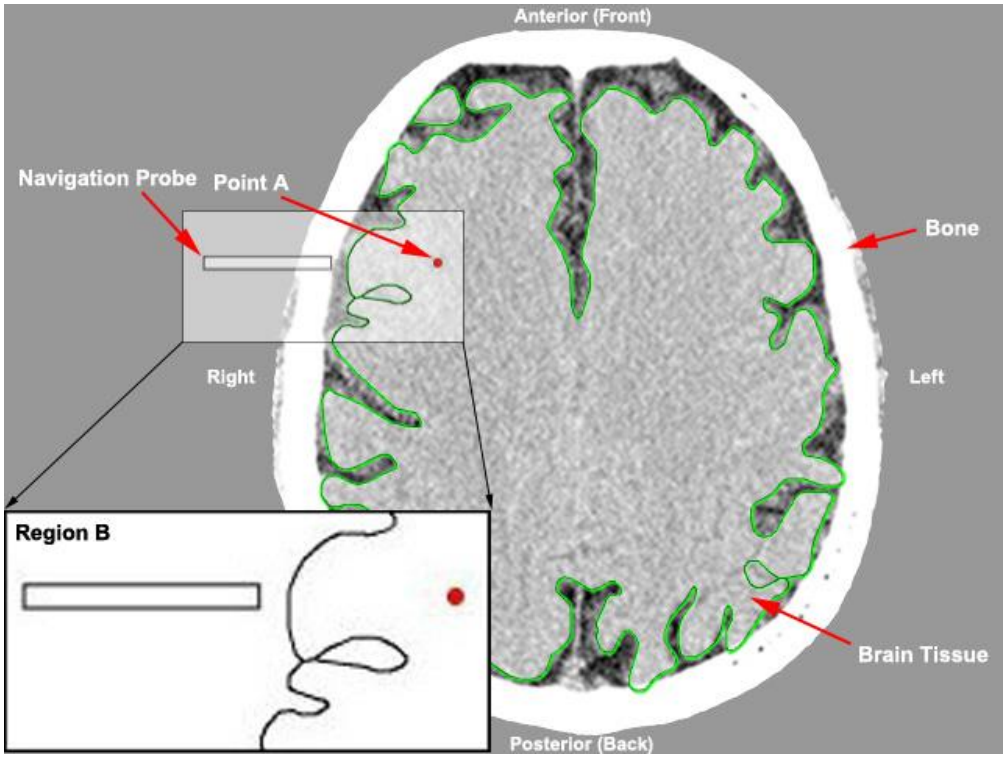

Figure 6.8: Point A is the point of evaluation of the total displacement values. Region B refers to the region of interest where the FE analysis was focused upon.

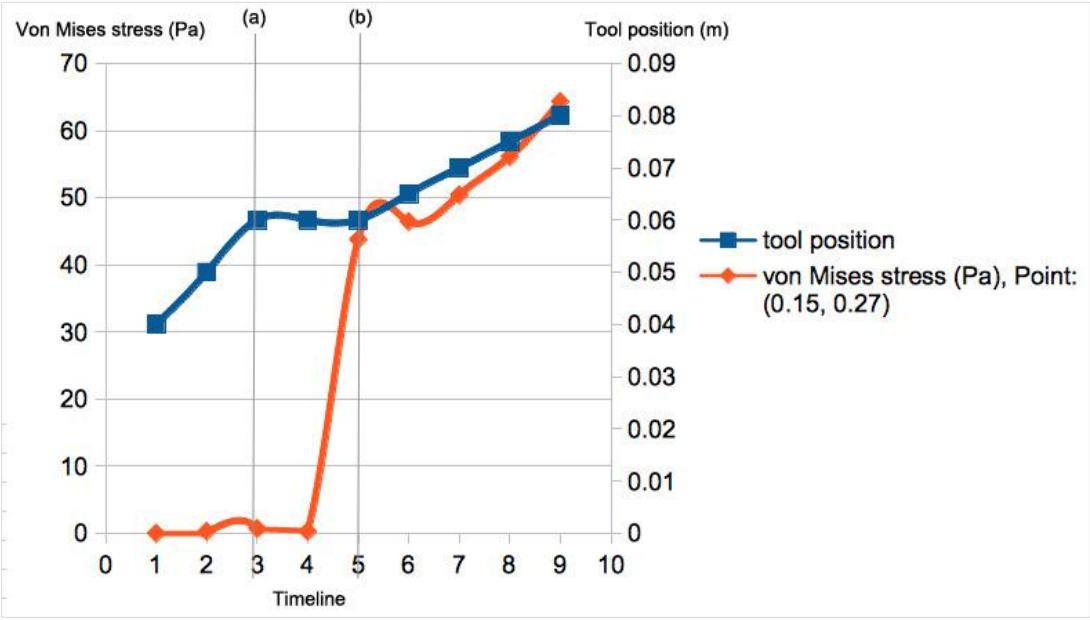

Figure 6.9: A progression timeline of the Von mises stress value at different tool positions.

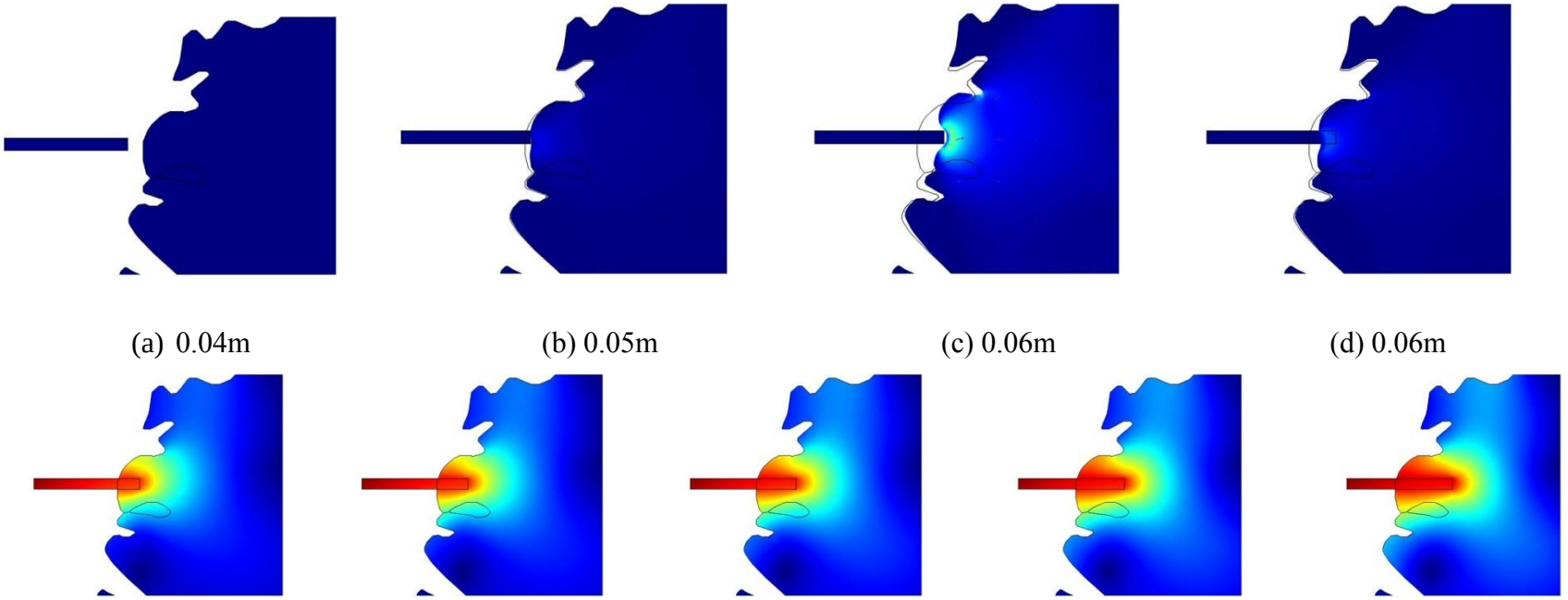

(a) 0.04m (b) 0.05m (c) 0.06m (d) 0.06m

(e) 0.06m (f) 0.065m (g) 0.07m (h) 0.075m (i) 0.08m

Figure 6.10: Finite element simulation results of brain tissue deformation during the insertion of the probe at different time unit.

Time unit	1	2	3	4	5	6	7	8	9
Tool position (m)	0.04	0.05	0.06	0.06	0.06	0.065	0.07	0.075	0.08
von Mises stress (Pa)	0	0.2863	0.71574	0.2863	43.7533	46.41968	50.38694	56.07243	64.28564

Table 6.1: Von mises stress value for different tool positions at the evaluation point (0.15, 0.27).

6.4 Conclusion

In this chapter, a visualization and navigation platform prototype was designed and realized based on the data visualization function of VTK and the image processing function of ITK. Qt library was used to provide graphical user interface elements to the system. This simple visualization system is useful for advancing the development work on image processing and brain tissue deformation function of IGS system. Using VTK to establish visualization subsystem can reduce numerous repeated tasks, which we can focus more on the algorithms and system design. This chapter also presents a simple biomodel to analyze the deformation and stress tensor experienced by the brain tissue during surgical operations. FE method was used for discretizing and solving the PDEs that describe the brain tissue deformation. Simulation results have showed that the brain shape deformations and the stress experience around the probe tip. Based on the observation of the simulation results, the deformation of the brain tissue of the probe insertion can be classified into the following three distinct phases:

- First, the brain undergoes elastic deformation as the tip of the navigation probe indents the outer surface of the brain prior to puncturing the brain's tissue.
- Second, the probe displacement induces a load on the brain surface. When this load reaches a critical threshold, the brain tissue ruptures. The rupture process is characterized by a sharp and recognizable peak in the deformation graph.
- Third, following rupture, the probe penetrates the tissue by cutting its surface.

Finally, based on the construction of a visualization software platform, the future work will be extended to the data processing module to implement brain tissue deformation which was discussed in the modeling section. By modeling, it gives us some simulation data on actual implementation of the system. As a conclusion, modeling an accurate simulation of brain tissue deformation is rather a complex task. The brain tissue is not only inhomogeneous and anisotropy, but also the complex properties and mechanical processes have to be taken into account. However, we hope to have laid a foundation on the future research to profile the stress values around navigation area to further model the image deformation.

Chapter 7

Conclusion and future work

7.1 Summary and contributions

Image-guided surgery is a new, rapidly evolving paradigm that will change the way surgery will be performed in the future. The development of new techniques that enhance visual image interpretation in an accurate manner is always the focus in medical research field. The aim of this thesis is to contribute to the research of two of these techniques, image registration and brain tissue deformation modeling. The contributions of this research are summarized as follows:

- **A point set registration method using points and curves feature**. We introduce the idea that the points and curves feature are applied into the nonlinear image registration, which has the accuracy of registration based on points and the robustness of registration based on curves feature. The proposed method is using hybrid approach in feature correspondence stage.
- **The incorporation of spatial information in Adaptive Mutual Information (AMI)**. The proposed method uses a simple way to enrich the image description by integrating the gradient information. The decision to choose gradient information is motivated by the fact that the image locations with a strong gradient have high information value, which could be useful for the image registration. Salient pixels in the regions with high gradient value will contribute more in the estimation of similarity metric of image pairs being registered.

- **Extension of the standard single feature MI similarity measure to a multi-features MI (MF-MI)**. One major contribution of MF-MI method is the incorporation of multiple image features into MI method to solve the problem of joint probability distribution estimation in a multi-dimensional feature space. Furthermore, the proposed MF-MI measure can be computed for a number of additional features, as long as these features provide the same output image resolution. From the vast amount of feature choices that describe the structural information of images, we have tested the standard deviation filter and proposed a new adaptive gradient magnitude image feature for our study.
- **The study to analyze the navigation probe-tissue interaction**. The computational analysis was carried out to determine the deformation and stress tensor experienced by the brain tissue of the corresponding mechanical loading force. The simulation results provide useful information about the probe-tissue contact modeling. This analytical model laid a foundation on the future research to profile the pattern of brain tissue deformation around navigation area to further model the image deformation.
- **The development of a prototype visualization display and navigation platform for interpretation of IGS**. The main framework was designed and realized based on the data visualization function of VTK and the image processing function of ITK. By utilizing the Qt library, it overcomes the main drawback of the toolkit, while maintaining the object oriented concept of VTK and ITK. This simple visualization system is useful for our future work to extend

the data processing module to implement brain tissue deformation which was discussed in the previous chapters.

7.2 Future work

The work presented in this thesis can be expanded in different directions. Following research tasks have been outlined and can be undertaken for future research and development.

- Since the MF-MI similarity metric provided very good results, a next step in our research would consist in investigating and evaluating the similarity metric for affine and nonrigid registration. Furthermore we would like to investigate the proposed method on an even wider range of spatial features combination.
- The increasing capabilities of computer hardware resources encourage us to explore the implementation of the image registration with the fast GPU and parallel processing. Moreover, we would analyze the efficiency of the standard mutual information with the proposed MF-MI measure and other strategies to deal with the high-dimensional medical images.
- Availability and quality of clinical data is always a concern throughout our research project. Although the registration results are satisfactory based on the available clinical data, it is not conclusive enough that our method is suitable for all types of medical images and clinical scenario. We hope to confirm the success rate of the method by validating a large number of input images.
- In order to provide updated image guidance to the surgeon that incorporate realistic tool-tissue interaction models, some significant challenges need to be overcome. The three main hurdles that need to be overcome are: first, formulating

a methodology to incorporate the experimental result of the FE analysis framework to simulate realistic brain tissue deformations; second, making simplifications to the computational model such that the simulation runs in real time but does not sacrifice the realistic deformation response; and finally, the significant issue of clinical validation must be addressed.

- Modeling soft tissue retraction and resection provides another significant topic of research. However, there is no effective way of tracking exactly which tissue has been resected even now and the development of research is still in its infancy. Modeling the effects of tissue resection is similarly difficult.

References

[1] T. C. Russakoff. Daniel B, Rohlfing. Torsten, Maurer Jr. Calvin R, "Image similarity using mutual information of regions," in *Computer Vision-ECCV 2004*, ed: Springer, 2004, pp. 596-607.

[2] PubMed. (2014, 14/1/2014). *PubMed database*. Available: http://www.ncbi.nlm.nih.gov/pubmed/?term=image+guided+surgery

[3] F. Maes, Collignon, A., Vandermeulen, D., Marchal, G., Suetens, P., "Multimodality image registration by maximization of mutual information," *IEEE Transactions on Medical Imaging, ,* vol. 16, pp. 187-198, 1997.

[4] P. Viola and W. M. Wells III, "Alignment by maximization of mutual information," *International Journal of Computer Vision*, vol. 24, pp. 137-154, 1997.

[5] J. West, J. M. Fitzpatrick, M. Y. Wang, B. M. Dawant, C. R. Maurer, Jr., R. M. Kessler, *et al.*, "Comparison and Evaluation of Retrospective Intermodality Brain Image Registration Techniques," *Journal of Computer Assisted Tomography July/August*, vol. 21, pp. 554-568, 1997.

[6] F. Maes, D. Vandermeulen, and P. Suetens, "Medical image registration using mutual information," *Proceedings of the IEEE*, vol. 91, pp. 1699-1722, 2003.

[7] S. P. Loeckx. Dirk, Maes. Frederik, Vandermeulen. Dirk, Suetens. Paul, "Nonrigid image registration using conditional mutual information," *IEEE Transactions on Medical Imaging, ,* vol. 29, pp. 19-29, 2010.

[8] D. W. Roberts, A. Hartov, F. E. Kennedy, M. I. Miga, and K. D. Paulsen, "Intraoperative brain shift and deformation: a quantitative analysis of cortical displacement in 28 cases, Neurosurgery 43 (4," ed, 1998, pp. 749--760.

[9] P. Dumpuri, R. C. Thompson, C. Aize, D. Siyi, I. Garg, B. M. Dawant, *et al.*, "A Fast and Efficient Method to Compensate for Brain Shift for Tumor Resection Therapies Measured Between Preoperative and Postoperative Tomograms," *IEEE Transactions on Biomedical Engineering, ,* vol. 57, pp. 1285-1296, 2010.

[10] C. Nimsky, O. Ganslandt, S. Cerny, P. Hastreiter, G. Greiner, and R. Fahlbusch, "Quantification of, visualization of, and compensation for brain shift using intraoperative magnetic resonance imaging," *Neurosurgery*, vol. 47, pp. 1070-9; discussion 1079-80, Nov 2000.

[11] I. Chen, A. M. Coffey, D. Siyi, P. Dumpuri, B. M. Dawant, R. C. Thompson, *et al.*, "Intraoperative Brain Shift Compensation: Accounting for Dural Septa," *IEEE Transactions on Biomedical Engineering, ,* vol. 58, pp. 499-508, 2011.

[12] T. Hartkens, D. L. G. Hill, A. D. Castellano-Smith, D. J. Hawkes, C. R. Maurer, Jr., A. J. Martin, *et al.*, "Measurement and analysis of brain deformation during neurosurgery," *IEEE Transactions on Medical Imaging, ,* vol. 22, pp. 82-92, 2003.

[13] J. B. A. Maintz and M. A. Viergever, "A survey of medical image registration," *Medical Image Analysis,* vol. 2, pp. 1-36, 1998.

[14] B. Zitová and J. Flusser, "Image registration methods: a survey," *Image and Vision Computing,* vol. 21, pp. 977-1000, 2003.

[15] M. S. Alp, M. Dujovny, M. Misra, F. T. Charbel, and J. I. Ausman, "Head registration techniques for image-guided surgery," *Neurol Res,* vol. 20, pp. 31-7, Jan 1998.

[16] G. Eggers, J. Mühling, and R. Marmulla, "Image-to-patient registration techniques in head surgery," *International Journal of Oral and Maxillofacial Surgery,* vol. 35, pp. 1081-1095, 2006.

[17] L. Zagorchev and A. Goshtasby, "A comparative study of transformation functions for nonrigid image registration," *IEEE Transactions on Image Processing, ,* vol. 15, pp. 529-538, 2006.

[18] M. A. Wirth, C. Choi, and A. Jennings, "Point-to-point registration of non-rigid medical images using local elastic transformation methods," in *Image Processing and Its Applications, 1997., Sixth International Conference on*, 1997, pp. 780-784 vol.2.

[19] D. L. G. Hill, D. J. Hawkes, J. E. Crossman, M. J. Gleeson, T. C. S. Cox, E. E. C. M. L. Bracey, *et al.*, "Registration of MR and CT images for skull base surgery using point-like anatomical features," *Br J Radiol,* vol. 64, pp. 1030-1035, November 1, 1991 1991.

[20] M. A. Audette, F. P. Ferrie, and T. M. Peters, "An algorithmic overview of surface registration techniques for medical imaging," *Medical Image Analysis,* vol. 4, pp. 201-217, 2000.

[21] M. Carla Gilardi, G. Rizzo, A. Savi, C. Landoni, V. Bettinardi, C. Rossetti, *et al.*, "Correlation of SPECT and PET cardiac images by a surface matching registration technique," *Computerized Medical Imaging and Graphics,* vol. 22, pp. 391-398, 1998.

[22] N. R. al-Rodhan and P. J. Kelly, "Pioneers of stereotactic neurosurgery," *Stereotact Funct Neurosurg,* vol. 58, pp. 60-6, 1992.

[23] R. J. Maciunas, R. L. J. Galloway, and J. W. Latimer, "The Application Accuracy of Stereotactic Frames," *Neurosurgery*, vol. 35, pp. 682-695, 1994.

[24] C. W. Burckhardt, P. Flury, and D. Glauser, "Stereotactic brain surgery," *Engineering in Medicine and Biology Magazine, IEEE*, vol. 14, pp. 314-317, 1995.

[25] A. Krol, M. Z. Unlu, K. G. Baum, J. A. Mandel, W. Lee, I. L. Coman, *et al.*, "MRI/PET nonrigid breast-image registration using skin fiducial markers," *Physica Medica*, vol. 21, pp. 39-43, 2006.

[26] C. R. Maurer, Jr., J. M. Fitzpatrick, M. Y. Wang, R. L. Galloway, Jr., R. J. Maciunas, and G. S. Allen, "Registration of head volume images using implantable fiducial markers," *IEEE Transactions on Medical Imaging, ,* vol. 16, pp. 447-462, 1997.

[27] K. L. Holloway, S. E. Gaede, P. A. Starr, J. M. Rosenow, V. Ramakrishnan, and J. M. Henderson, "Frameless stereotaxy using bone fiducial markers for deep brain stimulation," *Journal of Neurosurgery*, vol. 103, pp. 404-413, 2011/06/19 2005.

[28] T. Peters, K. Cleary, W. Birkfellner, J. Hummel, and E. Wilson, "Tracking Devices," in *Image-Guided Interventions*, ed: Springer US, 2008, pp. 23-44.

[29] K. Cleary and T. M. Peters, "Image-Guided Interventions: Technology Review and Clinical Applications," *Annual Review of Biomedical Engineering*, vol. 12, pp. 119-142, 2010.

[30] K. Cleary, Z. Hui, N. Glossop, E. Levy, B. Wood, and F. Banovac, "Electromagnetic Tracking for Image-Guided Abdominal Procedures: Overall System and Technical Issues," in *Engineering in Medicine and Biology Society, 2005. IEEE-EMBS 2005. 27th Annual International Conference of the*, 2005, pp. 6748-6753.

[31] A. Bosnjak, G. Montilla, R. Villegas, and I. Jara, "An Electromagnetic Tracking System for Surgical Navigation with registration of fiducial markers using the iterative closest point algorithm," in *Information Technology and Applications in Biomedicine (ITAB), 2010 10th IEEE International Conference on*, 2010, pp. 1-5.

[32] F. Poulin and L. P. Amiot, "Interference during the use of an electromagnetic tracking system under OR conditions," *Journal of Biomechanics*, vol. 35, pp. 733-737, 2002.

[33] J. B. West and C. R. Maurer, Jr., "Designing optically tracked instruments for image-guided surgery," *IEEE Transactions on Medical Imaging, ,* vol. 23, pp. 533-545, 2004.

[34] F. Watzinger, W. Birkfellner, F. Wanschitz, W. Millesi, C. Schopper, K. Sinko, *et al.*, "Positioning of dental implants using computer-aided navigation and an optical tracking system: case report and presentation of a new method," *Journal of Cranio-Maxillofacial Surgery,* vol. 27, pp. 77-81, 1999.

[35] N. D. Glossop, "Advantages of optical compared with electromagnetic tracking," *J Bone Joint Surg Am,* vol. 91 Suppl 1, pp. 23-8, Feb 2009.

[36] D. P. Perrin, N. V. Vasilyev, P. Novotny, J. Stoll, R. D. Howe, P. E. Dupont, *et al.*, "Image guided surgical interventions," *Curr Probl Surg,* vol. 46, pp. 730-66, Sep 2009.

[37] W. E. Lorensen and H. E. Cline, "Marching cubes: A high resolution 3D surface construction algorithm," *SIGGRAPH Comput. Graph.,* vol. 21, pp. 163-169, 1987.

[38] L. G. Brown, "A survey of image registration techniques," *ACM Comput. Surv.,* vol. 24, pp. 325-376, 1992.

[39] C. A. Pelizzari, G. T. Chen, D. R. Spelbring, R. R. Weichselbaum, and C.-T. Chen, "Accurate three-dimensional registration of CT, PET, and/or MR images of the brain," *Journal of Computer Assisted Tomography,* vol. 13, pp. 20-26, 1989.

[40] G. Borgefors, "Hierarchical chamfer matching: a parametric edge matching algorithm," *IEEE Transactions on Pattern Analysis and Machine Intelligence, ,* vol. 10, pp. 849-865, 1988.

[41] P. J. Besl and H. D. McKay, "A method for registration of 3-D shapes," *IEEE Transactions on Pattern Analysis and Machine Intelligence, ,* vol. 14, pp. 239-256, 1992.

[42] M. Kass, A. Witkin, and D. Terzopoulos, "Snakes: Active contour models," *International Journal of Computer Vision,* vol. 1, pp. 321-331, 1988.

[43] D. Shen, E. H. Herskovits, and C. Davatzikos, "An adaptive-focus statistical shape model for segmentation and shape modeling of 3-D brain structures," *IEEE Transactions on Medical Imaging, ,* vol. 20, pp. 257-270, 2001.

[44] P. A. Yushkevich, J. Piven, H. C. Hazlett, R. G. Smith, S. Ho, J. C. Gee, *et al.*, "User-guided 3D active contour segmentation of anatomical structures: significantly improved efficiency and reliability," *Neuroimage,* vol. 31, pp. 1116-1128, 2006.

[45] F. Leymarie and M. D. Levine, "Tracking deformable objects in the plane using an active contour model," *IEEE Transactions on Pattern Analysis and Machine Intelligence, ,* vol. 15, pp. 617-634, 1993.

[46] X. Wang and D. D. Feng, "Active contour based efficient registration for biomedical brain images," *Journal of Cerebral Blood Flow & Metabolism*, vol. 25, pp. S623-S623, 2005.

[47] H. Li, B. Manjunath, and S. K. Mitra, "A contour-based approach to multisensor image registration," *IEEE Transactions on Image Processing, ,* vol. 4, pp. 320-334, 1995.

[48] X. Y. Wang, S. Eberl, M. Fulham, S. Som, D. D. Feng, and F. David Dagan, "Data Registration and Fusion," in *Biomedical Information Technology*, ed Burlington: Academic Press, 2008, pp. 187-210.

[49] P. A. Van den Elsen, J. A. Maintz, E.-J. Pol, and M. A. Viergever, "Automatic registration of CT and MR brain images using correlation of geometrical features," *IEEE Transactions on Medical Imaging, ,* vol. 14, pp. 384-396, 1995.

[50] B.Balasubramanian and D. K. Porkumaran, "PET/CT and MR Image Registration using Normalized Cross Correlation Algorithm and Spatial Transformation Techniques," *International Journal of Computer and Network Security,* vol. 2, pp. 25-29, 2010.

[51] C. E. Shannon, "A Mathematical Theory of Communication," *Bell System Technical Journal,* vol. 27, pp. 379-423, 1948.

[52] T. M. Cover and J. A. Thomas, "Elements of information theory," ed: New York: Wiley, 1991.

[53] J. P. W. Pluim, J. B. A. Maintz, and M. A. Viergever, "Mutual-information-based registration of medical images: a survey," *IEEE Transactions on Medical Imaging, ,* vol. 22, pp. 986-1004, 2003.

[54] A. B. Hamza and H. Krim, "Image registration and segmentation by maximizing the jensen-rényi divergence," in *Energy Minimization Methods in Computer Vision and Pattern Recognition*, 2003, pp. 147-163.

[55] Y. He, A. B. Hamza, and H. Krim, "A generalized divergence measure for robust image registration," *IEEE Transactions on Signal Processing, ,* vol. 51, pp. 1211-1220, 2003.

[56] G. Jumarie, "A new information theoretic approach to the entropy of non-random discrete maps relation to fractal dimension and temperature of curves," *Chaos, Solitons & Fractals,* vol. 8, pp. 953-970, 1997.

[57] C. E. Rodriguez-Carranza and M. H. Loew, "Weighted and deterministic entropy measure for image registration using mutual information," in *Medical Imaging'98*, 1998, pp. 155-166.

[58] C. Tsallis, "Possible generalization of Boltzmann-Gibbs statistics," *Journal of Statistical Physics,* vol. 52, pp. 479-487, 1988.

[59] P. K. Kalra and N. Kumar, "An automatic image registration scheme using Tsallis entropy," *Biomedical Signal Processing and Control,* vol. 5, pp. 328-335, 2010.

[60] S. Sun, L. Zhang, and C. Guo, "Medical Image Registration by Minimizing Divergence Measure Based on Tsallis Entropy," *International Journal of Biological and Medical Sciences,* vol. 2, pp. 75-80, 2007.

[61] J. Havrda and F. Charvát, "Quantification method of classification processes. Concept of structural $ a $-entropy," *Kybernetika,* vol. 3, pp. (30)-35, 1967.

[62] M. P. Wachowiak, R. Smolíková, and T. M. Peters, "Multiresolution biomedical image registration using generalized information measures," in *Medical Image Computing and Computer-Assisted Intervention-MICCAI 2003,* ed: Springer, 2003, pp. 846-853.

[63] T. M. Cover and J. A. Thomas, "Entropy, Relative Entropy, and Mutual Information," in *Elements of Information Theory,* 2 ed Hoboken, NJ, USA: John Wiley & Sons, Inc., 2005, pp. 13-55.

[64] L. Junck, J. G. Moen, G. D. Hutchins, M. B. Brown, and D. E. Kuhl, "Correlation methods for the centering, rotation, and alignment of functional brain images," *Journal of Nuclear Medicine: official publication, Society of Nuclear Medicine,* vol. 31, p. 1220, 1990.

[65] Y.-M. Zhu and S. M. Cochoff, "Influence of Implementation Parameters on Registration of MR and SPECT Brain Images by Maximization of Mutual Information," *J Nucl Med,* vol. 43, pp. 160-166, February 1, 2002 2002.

[66] C. A. Wells. William, Delp. Scott, Gaens. Tom, Maes. Frederik, Vandermeulen. Dirk, Suetens. Paul, "Non-rigid Multimodal Image Registration Using Mutual Information," in *Medical Image Computing and Computer-Assisted Interventation — MICCAI'98*. vol. 1496, ed: Springer Berlin / Heidelberg, 1998, p. 1099.

[67] C. Studholme, D. L. G. Hill, and D. J. Hawkes, "An overlap invariant entropy measure of 3D medical image alignment," *Pattern Recognition,* vol. 32, pp. 71-86, 1999.

[68] H. Luan, F. Qi, Z. Xue, L. Chen, and D. Shen, "Multimodality image registration by maximization of quantitative–qualitative measure of mutual information," *Pattern Recognition,* vol. 41, pp. 285-298, 2008.

[69] M. Belis and S. Guiasu, "A quantitative-qualitative measure of information in cybernetic systems (Corresp.)," *IEEE Transactions on Information Theory,* , vol. 14, pp. 593-594, 1968.

[70] T. Kadir and M. Brady, "Saliency, scale and image description," *International Journal of Computer Vision,* vol. 45, pp. 83-105, 2001.

[71] J. P. W. Pluim, J. B. A. Maintz, and M. A. Viergever, "Image registration by maximization of combined mutual information and gradient information," *IEEE Transactions on Medical Imaging, ,* vol. 19, pp. 809-814, 2000.

[72] J. B. A. Maintz, P. A. van den Elsen, and M. A. Viergever, "Comparison of edge-based and ridge-based registration of CT and MR brain images," *Medical Image Analysis,* vol. 1, pp. 151-161, 1996.

[73] D. Rueckert, L. I. Sonoda, C. Hayes, D. L. Hill, M. O. Leach, and D. J. Hawkes, "Nonrigid registration using free-form deformations: application to breast MR images," *IEEE Transactions on Medical Imaging,,* vol. 18, pp. 712-721, 1999.

[74] X. Zhuang, D. J. Hawkes, and S. Ourselin, "Unifying Encoding of Spatial Information in Mutual Information for Nonrigid Registration," presented at the Proceedings of the 21st International Conference on Information Processing in Medical Imaging, Williamsburg, Virginia, 2009.

[75] C. M. Rueckert. Daniel, Hill. DLG, Hawkes. David J, "Non-rigid registration using higher-order mutual information," in *Medical Imaging 2000,* 2000, pp. 438-447.

[76] Q. Li and H. Ji, "Multimodality image registration using local linear embedding and hybrid entropy," *Neurocomputing,* vol. 111, pp. 34-42, 2013.

[77] J. Sadr, S. Mukherjee, K. Thoresz, and P. Sinha, "The fidelity of local ordinal encoding," *Advances in Neural Information Processing Systems,* vol. 2, pp. 1279-1286, 2002.

[78] Y. Han, T. Tan, Z. Sun, and Y. Hao, "Embedded palmprint recognition system on mobile devices," in *Advances in Biometrics,* ed: Springer, 2007, pp. 1184-1193.

[79] S. T. Roweis and L. K. Saul, "Nonlinear dimensionality reduction by locally linear embedding," *Science,* vol. 290, pp. 2323-2326, 2000.

[80] C. Zhang, J. Wang, N. Zhao, and D. Zhang, "Reconstruction and analysis of multi-pose face images based on nonlinear dimensionality reduction," *Pattern Recognition,* vol. 37, pp. 325-336, 2004.

[81] K. Miller, "Constitutive model of brain tissue suitable for finite element analysis of surgical procedures," *Journal of Biomechanics,* vol. 32, pp. 531-537, 1999.

[82] K. Miller, A. Wittek, G. Joldes, A. Horton, T. Dutta-Roy, J. Berger, *et al.*, "Modelling brain deformations for computer-integrated neurosurgery," *International Journal for Numerical Methods in Biomedical Engineering,* vol. 26, pp. 117-138, 2010.

[83] A. Wittek, K. Miller, R. Kikinis, and S. K. Warfield, "Patient-specific model of brain deformation: Application to medical image registration," *Journal of Biomechanics,* vol. 40, pp. 919-929, 2007.

[84] A. Wittek, G. Joldes, M. Couton, S. K. Warfield, and K. Miller, "Patient-specific non-linear finite element modelling for predicting soft organ deformation in real-time; Application to non-rigid neuroimage registration," *Progress in Biophysics and Molecular Biology,* vol. 103, pp. 292-303, 2010.

[85] A. Horton, A. Wittek, and K. Miller, "Subject-specific biomechanical simulation of brain indentation using a meshless method," *Medical Image Computing and Computer-Assisted Intervention–MICCAI 2007,* pp. 541-548, 2007.

[86] G. R. Joldes, A. Wittek, and K. Miller, "Suite of finite element algorithms for accurate computation of soft tissue deformation for surgical simulation," *Medical Image Analysis,* vol. 13, pp. 912-919, 2009.

[87] H. Delingette and N. Ayache, "Soft tissue modeling for surgery simulation, in," *N. Ayache (Ed.), Computational Models for the Human Body, Handbook of Numerical Analysis (Ed: P. Ciarlet), Elsevier,* pp. 453--550, 2004.

[88] D. Hawkes, P. Edwards, D. Barratt, J. Blackall, G. Penney, and C. Tanner, "Measuring and Modeling Soft Tissue Deformation for Image Guided Interventions." vol. 2673, N. Ayache and H. Delingette, Eds., ed: Springer Berlin / Heidelberg, 2003, pp. 1004-1004.

[89] T. J. Carter, M. Sermesant, D. M. Cash, D. C. Barratt, C. Tanner, and D. J. Hawkes, "Application of soft tissue modelling to image-guided surgery," *Medical Engineering & Physics,* vol. 27, pp. 893-909, 2005.

[90] G. E. Farin, *Curves and Surfaces for Computer-Aided Geometric Design: A Practical Code*: Academic Press, Inc., 1996.

[91] O. Ecabert, T. Butz, A. Nabavi, and J.-P. Thiran, "Brain shift correction based on a boundary element biomechanical model with different material properties," in *Medical Image Computing and Computer-Assisted Intervention-MICCAI 2003,* ed: Springer, 2003, pp. 41-49.

[92] A. Goshtasby, "Registration of images with geometric distortions," *IEEE Transactions on Geoscience and Remote Sensing, ,* vol. 26, pp. 60-64, 1988.

[93] K. Montgomery, C. Bruyns, J. Brown, S. Sorkin, F. Mazzella, G. Thonier, *et al.*, "Spring: A general framework for collaborative, real-time surgical simulation," *Medicine meets virtual reality 02/10: digital upgrades, applying Moore's law to health,* vol. 85, p. 296, 2002.

[94] R. D. Bucholz, D. D. Yeh, J. Trobaugh, L. L. McDurmont, C. D. Sturm, C. Baumann, *et al.*, "The correction of stereotactic inaccuracy caused by brain shift

using an intraoperative ultrasound device," in *CVRMed-MRCAS'97*, 1997, pp. 459-466.

[95] O. Škrinjar, C. Studholme, A. Nabavi, and J. Duncan, "Steps toward a stereo-camera-guided biomechanical model for brain shift compensation," in *Information Processing in Medical Imaging*, 2001, pp. 183-189.

[96] S. F. Frisken-Gibson, "Using linked volumes to model object collisions, deformation, cutting, carving, and joining," *IEEE Transactions on Visualization and Computer Graphics, ,* vol. 5, pp. 333-348, 1999.

[97] M. Ferrant, A. Nabavi, B. Macq, F. A. Jolesz, R. Kikinis, and S. K. Warfield, "Registration of 3-D intraoperative MR images of the brain using a finite-element biomechanical model," *IEEE Transactions on Medical Imaging, ,* vol. 20, pp. 1384-1397, 2001.

[98] O. Clatz, H. Delingette, E. Bardinet, D. Dormont, and N. Ayache, "Patient-specific biomechanical model of the brain: application to Parkinson's disease procedure," *Surgery Simulation and Soft Tissue Modeling,* pp. 1004-1004, 2003.

[99] I. Garg, S. Ding, A. M. Coffey, P. Dumpuri, R. C. Thompson, B. M. Dawant, *et al., Enhancement of subsurface brain shift model accuracy: a preliminary study* vol. 7625: SPIE, 2010.

[100] M. I. Miga, T. K. Sinha, D. M. Cash, R. L. Galloway, and R. J. Weil, "Cortical surface registration for image-guided neurosurgery using laser-range scanning," *IEEE Transactions on Medical Imaging, ,* vol. 22, pp. 973-985, 2003.

[101] D. Siyi, M. I. Miga, J. H. Noble, A. Cao, P. Dumpuri, R. C. Thompson, *et al.*, "Semiautomatic Registration of Pre- and Postbrain Tumor Resection Laser Range Data: Method and Validation," *IEEE Transactions on Biomedical Engineering, ,* vol. 56, pp. 770-780, 2009.

[102] O. Ecabert, T. Butz, A. Nabavi, and J. P. Thiran, "Brain shift correction based on a boundary element biomechanical model with different material properties," *Medical Image Computing and Computer-Assisted Intervention-MICCAI 2003,* pp. 41-49, 2003.

[103] O. Monga, N. Ayache, and P. T. Sander, "From voxel to intrinsic surface features," *Image and Vision Computing,* vol. 10, pp. 403-415, 1992.

[104] C. Davatzikos, J. L. Prince, and R. N. Bryan, "Image registration based on boundary mapping," *IEEE Transactions on Medical Imaging, ,* vol. 15, pp. 112-115, 1996.

[105] J. B. A. Maintz, P. A. van den Elsen, and M. A. Viergever, "Evaluation of ridge seeking operators for multimodality medical image matching," *IEEE Transactions on Pattern Analysis and Machine Intelligence, ,* vol. 18, pp. 353-365, 1996.

[106] T. C. Cheah., S. A. Shanmugam., and K. A. L. Mann., "Medical image registration: Comparison and evaluation of nonlinear transformation algorithms," presented at the Biomedical Engineering and Sciences (IECBES), 2010 IEEE EMBS Conference on, Kuala Lumpur, 2010.

[107] F. L. Bookstein, "Principal warps: thin-plate splines and the decomposition of deformations," *IEEE Transactions on Pattern Analysis and Machine Intelligence,* , vol. 11, pp. 567-585, 1989.

[108] MATLAB, "version 7.11.0.584 (R2010b)," *The MathWorks Inc.*, vol. Natick, Massachusetts, 2010.

[109] S. Periaswamy and H. Farid, "Medical image registration with partial data," *Medical image analysis,* vol. 10, pp. 452-464, 2006.

[110] P. Risholm, E. Samset, and W. Wells III, "Validation of a nonrigid registration framework that accommodates tissue resection," in *SPIE Medical Imaging*, 2010, pp. 762319-762319-11.

[111] J. M. F. Jay B. West, Matthew Y. Wang, Benoit M. Dawant, Calvin R. Maurer, Jr., Robert M. Kessler, Robert J. Maciunas, Christian Barillot, Didier Lemoine, Andre M. F. Collignon, Frederik Maes, Paul Suetens, Dirk Vandermeulen, Petra A. van , den Elsen, Paul F. Hemler, Sandy Napel, Thilaka S. Sumanaweera, Beth A. Harkness, Derek L. Hill, Colin Studholme, Gregoire Malandain, Xavier Pennec, Marilyn E. Noz, Gerald Q. Maguire, Jr., Michael Pollack, Charles A. Pelizzari, Richard A. Robb, Dennis P. Hanson, Roger P. Woods, "Comparison and evaluation of retrospective intermodality image registration techniques," 1996, pp. 332-347.

[112] I. Vajda, *Theory of statistical inference and information*. The University of California: Kluwer Academic Publishers Dordrecht, 1989.

[113] J. Maintz, E. Meijering, and M. Viergever, "General multimodal elastic registration based on mutual information," presented at the In: Proceedings of the SPIE Image Processing, 1998.

[114] A. Kuba, M. Šáamal, A. Todd-Pokropek, M. Holden, D. Hill, E. Denton, *et al.*, "Voxel Similarity Measures for 3D Serial MR Brain Image Registration," in *Information Processing in Medical Imaging*. vol. 1613, ed: Springer Berlin / Heidelberg, 1999, pp. 472-477.

[115] L. Freire, A. Roche, and J.-F. Mangin, "What is the best similarity measure for motion correction in fMRI time series?," *IEEE Transactions on Medical Imaging,* , vol. 21, pp. 470-484, 2002.

[116] M. A. Wirth, J. Narhan, and D. W. Gray, "Nonrigid mammogram registration using mutual information," in *Medical Imaging 2002*, 2002, pp. 562-573.

[117] K. A. Johnson. and J. A. Becker. (7/1/2011). *Whole Brain Atlas*. Available: http://www.med.harvard.edu/AANLIB/home.html

[118] W. Grimson, R. Kikinis, F. Jolesz, and P. Black, "Image-guided surgery," *Scientific American,* vol. 280, pp. 54-61, 1999.

[119] E. Watanabe, T. Watanabe, S. Manaka, Y. Mayanagi, and K. Takakura, "Three-dimensional digitizer (neuronavigator): new equipment for computed tomography-guided stereotaxic surgery," *Surgical neurology,* vol. 27, pp. 543-547, 1987.

[120] Y. Kosugi, E. Watanabe, J. Goto, T. Watanabe, S. Yoshimoto, K. Takakura, *et al.*, "An articulated neurosurgical navigation system using MRI and CT images," *IEEE Transactions on Biomedical Engineering, ,* vol. 35, pp. 147-152, 1988.

[121] R. L. Galloway Jr, R. J. Maciunas, and C. Edwards, "Interactive image-guided neurosurgery," *IEEE Transactions on Biomedical Engineering, ,* vol. 39, pp. 1226-1231, 1992.

[122] T. Peters, B. Davey, P. Munger, R. Comeau, A. Evans, and A. Olivier, "Three-dimensional multimodal image-guidance for neurosurgery," *Medical Imaging, IEEE Transactions on,* vol. 15, pp. 121-128, 1996.

[123] P. Merloz, J. Tonetti, L. Pittet, M. Coulomb, S. Lavallee, and P. Sautot, "Pedicle screw placement using image guided techniques," *Clinical Orthopaedics And Related Research,* vol. 354, pp. 39-48, 1998.

[124] A. M. DiGioia III, B. Jaramaz, and B. D. Colgan, "Computer assisted orthopaedic surgery: image guided and robotic assistive technologies," *Clinical Orthopaedics And Related Research,* vol. 354, pp. 8-16, 1998.

[125] L. Joskowicz, C. Milgrom, A. Simkin, L. Tockus, and Z. Yaniv, "FRACAS: a system for computer-aided image-guided long bone fracture surgery," *Computer Aided Surgery,* vol. 3, pp. 271-288, 1998.

[126] Y. R. Rampersaud, D. A. Simon, and K. T. Foley, "Accuracy requirements for image-guided spinal pedicle screw placement," *Spine,* vol. 26, pp. 352-359, 2001.

[127] L. Ibanez, W. Schroeder, L. Ng, and J. Cates, "The ITK Software Guide, 2nd edition," *Kitware Inc,* 2005.

[128] ITK. (9/7/2012). *The Insight Segmentation and Registration Toolkit*. Available: http://www.itk.org

[129] W. J. Schroeder, K. M. Martin, and W. E. Lorensen, "The design and implementation of an object-oriented toolkit for 3D graphics and visualization," 1996, pp. 93-ff.

[130] W. Schroeder, K. Martin, and B. Lorensen, *The Visualization Toolkit, Third Edition*: Kitware Inc., 2003.

[131] VTK. (9/7/2012). *The Visualization Toolkit*. Available: http://www.vtk.org/

[132] I. Wolf, M. Vetter, I. Wegner, M. Nolden, T. Bottger, M. Hastenteufel, *et al.*, "The medical imaging interaction toolkit (MITK): a toolkit facilitating the creation of interactive software by extending VTK and ITK," 2004, pp. 16-27.

[133] R. Shams, P. Sadeghi, R. Kennedy, and R. Hartley, "A Survey of Medical Image Registration on Multicore and the GPU," *Signal Processing Magazine, IEEE,* vol. 27, pp. 50-60, 2010.

[134] W. Plishker, O. Dandekar, S. Bhattacharyya, and R. Shekhar, "Utilizing Hierarchical Multiprocessing for Medical Image Registration," *Signal Processing Magazine, IEEE,* vol. 27, pp. 61-68, 2010.

[135] Y. Chen, C. Chakrabarti, S. Bhattacharyya, and B. Bougard, "Signal Processing on Platforms with Multiple Cores: Part 2-Applications and Design [From the Guest Editors]," *Signal Processing Magazine, IEEE,* vol. 27, pp. 20-21, 2010.

[136] I. Bitter, R. Van Uitert, I. Wolf, L. Ibáñez, and J. M. Kuhnigk, "Comparison of four freely available frameworks for image processing and visualization that use ITK," *IEEE Transactions on Visualization and Computer Graphics*, , vol. 13, pp. 483-493, 2007.

[137] U. Meier, O. López, C. Monserrat, M. C. Juan, and M. Alcaniz, "Real-time deformable models for surgery simulation: a survey," *Computer methods and programs in biomedicine,* vol. 77, pp. 183-197, 2005.

[138] CMake. (22/8/2014). *CMake 2.8.11*. Available: http://www.cmake.org/

[139] Microsoft.Visual.Studio. (9/7/2012). *Microsoft Visual Studio*. Available: http://www.microsoft.com/visualstudio/en-my

[140] M. J. Ackerman, "The visible human project," *Proceedings of the IEEE,* vol. 86, pp. 504-511, 1998.

[141] C. Multiphysics, "Comsol Inc," *Burlington, MA*, 2005.

[142] M. I. Miga, "Development and quantification of a 3D brain deformation model for model-updated image-guided stereotactic neurosurgery," 1998.